UNIVERSITÀ DELLA CALABRIA

Department DIATIC

Philosophical Doctorate in

Scienze ed Ingegneria dell'Ambiente delle Costruzioni e dell'Energia

CYCLE

XXIX

GEO-REFERENCING DEVICES BASED ON RETROREFLECTORS FOR GALILEO AND EARTH OBSERVATION

Settore Scientifico Disciplinare FIS/01

Coordinator: Ch.mo Prof. Pietro Pantano

Sign:

Supervisor/Tutor: Dr. Simone Dell'Agnello

Sign:

PhD Candidate: Dr. Stefania Contessa

Sign:

A Daniele

Contents

List of Acronym **v**

Why this work and what my contribution was **1**

1 Geodetic Positioning Techniques and Applications **5**

1.1 Satellite Laser Ranging 5

1.1.1 Corner Cube Reflectors 10

1.1.2 Velocity Aberration 13

1.2 GNSS: Global Navigation Satellite System 13

1.3 Synthetic Aperture Radar Technology 18

1.4 SLR Application on GNSS and Earth Observation 27

2 G-CALIMES Project **31**

2.1 Galileo constellation 32

2.2 Earth Observation Satellites 36

2.2.1 Cosmo-SkyMed Constellation 36

2.2.2 Sentinel constellation 38

3 Instrumentation design and goals **43**

3.1 CORA design 44

3.1.1 Optical simulations 44

3.1.2 Mechanical design 50

3.2 INCA design 56

3.2.1 Radar Cross Section simulations 62

3.3 CORA and INCA design conclusions 65

4 SCF-Lab and Testing **67**

4.1 SCF_Lab facility and subsystems 68

4.2 SCF-Test 79

4.3 Orbit-Test 83

4.3.1 EO Orbit simulations 84

5 CORA Characterization and Results **91**

5.1 CORA SCF-Test characterization 91

5.1.1 CORA SCF-Test Results 95

5.2 CORA Orbit-Test Characterization 106

5.2.1 CORA Orbit-Test Results 108

5.3 Correlation with Galileo and GNSS 113

5.3.1 Results of SCF-Test of Galileo IOV 114

5.3.2 Selected results of IRNSS test 118

5.3.3 Comparison with testing results of INFN-ASI LRA 121

5.4 Conclusions about CORA test results 125

6 INCA Characterization and Results **127**

6.1 Radar Reflector Detection 128

6.2 INCA deployment and first measurement 136

6.3 Conclusions and future activity for INCA entire characterization . . . 140

Conclusions and Future work **141**

List of Acronyms and Definitions

AM0 Air Mass 0

ASI Agenzia Spaziale Italiana

CCD Charged Coupled Device

CCR Corner Cube Reflector

CORA COsmo Retroreflector Array

DAO Dihedral Angle Offset

EM Engineering Model

EO Earth Observation

ESA European Space Agency

ETRUSCO Extra Terrestrial Ranging to Unified Satellite COnstellations

FFDP Far Field Diffraction Pattern

G-CALIMES Galileo-Cosmo-Skymed Absolute Laser Intercalibration with Measurements on Earth and in Space

GCO Galileo Critical Orbit

GIOVE Galileo In Orbit Validation Element

GLONASS GLObal'naya Navigationnay Sputnikovaya Sistema

GNSS Global Navigation Satellite System

GPS Global Positioning System

GRA GNSS Retroreflector Array

ILRS International Laser Ranging Service

INCA INter CAlibration

INFN Istituto Nazionale di Fisica Nucleare

IOV In Orbit Validation

IR InfraRed

IRNSS Indian Regional Navigation Satellite System

ITRF International Terrestrial Reference Frame

IW Interferometric Wide

ISCE InSAR Scientific Computing Environment

JPL Jet Propulsion Laboratory

KPI Key Performance Indicator

LAGEOS LAser GEOdynamics Satellite

LEO Low Earth Orbit

LN2 Liquid Nitrogen

LNF Laboratori Nazionali di Frascati

LRA Laser Retroreflector Array

LTAN Longitude Time of the Ascending Node

MEO Medium Earth Orbit

MLI Multi-Layer Insulation

OCS Optical Cross Section

RCS Radar Cross Section

SAR Synthetic Aperture Radar

SCF Satellite/lunar/GNSS laser ranging/altimetry and Cube/microsat Characterization Facility

SCF_Lab Satellite/lunar/GNSS laser ranging/altimetry and Cube/microsat Characterization Facilities Laboratory

SLC Single Look Complex

SLR Satellite Laser Ranging

SS Solar Simulator

SSO Sun-synchronous Orbit

VA Velocity Aberration

Why this work and what my contribution was

This work is the result of a collaboration between University of Calabria, Istituto Nazionale di Fisica Nucleare (INFN) and Italian Ministry of Defense, in the framework of Galileo-Cosmo-Skymed Absolute Laser Intercalibration with Measurements on Earth and in Space (G-CALIMES), a research and technological development project. The aim of G-CALIMES is the absolute inter-calibration of three different positioning techniques: Satellite Laser Ranging (SLR), Global Navigation Satellite System (GNSS) and Synthetic Aperture Radar (SAR), for the benefit of European Galileo and Italian COSMO-SkyMed programs.
SLR provides centimeter accuracy orbits and long term time-series but it is strongly sensitive to clouds and rains; GNSS has an accuracy at decimeter level and SAR has meter accuracy, but it is available in every atmospheric conditions during day and night time. Therefore a measurement combining these techniques can improve the absolute positioning of Earth Observation (EO) satellites and their terrestrial maps, can realize co-location between EO and GNSS constellations, all respect to the International Terrestrial Reference Frame (ITRF), defined by SLR technique.

To reach this goal my research activity regarded the development and perfor-

mance testing of space and terrestrial instrumentation based on retroreflectors. The space instrument designed and characterized is named COsmo Retroreflector Array (CORA) and consists of four optical Corner Cube Reflector (CCR)s made of fused silica, optimized for COSMO Second Generation satellites to improve their orbit positioning; the ground based instrument is named INter CAlibration (INCA) and consists of a radar reflector equipped with a GPS/Galileo receiver and an optical CCR. It can be detected by the three positioning techniques: SLR (using optical CCR), GNSS (using the receiver) and SAR (using radar reflector). These devices were designed and tested at the Satellite/lunar/GNSS laser ranging/altimetry and Cube/microsat Characterization Facilities Laboratory (SCF_Lab) of Laboratori Nazionali di Frascati (LNF), with the collaboration of NASA-Jet Propulsion Laboratory (JPL).

My research activity was focused on:

1. Thermo/optical characterization of laser retroreflector arrays for GNSS, in order to investigate the correlation between structural design and optical performances

2. CORA design and qualification

3. INCA preliminary and first-phase in-field characterization carried out at JPL and LNF respectively.

CORA experimental activity consisted of two tests: the standard SCF-Test and the Orbit-Test, conducted in a space-simulated environment, evaluating device's thermal and optical performances. In particular key parameters I evaluated are CCR thermal relaxation time and Far Field Diffraction Pattern of the laser return at ground. This analysis is important to deeply understand instrument's engineering

properties and its real behavior during operational life.

INCA characterization consisted of two phases: the first was carried out at JPL during my summer internship, where I performed radar reflector detection and geometric calibration of Sentinel-1A images, comparing radar measurements with GPS coordinates; second part was performed at LNF, where I processed Sentinel-1A images to evaluate the pointing system and the best background for INCA deployment.

In Chapter 1 I describe the three positioning techniques used in this work and in Chapter 2 I present G-CALIMES project, with a detail description of GNSS and EO constellations to which the project is applicable: Galileo, COSMO-SkyMed and Sentinel. Chapter 3 describes CORA and INCA devices, while the SCF_Lab is presented in detail in Chapter 4, with a description of test procedures used for characterization. Finally Chapter 5 and Chapter 6 concern on CORA and INCA test results respectively.

Chapter 1

Geodetic Positioning Techniques and Applications

In this Chapter I present three different positioning techniques used in space environment: Satellite Laser Ranging, Radionavigation and Synthetic Aperture Radar technology. All of them are based on satellites equipped with dedicated instrumentation but have different availabilities and accuracies. The aim of this work is a deep knowledge of these techniques and their inter-calibration in order to perform geo-referencing measurements.

1.1 Satellite Laser Ranging

SLR is one of the most accurate positioning techniques currently available to determine the geocentric position of Earth orbiting satellites (the only space geodesy technique that measures directly a range), providing unambiguous centimeter accuracy orbits and long term stable time-series. It is based on a global network of

ground stations that measure the round trip time of flight of ultrashort laser pulses transmitted to satellites equipped with special retroreflectors. These retroreflectors called CCR are quartz prisms made of a radiation resistant grade Fused Silica with a particular geometry that allows a laser beam to come back along the same direction from which it came.

SLR gives the most precise positioning in space, as well as a metrologically 'absolute' positioning with respect to the ITRF [1], a Cartesian coordinate system co-rotating in space with the Earth and with origin on its center-of-mass (geocenter). SLR technique provides also important contributions to fundamental physics studies: for example measurement of temporal variation in the Earth's gravity field, mapping volumetric changes in continental ice masses, evaluation of long-term climate changes and validation of General Relativity Theory [2]. Given its accuracy it is also used to determine accurate distance measurements to retroreflector arrays deployed by Apollo and Russian Luna missions on the Moon ([3] and [4]).

Laser ranging data are collected, analysed and distributed by a network of laser stations that together form the International Laser Ranging Service (ILRS) [5], instituted in 1998 by the Global SLR community. The data sets are used by the ILRS to calculate fundamental parameters such us:

- satellite ephemerides
- Earth orientation parameters (polar motion and length of day)
- coordinates and velocity of tracking stations
- time varying geocenter coordinates
- coefficients of Earth's gravity field, variable and constant
- fundamental physical constants

- lunar ephemerides and librations
- lunar orientation parameters

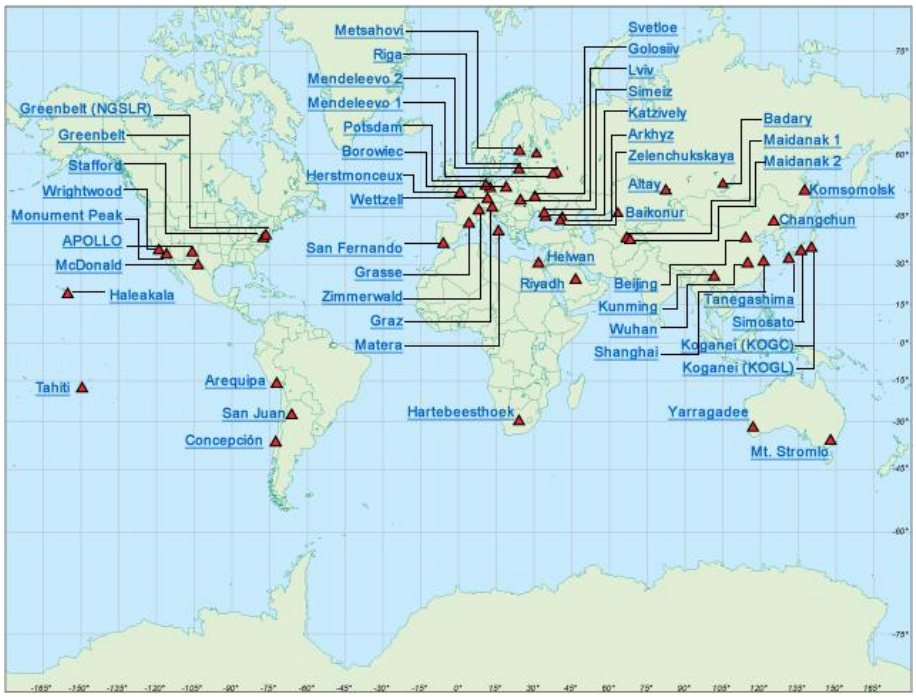

Figure 1.1: ILRS network stations

Nowadays ILRS is composted by more than 40 ground stations (see picture in Fig.1.1) which routinely track about 30 retroreflector equipped satellites, including geodynamic, radio-altimetry, Earth sensing, general relativity and radio-navigation satellites. Four stations (Matera in Italy, Grasse in France, and McDonald and APOLLO in USA) regularly track the arrays deployed on the Moon surface and the number of stations with this capability is growing, including German station of Wetzell.

Laser ranging stations use $\sim$ 100 ps laser pulses and fast timing electronics for taking measurements. Primary products from the stations are normal points, temporal

averages of single range measurements (few seconds depending on the altitude of the satellite) transmitted rapidly (within few hours) to Data Analysis Centres. The precision is typically of few tens of picoseconds ($\sim$ 1 - 10 mm) but the accuracy is affected by two main error sources: atmospheric attenuation/refraction and reference of measurement to the satellite center of mass (range correction). Atmospheric refraction can cause significant errors in SLR measurements. In order to correct these errors, two techniques have been developed: atmospheric models and pulse two-color ranging systems [32]. Atmospheric models are based upon surface measurements of pressure, temperature and relative humidity. The residual errors are probably due to horizontal gradients in the refractivity, which are sensitive to local topographic effects. Moreover atmospheric turbulence can add random fluctuations in the refractivity, but this phenomenon only introduces small errors for low elevation. Since the launch of LAser GEOdynamics Satellite (LAGEOS) satellites is possible to better estimate the Earth center of mass and consequently to improve the atmospheric models, especially for low elevation propagation. With the upgrade of laser ranging stations, pulsed two-color ranging systems are used. They can directly estimate the atmospheric delay in satellite ranging, by measuring the difference in propagation times between two optical pluses transmitted at different wavelengths. Laboratory measurement are important instead for the second error source in the SLR accuracy, in order to refer the range measurement to a reference point on the satellite.

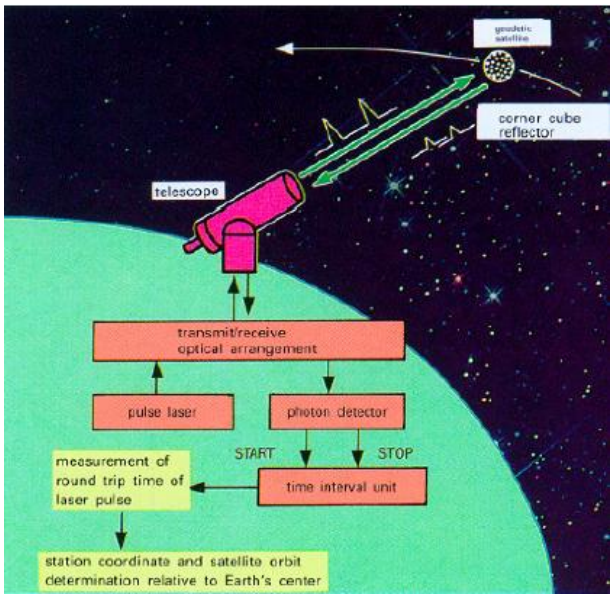

Figure 1.2: SLR time of flight measurement

1.1.1 Corner Cube Reflectors

Before proceeding it is necessary to describe the characteristics of CCRs and the different types used for SLR. CCRs are retroreflector prisms, made out of a corner of a cube (see Fig.1.3[1]), whose main feature is to reflect the light back to the same incident direction. This is achieved by means of a triple reflection of a ray on the three reflecting faces. Fig.1.4 shows this triple reflection in a simulated CCR and the concept of retroreflection in a 2D sketch.

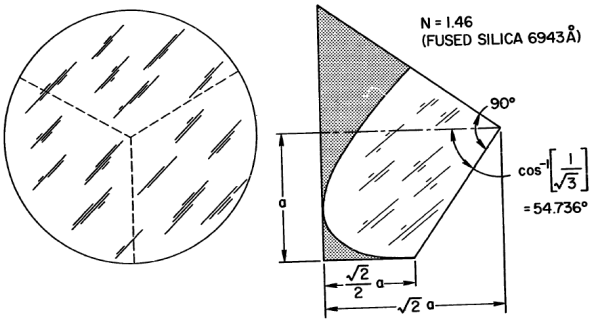

Figure 1.3: Corner Cube prism geometry

CCRs can be divided into two main classes: solid and hollow. Solid cubes are quartz prisms made of a radiation-resistant grade of Fused Silica, with very low thermal expansion, while hollow cubes have only the reflecting faces, made of glass, covered with a high reflectivity metal layer. Solid cubes can further be divided into uncoated and coated categories. Uncoated CCRs are just the solid prism of fused silica, while coated ones are prisms whose reflective faces have a high reflective coating (usually Aluminum or Silver). Retro-reflection for uncoated CCRs works with total internal reflection. Total internal reflection is the effect of Snell's law of

[1]from:*Designed of Retrodirector Arrays for Laser Ranging of satellites*, Peter O. Minott, Gooard Space Flight Center

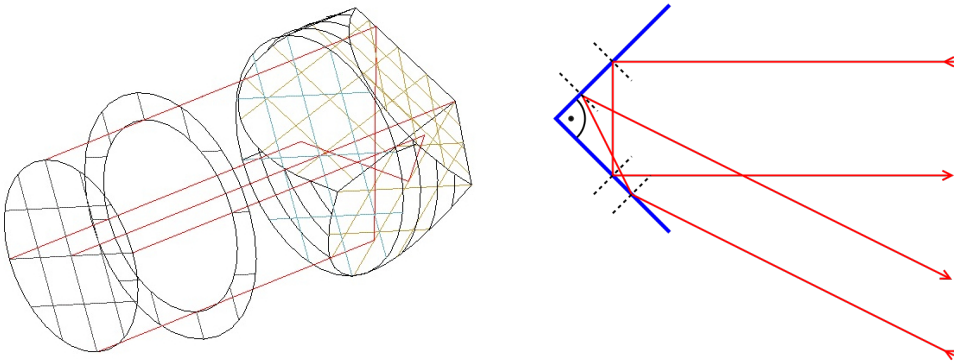

Figure 1.4: Concept of retroreflection of a CCR

refraction when a ray travels across a medium with high density (fused silica) to one with lower density (vacuum). As the angle between the incident ray and the interface between the two media becomes bigger, the intensity of the refracted ray decreases, until the angle reaches a critical value (θc in Fig.1.5); increasing further on the angle, the ray is totally reflected at the interface. In this particular case the interface between the two media will act as a *perfect reflector* (see Fig.1.5) The particular geometry of the CCR makes the ray hits three times the cube an then coming back.

Coated cubes on the other hand act as normal reflectors; the reflection of a ray on their reflecting faces works with classic reflection. Hollow CCRs belong to the coated class. The critical value of the angle allowing reflection, is different between coated and uncoated CCRs: for coated is 54° and for uncoated is 17°. This difference between CCRs comes up in the qualitative, but also quantitative, characteristics of their Far Field Diffraction Pattern (FFDP),the diffraction waveform of the laser return. Coated and hollow reflectors act as mirrors (almost perfect) and as so, the polarization of the laser beam hitting them remains unchanged after the reflections, hence the FFDP shape for perfect CCRs is axial-symmetric. In uncoated CCRs, on

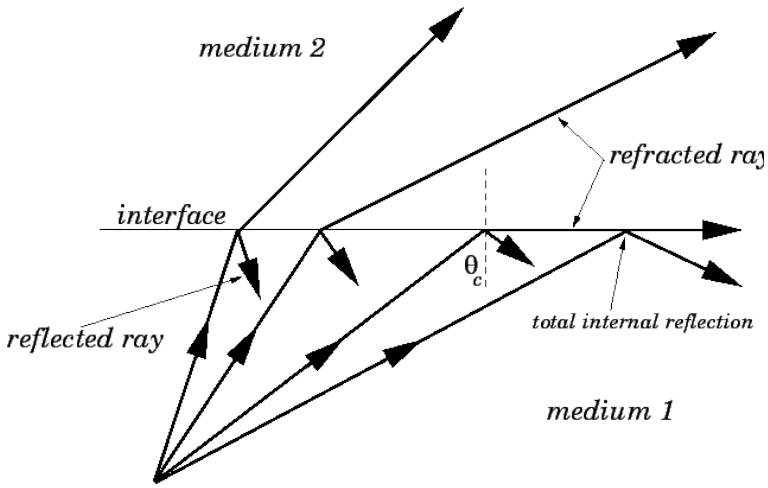

Figure 1.5: Principle of total internal reflection

the other side, the polarization of the hitting beam changes at every reflection and this makes their FFDP of a particular shape. Fig.1.6 shows these different types of retroreflectors.

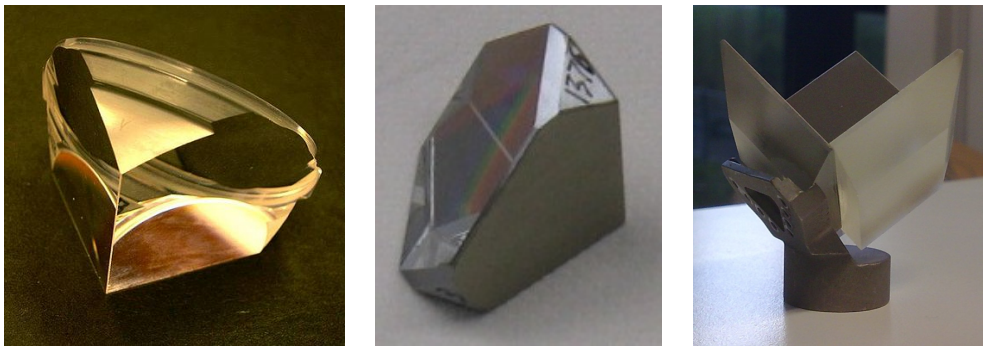

Figure 1.6: Retroreflector types for SLR, from left: solid uncoated, solid coated and hollow

Another important feature of retroreflectors is the artificial increase of the angle between the reflecting faces to compensate the relative motion between satellite and laser ranging station (Velocity Aberration (VA)). It is therefore common to increase

from a fraction of arcsec to few arcsec the angles between the reflecting faces; this can be done on all of the three angles or just one or two and is called Dihedral Angle Offset (DAO). Its effect is to deform the outgoing wavefront of the CCR, moving the intensity away from the center of the FFDP.

1.1.2 Velocity Aberration

The VA is the effect of the relative motion between a satellite in orbit around the Earth and the telescope on the ground; a Laser Retroreflector Array (LRA) retroreflects a laser pulse, coming from a laser ranging station on the ground, back to the same direction, as explained earlier in the section 1.1, so the center of the FFDP would fall in the position occupied by the telescope at the moment the pulse was sent to the satellite. In the FFDP domain this means that the position of the station shifts from the center by a distance dependent from the altitude of the satellite. The angular displacement ϑ from the center of the FFDP, is given by the equation 1.1, as schematized in the Fig.1.7.

$$\vartheta = \frac{2\nu \cos\phi \, \Delta t}{c \, \Delta t} = 2\frac{\nu}{c}\cos\phi \tag{1.1}$$

1.2 GNSS: Global Navigation Satellite System

GNSS is a radio-positioning and transfer timing system from the space, based on signals transmitted by a satellite constellation. It provides position, velocity and time valuations to unlimited users in the space, in sky, on ground and at sea. Measure-

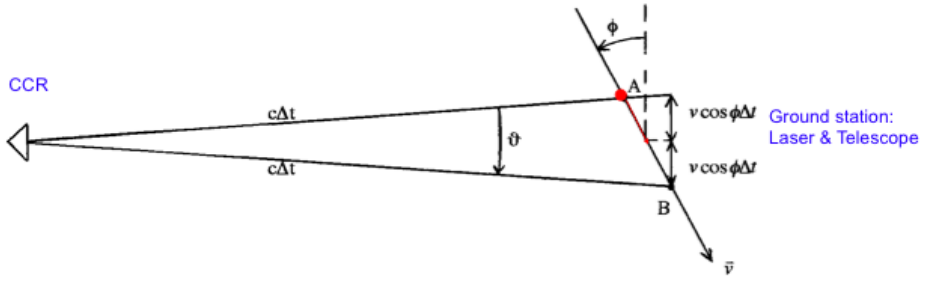

Figure 1.7: Velocity aberration conceptual scheme. ν is the relative velocity satellite-station. A and B are the positions of Laser Ranging station when laser beam is sent to CCR and comes back from it respectively.

ments are available worldwide and all the time in a global frame system, but some systems allow maximum accuracy and noiseless signal only for authorized users. The navigation satellite systems complete and currently operating are:

- Global Positioning System (GPS): 24 global satellites, USA
- GLObal'naya Navigationnay Sputnikovaya Sistema (GLONASS): 24 global satellites, Russia

However in the future this number is expected to increase. China is being equipped whit is own satellite system called COMPASS (30 global and 5 regional satellites), currently active only on the Asian area with 16 satellites; Europe is developing Galileo (30 satellites), currently operating with 18 satellites; India and Japan are implementing their own systems called respectively Indian Regional Navigation Satellite System (IRNSS) (7 regional satellites) and Quasi-Zenith Satellite System (3 regional satellites). To illustrate the diverse use of satellite navigation technology, several examples of application are presented next:

- by land this system is important to request emergency assistance sending his position to an emergency response dispatcher, to survey and map roads and

rail system, to prevent collision and control flow of traffic, to conduct precision farming operations and finally to synchronize clocks and events around the world, defining the Temps Atomique International

- the aviation use satellite navigation to approach better to the various phases of flight, avoiding obstacles and observing the procedures, to transmit aircraft location to the other aircrafts and to Air Traffic Control and to add a margin of safety to operation.

- in space guidance GNSS allows attitude determination (i.e. pitch and roll), time synchronization, orbit determination and absolute and relative position determination. On low orbits GPS measurements are used for atmospheric and ionospheric research and applications in weather prediction and space weather monitoring

- in the maritime field satellite navigation provides unprecedented accuracy and capabilities for mariners and transportation managers and allows underwater surveying, buoy placement and mapping ([6, 7])

The distance between a satellite and a receiver on the Earth is obtained by calculating the time that signal takes to go from the satellite to the receiver. This method is called "one-way" because the microwave signal travels the distance transmitter-receiver once. Navigation satellites are equipped with atomic clocks but receivers have quartz clocks that are less accurate, so there is a problem of synchronization between them. In order to solve this issue each satellite transmits its signal at the beginning of each millisecond, so the receivers know the initial time of transmission and also the final time of reception as it can measure. Unfortunately they do not know the timing error between transmitter and receiver. Moreover the synchronization is not the only cause of delay, but there are other contributions such as receiver

hardware delays, thermal noise, ephemeris errors, ionospheric delay, tropospheric delay and multipath [8], that must be taken into account.
Assuming that satellite clock is perfect, the only clock error is due to the receiver and it is called t_u. This delay is the most important and for a first analysis the other contribution can be ignored [6]. In conclusion the system has four unknowns, three for the user location and one for the synchronization error. Therefore the receiver must identify at least four satellites to estimate a pseudorange ρ between itself and the transmitter, that is:

$$(\rho(t)) = (r(t)) + c \cdot t_u(t_R)$$

where r(t) is the real distance between user and satellite, c is the speed of light and $t_u(t_R)$ is the quartz clock error at time t_R. r(t) is expressed using the following equation:

$$(r(t)) = \sqrt{((x_s - x_u)^2 + (y_s - y_u)^2 + (z_s - z_u)^2)} = \rho(t) - c \cdot t_u(t_R)$$

The subscript u (user) identifies the receiver, while s is the satellite (transmitter). The system is then solved by a linearization around an approximate position of the receiver with a least square method to obtain this following expression:

$$H \cdot \Delta x = \Delta\rho$$

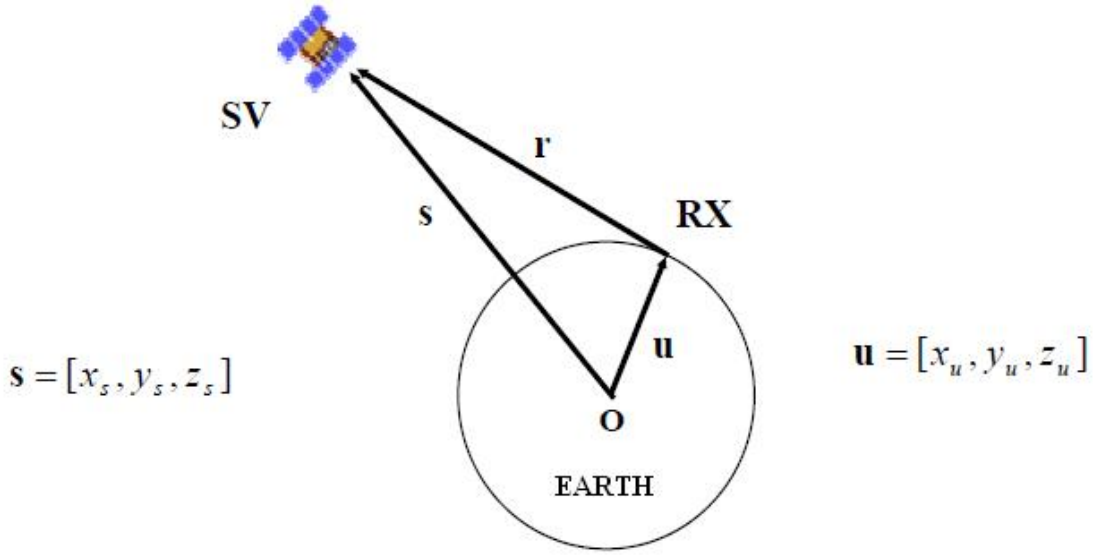

Figure 1.8: Distance between satellite and receiver

where H is the matrix (N×4) of the direction cosines of the satellite-receiver vector, Δx is the position vector but it includes also time variable

$$(\Delta x) = \begin{pmatrix} \Delta x_u \\ \Delta y_u \\ \Delta z_u \\ -c \cdot \Delta t_u \end{pmatrix}$$

and $\Delta\rho$ is the pseudorange vector (N×1). N indicates the number of satellites and it is ≥ 4. If N=4

$$\Delta x = H^{-1} \cdot \Delta\rho$$

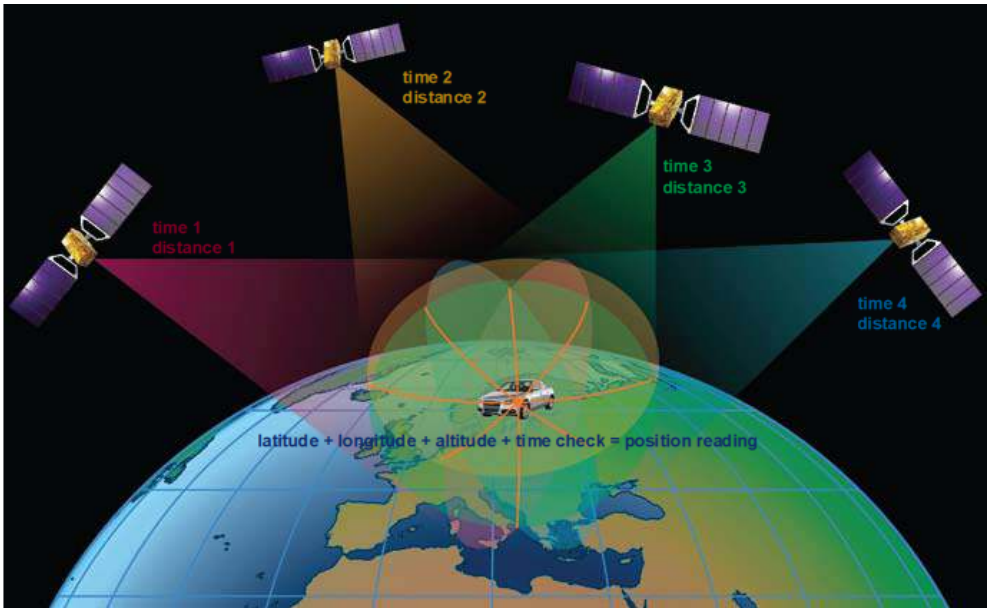

Figure 1.9: How satellite navigation works, from ESA

but, as most of the time the number of equations used is > 4 then it:

$$\Delta x = (H^T H)^{-1} \cdot \Delta\rho$$

1.3 Synthetic Aperture Radar Technology

A SAR is a radar system which utilizes a moving platform to simulate an extremely large antenna and generates high-resolution remote sensing imagery. The idea of a SAR (i.e. an active system) was conceived by Carl Wiley in the USA in the 1950s. He suggested the principle that — because each object in the radar beam has a slightly different speed relative to the antenna — each object will have its own doppler shift; therefore a precise frequency analysis of radar returns will allow the construction

of a detailed image. A SAR image is, for this reason, as a mosaic of small picture elements (pixels), where each one carries amplitude and phase information about the microwave field backscattered by the Earth surface [9].

The core of this system is the antenna: it works like a phase array, but contrary of a large number of parallel elements, SAR uses one antenna in time-multiplex and the different geometric positions of the elements are the result of the moving platform (e.g. airborne or satellite). The antenna transmits a wide bandwidth waveform, so every point of the overflow area is illuminated by a burst of pulses. In the processing analysis, magnitude and phase of the received signals are recombined to create a high resolution image of the area. Transmitted pulses have all defined phase angles to a reference and this makes the system coherent and extremely stable. The main advantages and disadvantages of this system are listed in the Table 1.1: An example

Advantages	All weather capability (low sensitivity to clouds and rain)
	Day and night operation (independence from sun illumination)
	Marginal effects of atmospheric constituents (multi-temporal analysis)
	Sensitivity to dielectric properties (map of water content, ice)
	Sensitivity to surface roughness (measure of ocean wind speed)
	Accurate measurements of distance (interferometry)
	Sensitivity to man made object (reconnaissance, surveillance)
	Foliage and sub-surface penetration
Disadvantages	Complex interaction (hard complex processing)
	Speckle effects (hard in visual interpretation)

Table 1.1: SAR main features

of SAR image is presented in the Fig.1.10 from European Space Agency (ESA) [10]. The antenna, pointing to the Earth surface in a plane perpendicular to the orbit, can not observe at nadir, but its side-looking beam illuminates a swath on the Earth surface with an incidence angle, depending on the off nadir angle (look angle) and on the terrain slope, as shown in the Fig.1.11. The platform direction is called

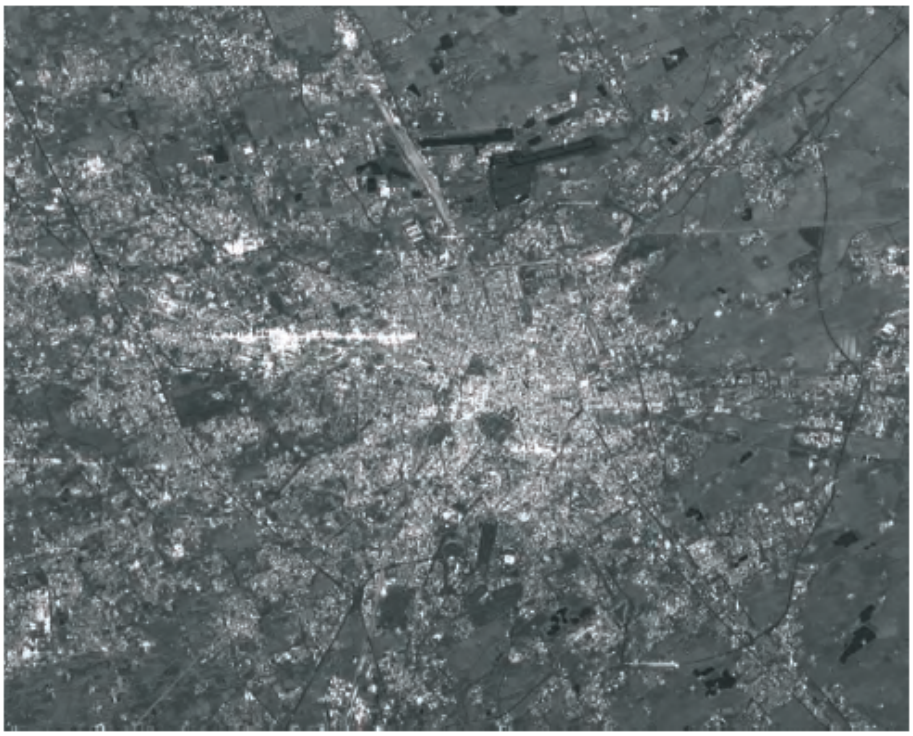

Figure 1.10: SAR image of Milan city from European Remote Sensing satellite (ERS)

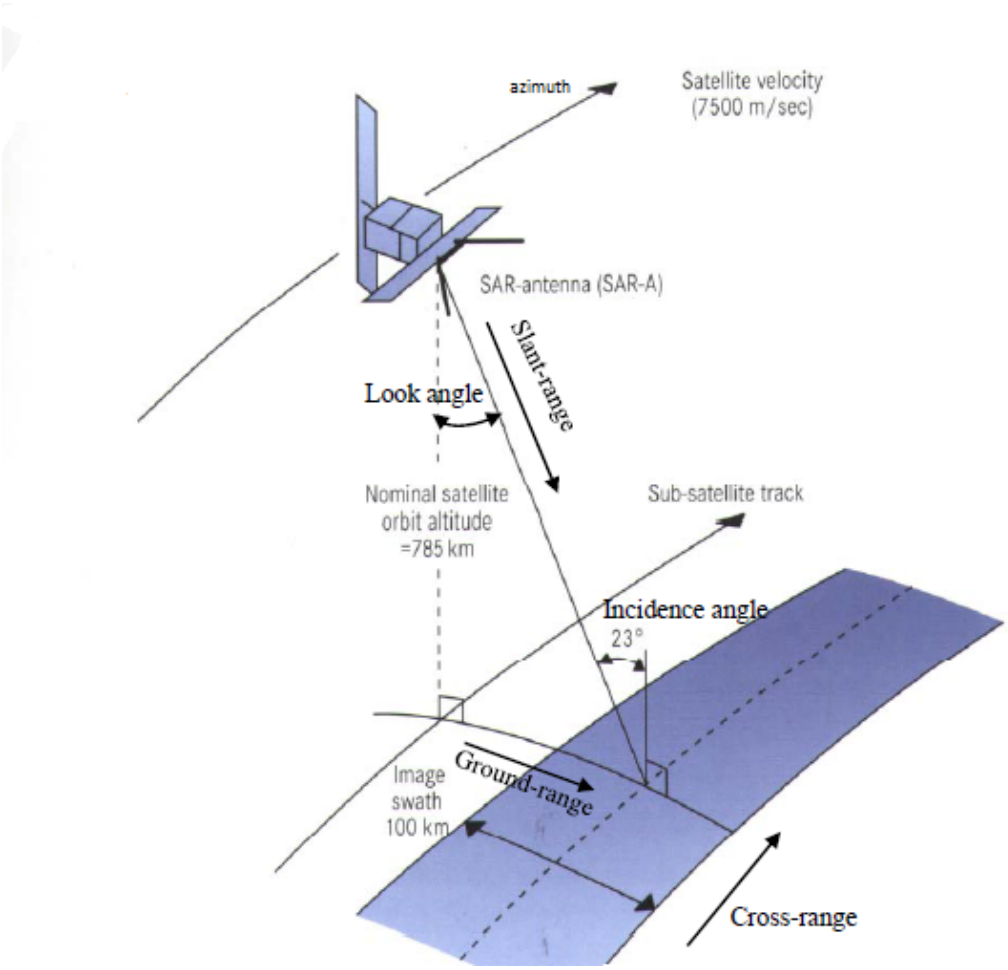

Figure 1.11: SAR system from a satellite

azimuth (or along track), while the cross-track direction is called ground range. The direction along the Line of Sight is usually called slant-range [10]. The geometric resolution, that is the capability to distinguish two objects at a certain distance, in range and azimuth is different: slant range resolution is obtained evaluating the time difference between signals received and it is calculated from the formula 1.2:

$$r_s = \frac{c}{(2B)} \tag{1.2}$$

where c is the speed of light and B is the bandwidth. It is constant and related directly to the transmitted waveform. Its projection in ground range direction is variable and depending on the local incidence angle θ following this expression:

$$r_g = \frac{c}{2B\sin(\theta)} \tag{1.3}$$

Azimuth resolution is proportional to the antenna length D along track direction, as show in the formula 1.4:

$$r_a = \frac{D}{2} \tag{1.4}$$

There are three different SAR operation modes: Stripmap, Spotlight and ScanSAR, with different acquisition configurations and resolutions. In Stripmap Mode the real antenna is directed toward the ground at a fixed angle of elevation, see Fig.1.12. Spotlight Mode steers the real antenna toward the scene center to exceed the limit on the synthetic aperture of the Stripmap Mode, as shown in the Fig.1.13. The main differences between these two modes are that Stripmap images have a very large azimuth swath but limited resolution while Spotlight images have a small azimuth swath with very high resolution. Finally ScanSAR Mode acquisition is performed by using the same azimuth antenna steering of the Stripmap Mode, but switching the

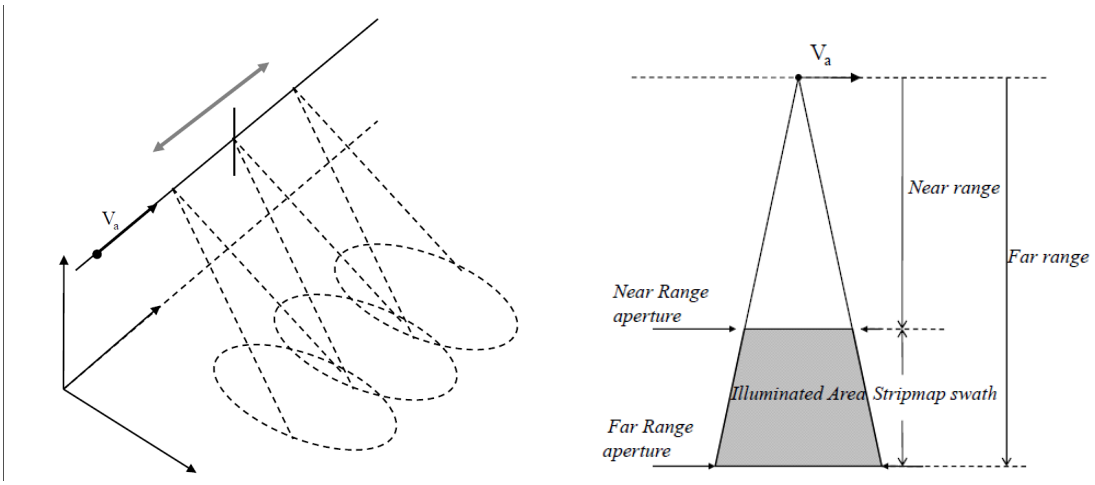

Figure 1.12: Left, Stripmap Mode configuration. Right, Illuminated area of a Stripmap image

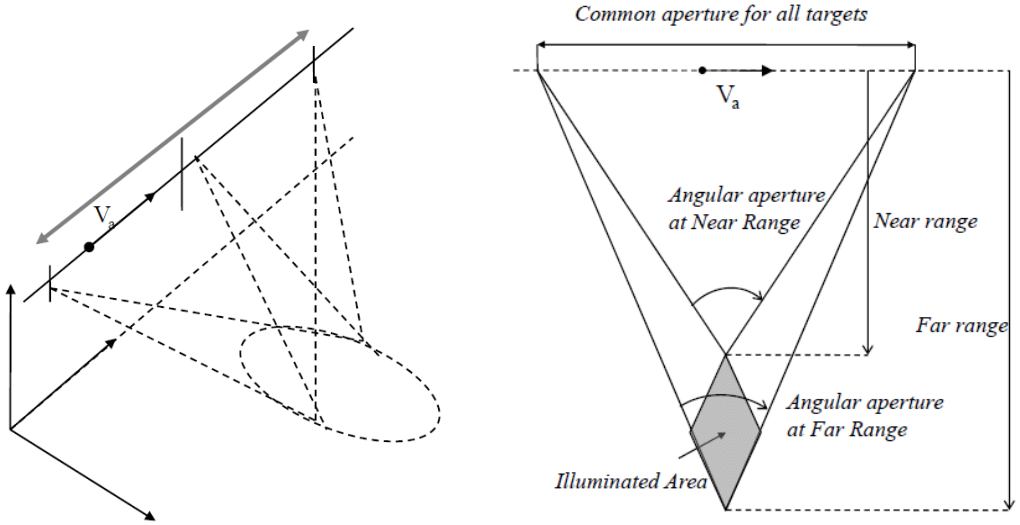

Figure 1.13: Left, Spotlight Mode configuration. Right, Illuminated area of a Spotlight image

beam in elevation after each burst to cover a wider swath, Fig.1.14. This last mode is

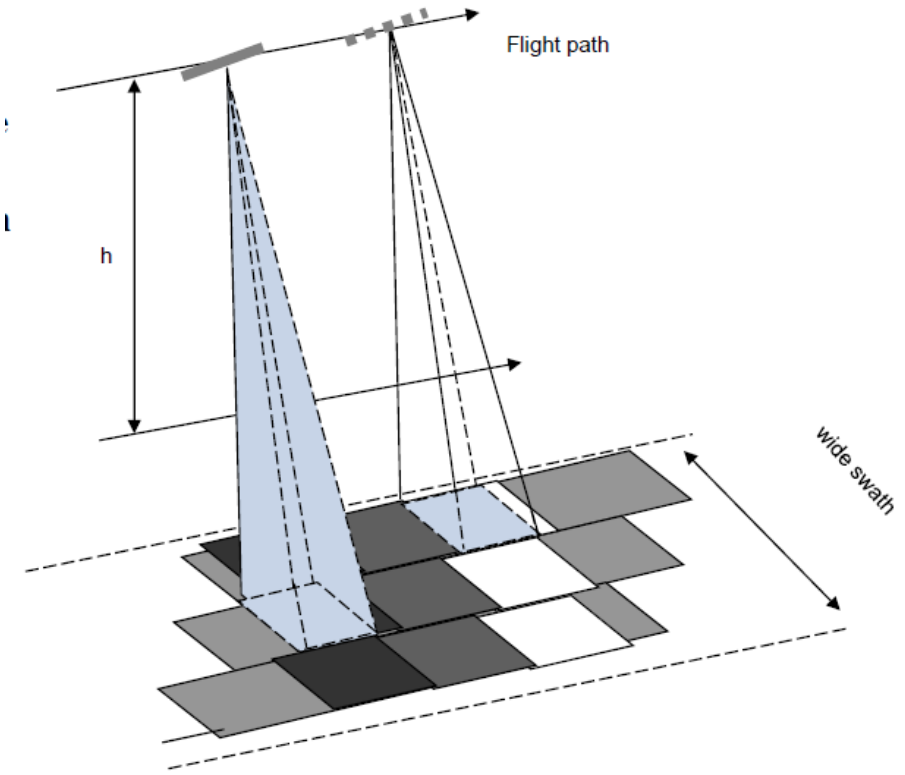

Figure 1.14: ScanSAR Mode configuration

the configuration I analyzed during my activity for radar corner reflector detection, as explain in Chapter 6. In particular I examined images from European Sentinel Constellation, described in detail in Chapter 2, in Interferometric Wide (IW) Swath configuration, that is a particular ScanSAR Mode. The IW mode acquires data with a 250 km swath at 5 m by 20 m spatial resolution and captures three sub-swaths using Terrain Observation with Progressive Scans SAR (TOPSAR). Using TOPSAR technique the beam is electronically steered from backward to forward in the azimuth direction for each burst, avoiding scalloping and improving the homogeneity of the image throughout the swath [11]. This is the main reason why I used these type

of images for my work, concerning corner reflector detection. IW mode has the same coverage and resolution as ScanSAR, but with a nearly uniform Signal to Noise Ratio and Distributed Target Ambiguity Ratio. Each sub-swath consists of a series of bursts that are processed separately and then resampled to a common pixel spacing grid in range and azimuth, to reduce overlapping between adjacent bursts and to preserve phase information. The main characteristic of IW swath Mode are listed in the Table 1.2 [12]. I used images in Level-1 Single Look Complex (SLC).

Characteristic	**Value**
Swath width	250 km
Incidence angle	29.01°-46°
Sub-swaths	3
Azimuth steering	0.6°
Azimuth and range looks	single
Polarization options	Dual (HH+HV,VV+VH)
Maximum Noise Equivalent Sigma Zero	-22dB
Radiometric stability	0.5dB
Radiometric accuracy	1dB
Phase error	5°

Table 1.2: Characteristics of Interferometric Wide swath mode

Level-1 SLC products consist of focused SAR data, geo-referenced using orbit and attitude data from satellite and provided in slant-range geometry, that is the natural radar observation.

Concerning the electromagnetic spectrum range for SAR it is usually between X band (7-12 GHz) and L band (1-2 GHz). When an electromagnetic wave reflects off a surface, there are three properties of the surface taking into account: the dielectric constant (or permittivity ϵ), the roughness (root-mean-square height relative to a smooth surface) and the local slope. The amplitude of radiation backscattered depends more on the roughness than on the chemical composition of the scatterers

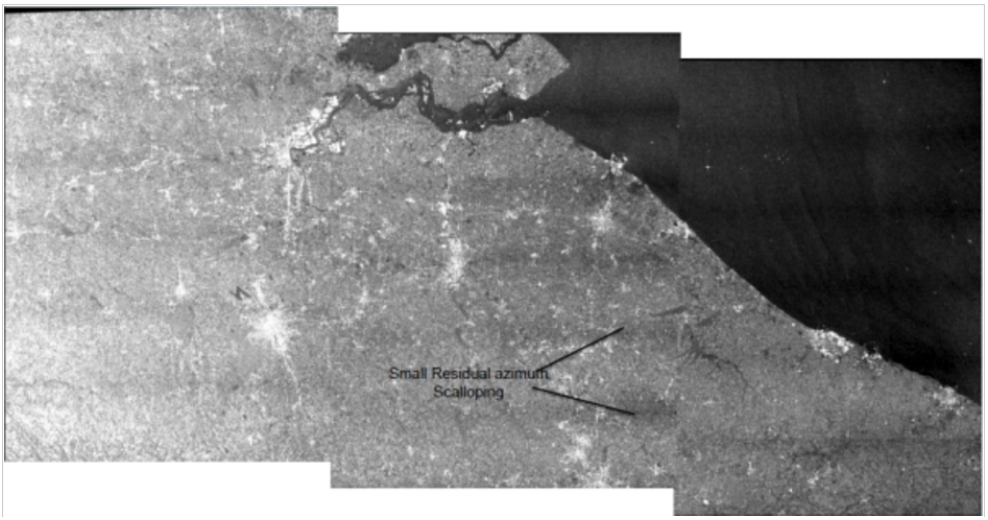

Figure 1.15: IW sub-swaths de-burst and merged

on the terrain. A smooth surface acts like a mirror, reflecting the wave at an angle equal and opposite to the incidence angle θ and therefore it appears in the SAR image as black, since the radiation is mainly mirrored away from radar. Following the Rayleigh criterion a surface is smooth if:

$$h < \frac{\lambda}{8\sin(\theta)} \tag{1.5}$$

where h is the surface roughness, λ is the wavelength of the wave and θ is the incidence angle. Therefore in order to clearly detect a radar reflector in a SAR image, the roughness of background on which it is placed is very important. Typically, exposed rocks and urban areas show strong amplitude of the radiation backscattered making harder the reflector detection, while smooth flat surfaces (like quite water basins) show low amplitudes and they are better suited for reflector deployment for images calibration. In the Chapter 6 I present a study to identify the best background for radar reflector deployment in an urban area and a comparison with

other devices placed on a desert area.

1.4 SLR Application on GNSS and Earth Observation

Radio-navigation satellites are tracked by microwave signals that are affected by ambiguities, signal perturbations from ionosphere and clock biases which limit the accuracy to ∼1 m (broadcast data [13]). Current tracking accuracy of SLR technique, to passive targets, is approximately $\sim 1 \div 10$ cm and using LRAs on such satellites will first improve their positioning and orbit tracking. The enhanced ranging accuracy, along with the independence of SLR from microwave technique, gives an important validation and calibration of GNSS orbit quality. This approach has been used successfully, so far, on GPS, GLONASS and Galileo In Orbit Validation Element (Galileo In Orbit Validation Element (GIOVE)) A/B satellites. SLR range measurements from various stations have been compared with GNSS orbit derived from microwave tracking data in order to accurately calibrate them [14, 15]. Being an autonomous technique from the basic radiometric tracking, SLR doesn't depend on atomic clocks on board of the satellites; therefore the effects of clock modeling can be separated from the orbit modeling and this aspect helps to better understand current errors in GNSS orbit prediction. For example SLR has been used to identify not modeled systematic effects, such the solar radiation pressure. Some studies have shown how an improvement on solar radiation pressure model, into GNSS orbit modeling, could improve GNSS orbit accuracy [14, 15]. Moreover SLR can be used to check clock performance.

As mentioned in section 1.2, GNSS is also fundamental to develop and maintain

the Temps Atomique International, along with the technique of Two-Way Satellite Time and Frequency Transfer (using telecommunication satellites). Temps Atomique International gives a time standard used worldwide and it is realized by a set of atomic clocks distributed around the world that need to be compared with precision and accuracy. This comparison is called "Time Transfer" and provides at each epoch the synchronization errors between clocks. The Time Transfer principle consists in a connection between two or more clocks using GNSS receivers and their messages. Analyzing GNSS observations on a clock 1 it is possible to determine the synchronization between this clock, and the satellite clock and therefore the GNSS reference time scale, whose information is in the navigation message. Doing the same with another clock it is possible to synchronize these two ground clocks because for both the satellite is the same. The accuracy of this technique is, currently, of few ns, but it can go down to 1 ns with Two-Way Satellite Time and Frequency Transfer and using a third microwave signal the accuracy can bring down to $\sim$ 100 ps. However optical techniques have better performance and could reach an accuracy of $\sim$ 50 ps over 10 days (an example is the T2L2 experiment [16]).

The principle is the same of GNSS above described but it uses time tagged laser pulses, of few ps length, sent to the satellite and received back. At the ground station, a timer registers start and arrival times of the pulse and on the satellite a detector tags the time of arrival of the pulse. The difference $(t_{start} + t_{arrival})/2 - t_{sat\_arrival}$ plus propagation delays, gives the synchronization error between the clock at the ground station and the atomic clock on board the satellite. Doing the same for a second clock in another laser ranging station, it is possible to synchronize these two clocks. Fig.1.16 gives a schematic view of the system. Unfortunately laser tracking, though less sensitive to propagation effects in the atmosphere, is strongly dependent on weather conditions and this doesn't allow daily clock comparison as GNSS does.

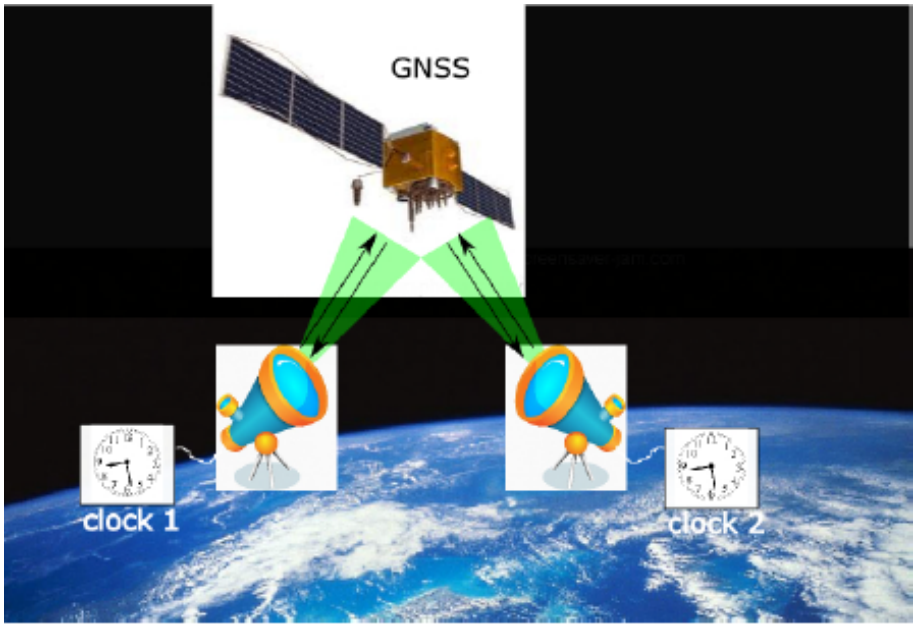

Figure 1.16: Schematic view of SLR time transfer

However the use of both techniques, will improve the accuracy of the time scale provided worldwide. As a consequence, a more accurate time scale transfer will make possible also a more accurate positioning.

Tracking of GNSS satellites plays not only an integral role on the formulation of the ITRF, but it is also the means by which the ITRF is distributed globally so that users can link their measurements into the Reference Frame. SLR in particular uniquely defines the origin (geocenter) and, together with Very Long Baseline Interferometry, the scale of length of the ITRF, as explain in section 1.1. Each of the techniques contributing to the ITRF measures a different observable quantity (optical versus radio, range versus range rate, terrestrial versus celestial, etc.) and hence has a different set of systematic errors. Careful combination of these data tries to exploit the strengths of each while mitigating the weaknesses. SLR is the only optical technique and the only one providing a direct measurements of

station-to-satellite ranges. As such, it s relied upon for calibration and validation of other techniques including altimetry and GNSS. The long-term goal is to define and maintain an ITRF with an accuracy of 1 *mm* and a stability of 0.1 *mm/year* over a 10-year period [17], and distribute it worldwide.

SLR was also used to track EO satellites from the first ERS satellite. Actually EO satellites equipped with retroreflector arrays and tracked by ILRS are: Cryosat-2, GRACE-A and B, Jason-2, Sentinel-3A, TanDEM-X and TerraSAR-X[2]. Some of these missions have the aim of measuring small secular changes of distance (such as sea-level thickness or surface elevation of ice sheets) and therefore laser ranging is used for calibration of on board altimeter or navigation system and as support of Precise Orbit Determination. Moreover on these satellites SLR is often combined with measurements from DORIS and GPS but it can also provide an essential independent tracking data type.

[2]https://ilrs.cddis.eosdis.nasa.gov/missions/satellite_missions/current_missions

Chapter 2

G-CALIMES Project

G-CALIMES, is a co-funded multi-year contract implementing a technological development project between INFN and the Italian Ministry of Defence, within the framework of the European Copernicus[1] Program. The aim of G-CALIMES is the absolute inter-calibration of three different positioning techniques: SLR, Radionavigation (GNSS) and SAR technology, for the benefit of European Galileo and Italian COSMO-SkyMed programs. Overall, this work is applicable to both COSMO-SkyMed first and second generation (under preparation) and to others EO programs like Sentinels missions.

The activity, carried on at the SCF_Lab[2] of LNF, consists in development and performance-testing of terrestrial and space instrumentation based on radar and laser retroreflectors for space and ground segments. The project goal is to improve the absolute positioning of COSMO-SkyMed constellation and its terrestrial maps, its co-location with GNSS, all with respect to the ITRF. Phase 1 of G-CALIMES started in 2014 and regarded the design and characterization of a satellite payload

[1] http://www.copernicus.eu/

[2] http://www.lnf.infn.it/esperimenti/etrusco/

(described in detail in Chapter 4) to be mounted on COSMO Second Generation satellites together with a feasibility study and realization of a ground-based device (presented in Chapter 3). Right now this Phase is concluded and Phase 2 is starting and continues until 2019. It will involve the complete characterization of ground-based device and development of a terrestrial network by selecting the most suitable sites for deployment of the device in accordance with the Italian Ministry of Defence, to perform positioning measurements exploiting the three different techniques. In this Chapter I describe in detail GNSS and EO constellations that benefit from G-CALIMES project and on which my research activity has been focused.

2.1 Galileo constellation

Galileo is Europe's global navigation satellite system, providing a highly accurate, guaranteed global positioning service with accuracy less than 10 cm under civilian control. It is inter-operable with GPS and GLONASS, the two other global satellite navigation systems. ESA's first two navigation satellites, GIOVE-A and –B, were launched in 2005 and 2008 respectively, reserving radio frequencies set aside for Galileo by the International Telecommunications Union and testing key Galileo technologies. Then on October 21 2011 the first two of four operational satellites designed to validate the Galileo concept in both space and on Earth came. Two more followed in 2012, completing this In Orbit Validation (IOV) phase. In August 2013 the phase of testing of Public Regulated Service, a high-precision positioning service designed to provide data for the development of sensitive applications, designed specifically to authorized users by national governments began. In August 2014 the Full Operational Capability phase, launching satellites number 5 and 6 started . At the moment 18 satellites are operative. The fully deployed Galileo sys-

tem consists of 30 satellites (27 operational + 3 active spares), positioned in three circular Medium Earth Orbit (MEO) planes at 23222 km altitude above the Earth and at an inclination of the orbital planes of 56° above the equator, separated by 120° longitude. Once this is achieved, Galileo navigation signals will provide good coverage even at latitudes up to 75° north, which corresponds to the North Cape and beyond. The large number of satellites together with the optimization of the constellation, and the availability of the three active spare satellites, will ensure that the loss of one satellite has no discernible effect on the user.

Two Galileo Control Centers (Fucino, Italy and Oberpfaffenhofen, Germany) have been implemented to ensure the control of satellites and to perform the navigation mission management. Data provided by a global network of Galileo Sensor Stations will be sent to the Galileo Sensor Center through a redundant communications network. The Galileo Control Centers will use the data from the stations to compute the integrity information and to synchronize the time signal of all satellites with the ground station clocks. As a further feature, Galileo is contributing to a global Search and Rescue function. To do this, each satellite is equipped with a transponder, which is able to transfer the distress signals from the user transmitters to the Rescue Co-ordination Centre, which will then initiate the rescue operation. At the same time, the system will provide a signal to the user, informing him that his situation has been detected and that help is under way. Altogether Galileo will provide five levels of services with guaranteed quality which marks the difference from this first complete civil positioning system.

In navigation, clocks are the driving factor for accurately determining positions. Each of the 30 satellites in the Galileo system have two type of clock on board: Rubidium Atomic Frequency Standard and Passive Hydrogen Maser. The clocks use different technologies, but work with the same principle - if you force atoms

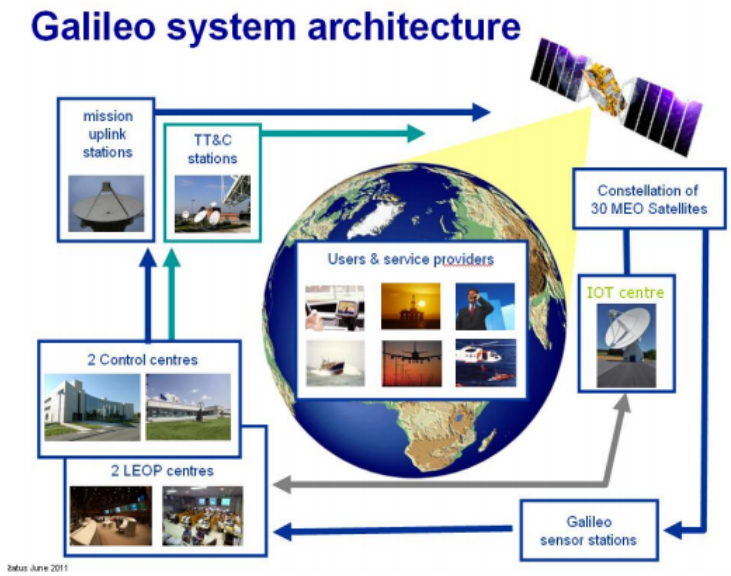

Figure 2.1: Galileo system architecture

to jump from one particular energy state to another, it will radiate the associated microwave signal at an extremely stable frequency. They keep time to within a few hundred-millionths of a second per day and this accuracy allows you to resolve your position anywhere on the Earth's surface.
Satellites are also equipped with LRA, as show in Fig.2.2.

Originally, the first Galileo satellite for orbit validation GIOVE-A, was planned to be equipped with a pair of identical LRA separated by some distance on the nadir-facing side of the spacecraft. The final design deviates from this original approach, whereby the two patches have been co-located and form one integrated array of 76 coated cubes with a diameter of 27 mm each. The overall shape is trapezoidal. Fig.2.3 shows the LRA of IOV satellites at the SCF_Lab, provided by ESA for testing activity.

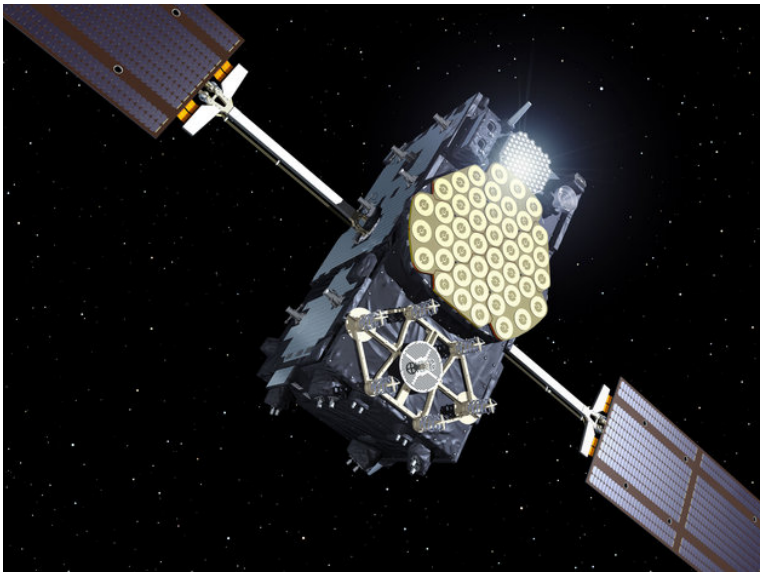

Figure 2.2: Galileo satellite

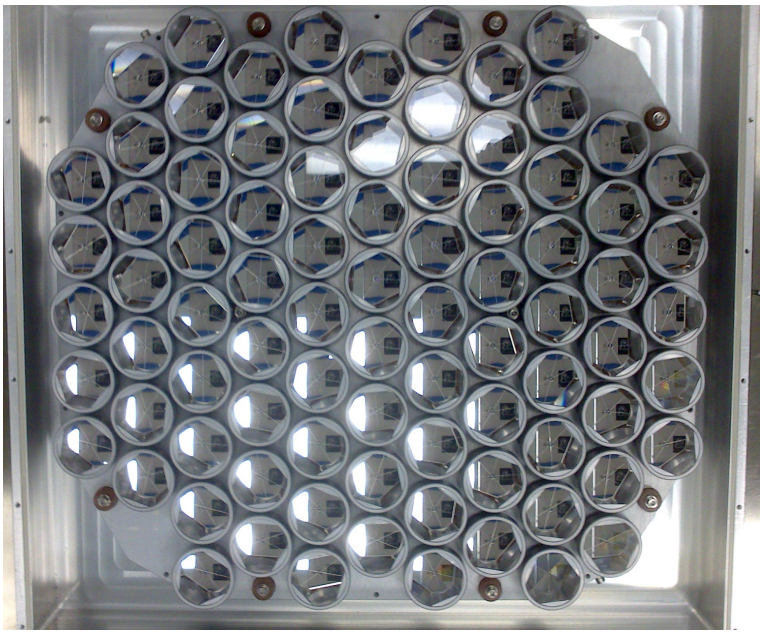

Figure 2.3: LRA Galileo IOV satellite structure at the SCF_Lab

2.2 Earth Observation Satellites

In this section I report a description of the main satellite constellations for Earth Observation and Monitoring: the Italian COSMO-SkyMed and the European Sentinels missions.

2.2.1 Cosmo-SkyMed Constellation

COSMO-SkyMed is the system for satellite EO designed for dual purposes: civil and military. His four satellites are able to peer at the Earth from space meter by meter, day and night, in all weather conditions. Therefore it is designed to prevent landslides and floods, to coordinate relief efforts in the event of earthquakes or fire and to control critical areas. Developed by Agenzia Spaziale Italiana (ASI) and the Italian Ministry of Defence, COSMO-SkyMed is based on a constellation of four identical satellites, equipped with SAR, working in X-band. The system is able to make up to 450 shots per day of the Earth's surface, equal to 1800 radar images, every 24 hours. The orbit characteristic are summarized in the Table 2.1. Sun-synchronous

Orbit type	SSO
Inclination	97.86°
Nominal Height	619.6 km
Revolutions per day	14.8125
Orbit Cycle	16 days
Eccentricity	0.00118
Argument of perigee	90°
LTAN	6:00 a.am.
Phasing	90°

Table 2.1: COSMO-SkyMed orbit characteristics

Orbit (SSO)s are medium-low near polar orbits, exploiting perturbations due to

non-sphericity of the Earth to maintain a constant orientation of the orbit plane respect to the Sun. The Longitude Time of the Ascending Node (LTAN) equal to 6 a.m. means COSMO-SkyMed orbit is a particular SSO namely dawn-dusk. Along this orbit the local mean solar time passage for equatorial longitudes is around sun-rise or sunset, therefore satellite rides the terminator between day and night. This configuration is particulary useful for EO satellites because solar arrays are always illuminated (easing thermal control system) and satellites survey the Earth surface always with the same Sun illumination condition.

In nominal conditions, the four satellites of COSMO-SkyMed are equi-phased in the same orbital plane as shown in the Fig.2.4. This configuration provides at least two opportunities in one days to access the same target site on the Earth surface under different observing conditions (typically around 6 a.m. and 6 p.m. local time). The interferometric configuration instead consists of two satellites placed in different orbit plane (0.08°) with 20" of separation, corresponding to an along-track separation of 151 km.

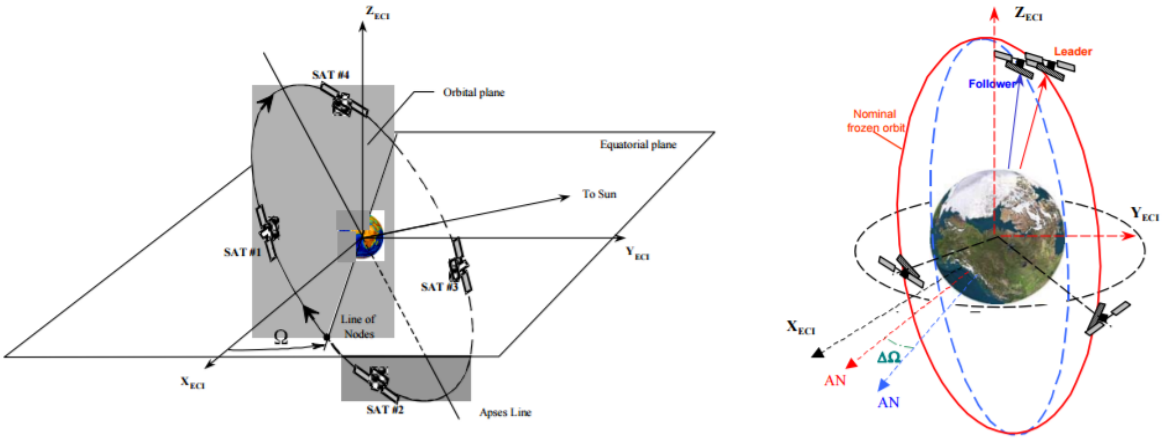

Figure 2.4: Left, Cosmo-SkyMed nominal configuration. Right, Interferometry tandem configuration

The real advantage of COSMO-SkyMed is the extraordinary flexibility of use. Radar can operate in:

- Spotlight mode: focusing on an area of 10x10 km and observing it with a resolution down to the individual meter
- StripMap: swath of 40x40 km or 30x30 km with a geometric resolution of 3 or 15 m respectively, depending on acquisition mode
- ScanSAR: swath of 100x100 km or 200x200 km with a geometric resolution of 30 or 100 m respectively, depending on acquisition mode

A very short time is required to configure the constellation in order to obtain desired images of the area: from 72 hours when operating under routine conditions, up to less than 18 hours in emergency conditions. Another strength is the short revisit time (the interval between two passages on the same point), less than 12 hours, which allows to constantly monitor the situation in a particular area.
The first satellite of the constellation was launched on June 7, 2007 and the second on December 9 of the same year. The third satellite started on October 25, 2008. The system was completed November 5, 2010 with the launch of the fourth and final satellite. Currently the second generation of COSMO-SkyMed is under development and the SCF_Lab is proposing CORA payload as new LRA on board of these satellites.

2.2.2 Sentinel constellation

Sentinels missions have been developed in the framework of European Copernicus Program with the aim of land, ocean and atmospheric monitoring. Each Sentinel mission is based on a constellation of two satellites to fulfil revisit and coverage

requirements, providing robust data sets [16]. The first satellite was launched on April 2014 and actually there are 4 satellites in orbit: Sentinel-1A and B, Sentinel-2A and Sentinel-3A. The entire constellation will consist of 10 satellites:

- Sentinel 1-A and 1-B, equipped with radar for land and ocean services, emergency mapping support in the event of natural disasters and climate changes monitoring

- Sentinel 2-A and 2-B, for multispectral high-resolution imaging, dedicated to land monitoring to provide imagery of vegetation, soil and water cover, inland waterways and coastal areas

- Sentinel 3-A and 3-B, with multi-instruments to measure sea-surface topography, sea and land surface temperature, ocean and land colour with high accuracy and reliability

- Sentinel 4, a payload devoted to atmospheric monitoring that will be embarked upon a Meteosat Third Generation-Sounder satellite in geostationary orbit

- Sentinel 5, a payload that will monitor the atmosphere from polar orbit aboard a MetOp Second Generation satellite

- Sentinel 5-P, developed to reduce data gaps between Envisat and Sentinel-5. This mission will be dedicated to atmospheric monitoring

- Sentinel 6, will carry a radar altimeter to measure global sea-surface height, primarily for operational oceanography and for climate studies.

During my activity I analyzed SAR images from Sentinel-1A. It carries a C-Band SAR on a polar orbit and its main characteristics are summarized in the Table2.2.

Orbit type	SSO near-polar, circular
Inclination	98.18°
Nominal Height	693 km
Revolutions per day	14.5833
Orbit Cycle	12 days, 6 with two satellites
Payload	C band SAR
Centre Frequency	VV+VH,HH+HV
Polarization	6:00 a.am.
Incidence angle	20° - 45°
Radiometric accuracy	1 dB (3 σ)

Table 2.2: Sentinel-1A orbit characteristics

The satellite has four image acquisition modes, with different resolution and swath width:

- Strip Map Mode at 80 km swath and 5x5 m spatial resolution
- Interferometric Wide Swath Mode at 250 km swath and 5x20 m spatial resolution
- Extra-Wide Swath Mode of 400 km and 20x40 m spatial resolution
- Wave-Mode images of 20x20 km and 5x5 m spatial resolution (at 100 km intervals)

In the Figure 2.5 a picture of Sentinel-1A is shown.

Figure 2.5: Sentinel-1A satellite

Chapter 3

Instrumentation design and goals

This Chapter presents a detailed description of the instrumentation related to G-CALIMES project, designed and realized during my PhD research activity. In the section 3.1 I describe the new payload of retroreflectors named CORA, intended to be mounted on COSMO-SkyMed Second Generation satellites, with the aim of guaranteeing an accurate ranging measurement for every Laser Ranging station on Earth, optimizing the satellite tracking. At first I will show the optical simulations performed to choose CCR optical characteristics, continuing with mechanical design, frame structure and CCR housing, chosen to have a lightweight and optimized array. In the section 3.2 I describe the ground-based radar device named INCA, built to combine three different positioning techniques and perform inter-calibration measurements. Regarding INCA, I present a feasibility study I led in order to identify the more reliable and convenient configuration and a geometric simulation, to understand how returning signal from device is influenced by its correct deployment and alignment.

3.1 CORA design

EO constellations use retroreflector arrays to enhance their positioning accuracy, as explained in the section 1.4. They are equipped with solid coated retroreflectors that have a larger angle of acceptance respect to uncoated, as mentioned in the section 1.1.1. This feature is essential to take into account the reduced field of view of Low Earth Orbit (LEO) satellites (altitude orbit about 600 km) from Laser Ranging stations. However the close contact between fused silica and metal film, can generate temperature differences inside reflector, that create a variation in the index of refraction and consequently a degradation in the optical performances [18]. On the other hand uncoated CCR are affected by low thermal gradients but they have an angle of acceptance lower than coated and for this reason are used only for satellites on high orbits. These considerations led us to choose coated reflectors for CORA device, as explained in detail in the section 3.1.1. Moreover we tried to design a compact and lightweight array, compatible with performance and structural dynamics, being the payload's weight critical in space.

3.1.1 Optical simulations

A satellite orbiting at an altitude of $\sim$ 600 km has a VA varying between 25 and 50 μrad, as shown in the Figure 3.1, where the angular displacement in the FFDP is represented (for a detail description of FFDP see section 4.2). Such a wide variation in the relative movement between station and payload would require different kind of CCRs to cover the VA band. We proceeded however in a different way. Usually, given the altitude of a satellite, hence the VA, it is possible to define dimensions and DAO of CCR, by looking at the average intensity of its FFDP at that VA. We proceeded in the same way but applying that to the wider band of 25-50 μrad,

checking if the average intensity in this band was at an acceptable level (scaling from the reference intensity of LAGEOS satellite, previous tested at the SCF_Lab and reported in [18]).

Since for SLR the altitude of COSMO-SkyMed satellites is quite low, there are no severe requests on the intensity coming back to the stations, meaning that we can concentrate on the return of just one CCR. Different optical simulations were carried out, by commercial software CODE V, varying CCR front face diameter and DAOs, to define the characteristics for CORA CCR expressed in Table 3.1: DAO are put

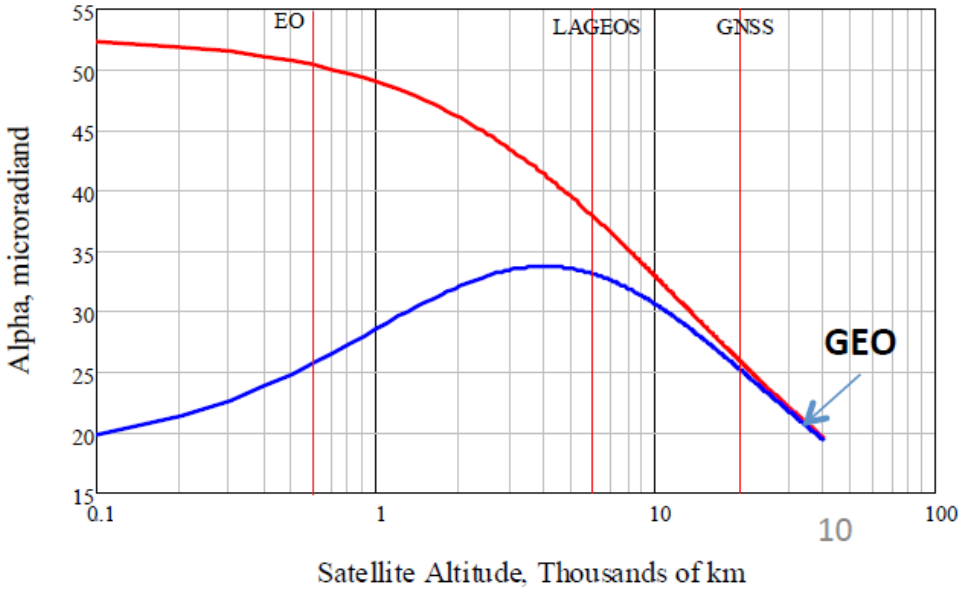

Figure 3.1: Relative velocity between satellite and station expressed in angular displacement in the FFDP

on all of the three retroreflector edges with a tolerance of $\pm$ 0.5 *arcsec*, which is the usual value for commercial CCRs. 1.8 *arcsec* was chosen in order to not reduce too much the intensity at the VA band. In the Fig.3.2 we compare the average intensity for a CCR with DAO on specification and those with $\pm 0.5 arcsec$ tolerances. The intensity in COSMO-SkyMed VA range is $0.98 \cdot 10^6\, m^2$ for DAO of 1.8 *arcsec*, while

Front Face diameter:	33 mm
Length	24 mm
DAO	3 x 1.8 $\pm$ 0.5 $arcsec$
Material	Suprasil 1
Coating	Silver

Table 3.1: CORA characteristics

it decreases at $0.94 \cdot 10^6\, m^2$ for 1.3 $arcsec$ and at $0,64 \cdot 10^6\, m^2$ for DAO of 2.3 $arcsec$.

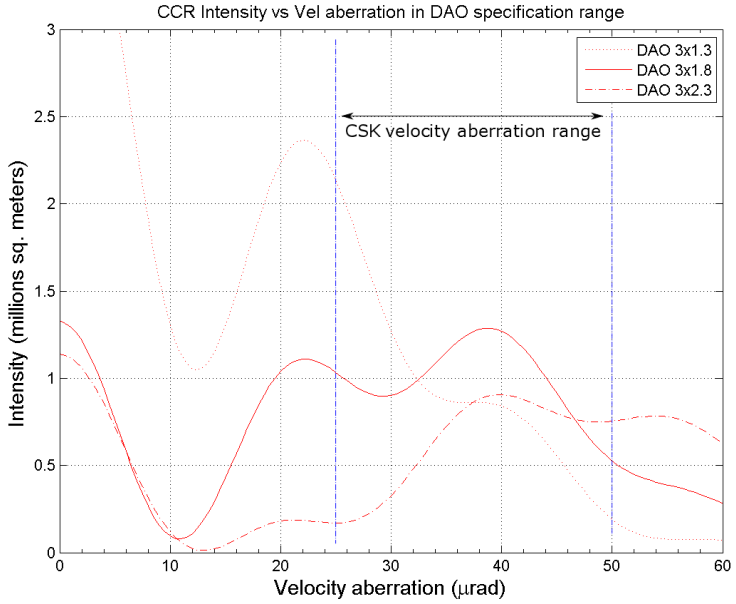

Figure 3.2: Average intensity of FFDP with different DAO

For a satellite on a LEO orbit with an inclination of about 90°, the inclination of the laser beam hitting its CCR front face will almost never be zero (zero being perpendicular to the CCR front face), but it will reach high values, as showed in the Fig.3.3. This makes the coating of CCR back faces a necessity. To reduce the effect of the thermal absorption of the Sun radiation on CCR performances, we chose

Silver as back coating, as opposed to Aluminum, which has a higher solar absorption. In addition, Silver has a higher laser reflectivity than Aluminum. In the following figures I show the FFDP of CORA CCR along with the plot of the average intensity at increasing VA. Simulations are performed with a 532 nm laser beam. Intensity values are defined in Optical Cross Section (OCS), which is a standard intensity unit for retroreflectors, [19]. CCRs chosen for the array differ from classic CCR

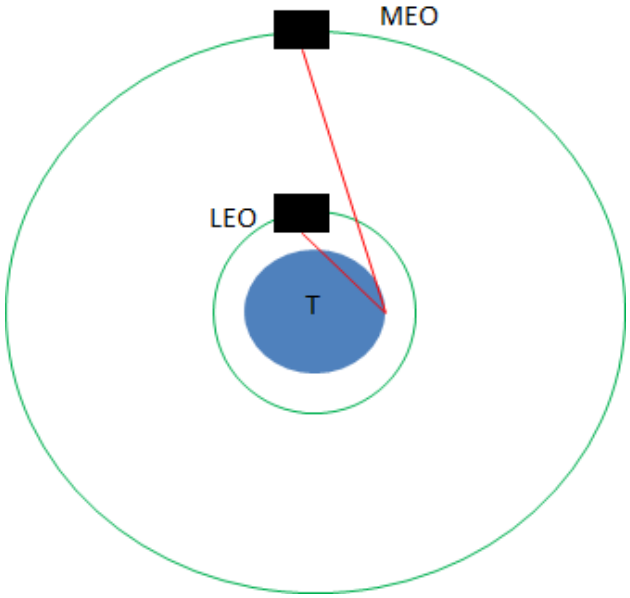

Figure 3.3: Schematic view of plane LRA on LEO and MEO

prism manufacturing for some protrusions, "tabs", they have on their cylindrical part. These tabs are not polished and connect CCRs with their holding system, as shown in the Fig.3.6. The optical specifications of CORA CCRs are:

- Surface Roughness 80/50 scratch/dig

- Front face flatness (peak-to-valley, not RMS) $\leq \lambda/8$ with $\lambda = 532\ nm$

- Three rear surfaces flatness (peak-to valley. not RMS) $\leq \lambda/10$ with $\lambda = 532\ nm$

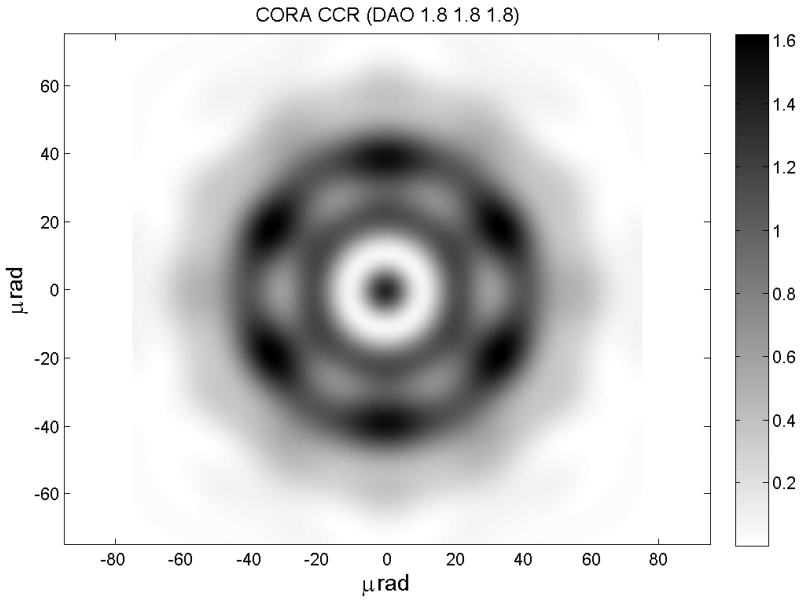

Figure 3.4: FFDP of CORA CCR

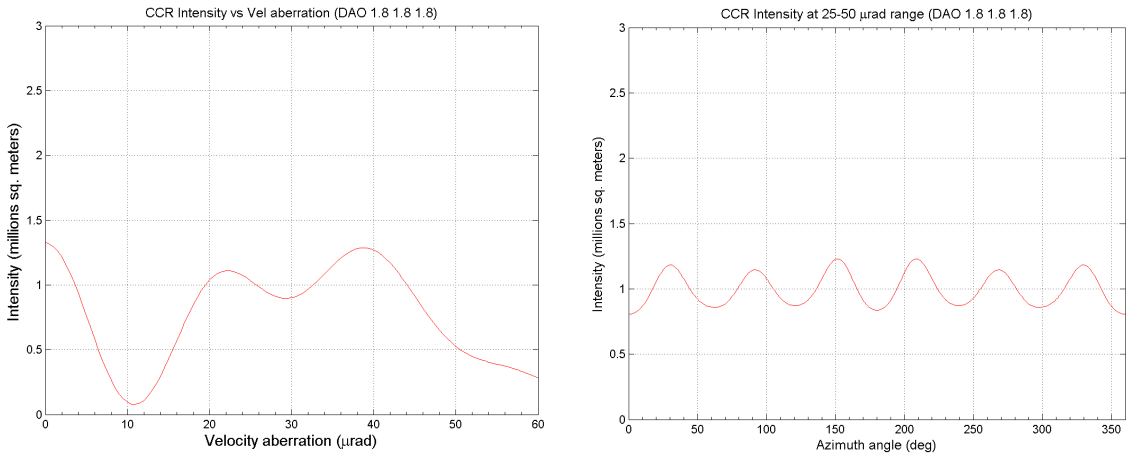

Figure 3.5: Left, CORA CCR average intensity at increasing VA. Right, CORA CCR intensity in the band 25-50 μrad

- Wavefront distortion emerging from the 90% of the CCR front face optically active (peak-to-valley, not RMS) $\leq \lambda/4$ with $\lambda = 532\ nm$

- Coating silver

- DAO of $1.8 \pm 0.5 arcsec$, on each of the three physical edges, as previously mentioned.

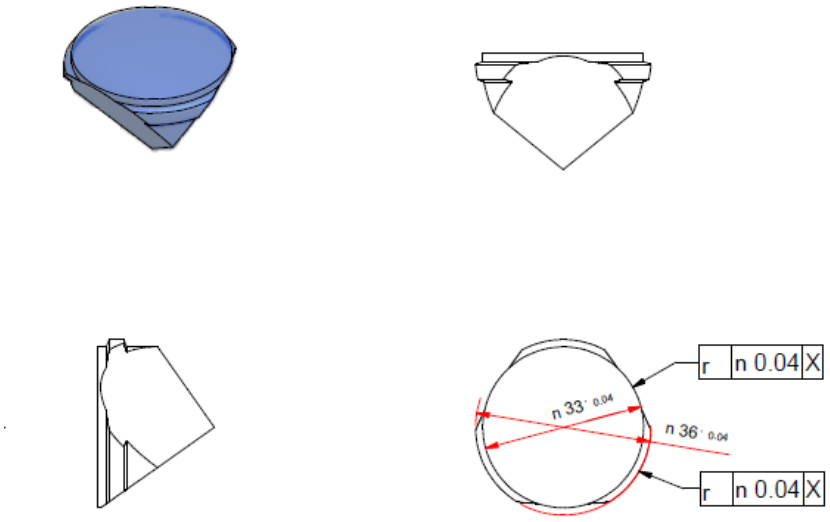

Figure 3.6: CORA CCR schematic view and dimensions

Fig.3.7 shows a picture of one of CORA CCRs.

As inclination of the laser beam on CCR front face from ground station could reach high values we decided to substitute a single CCR payload with a pyramid of CCRs. In this way is possible to increase the number of stations capable to track the satellite. Hence we chose a square based pyramid, with four CCRs on it and pyramid faces at an inclination with respect to its base of 45°. Fig.3.8 shows CORA average intensity over the range 25-50 μrad in the configuration presented in Fig.3.9.

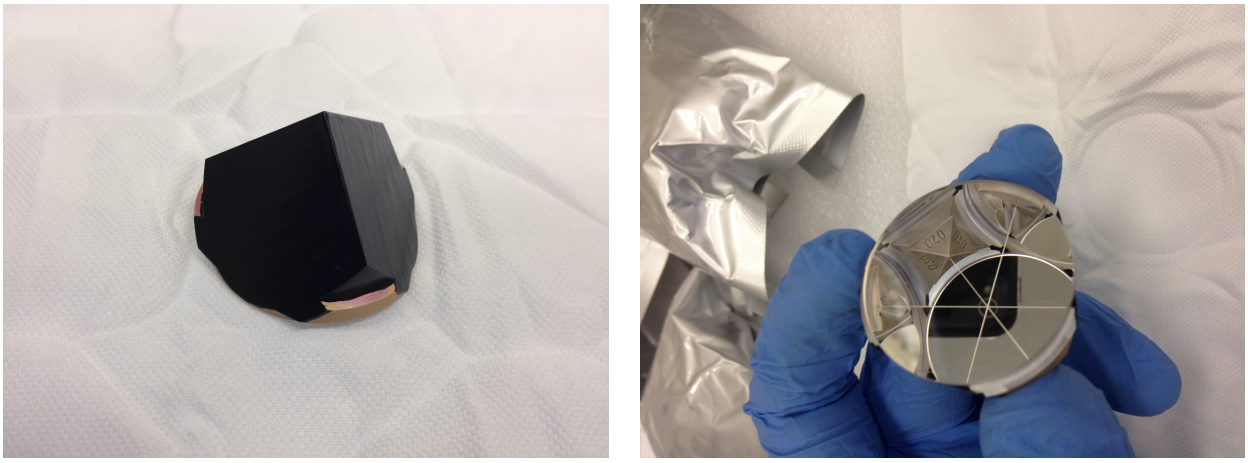

Figure 3.7: Left, CORA CCR back view. Right, CORA CCR front view

This simulation has been obtained rotating incident laser beam, at a fixed incidence angle, with respect to the vertical axis. It is clear how intensity is maximized when the inclination of laser beam is high respect to the vertical axis of CORA. Even in the case there would be high fluctuation depending on the direction; a maximum is reached as the laser hits directly one CCR.

3.1.2 Mechanical design

CORA has an Aluminum 6000 series square based pyramidal structure with sides at 45° inclination relative to the base, as mentioned before. The base square is [115 x 115] mm sized and the truncated pyramid height is 50 mm. The inner structure is empty to guarantee a lighter weight and has 4 holes on 45° sloped surfaces for CCRs holding (see Figure 3.10). This frame is closed with an Aluminum plate to ensure mechanical coupling with satellite surface. The Table 3.2 summarizes CORA frame mechanical features.

In order to assemble CCRs with the frame we needed first to mount the CCR

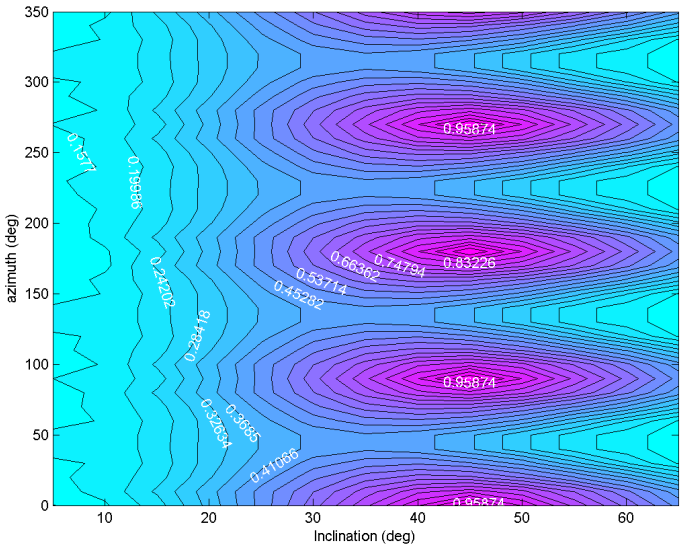

Figure 3.8: CORA average intensity over the range $25 - 50$ μrad

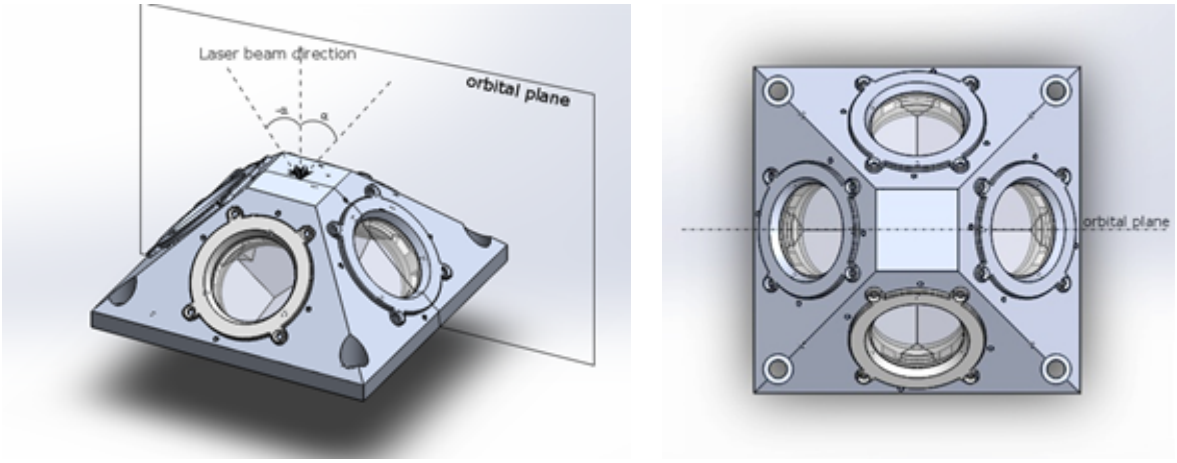

Figure 3.9: CORA in configuration used for simulation

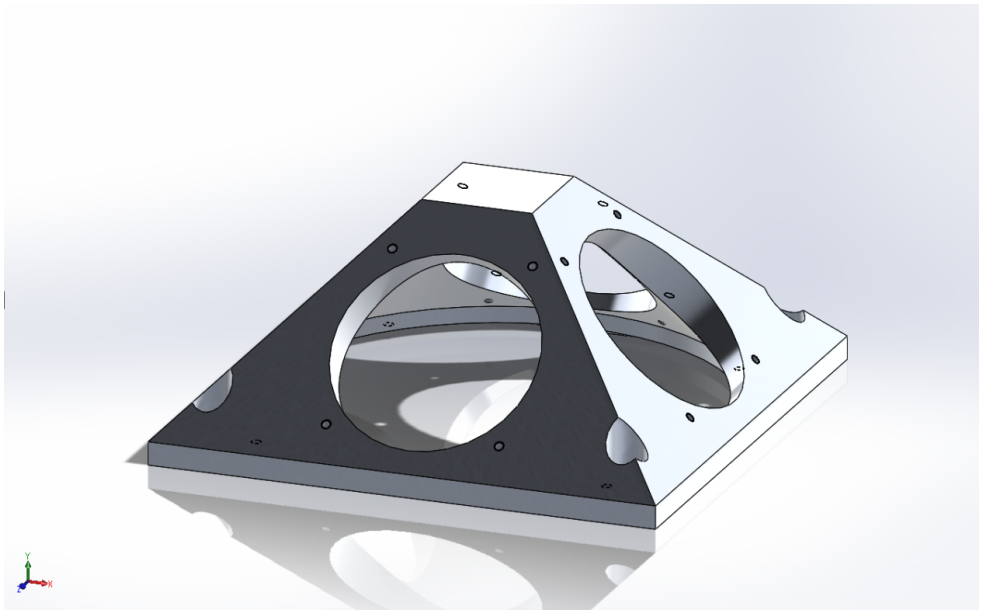

Figure 3.10: CORA frame structure

inside its housing then put the housing in the frame hole. This type of mounting has been chosen because at first we wanted to use the back-mounting technique, inheritance from LAGEOS and Apollo CCRs and highly thermally optimized, but the frame shape was too small to screw CCR from the inner surface. So, to keep the back-mounting technique, it is necessary to mount apart CCR and its rings inside the housing (see Fig.3.12) and then screws it on the frame. The housing assembly is composed by:

- Cylindrical housing
- 1 Fused silica 33 mm diameter coated CCR
- 2 KEL-F rings, called in the following upper and lower ring
- 1 Aluminum ring

Figures 3.11 and 3.12 show in detail CORA CCR housing.

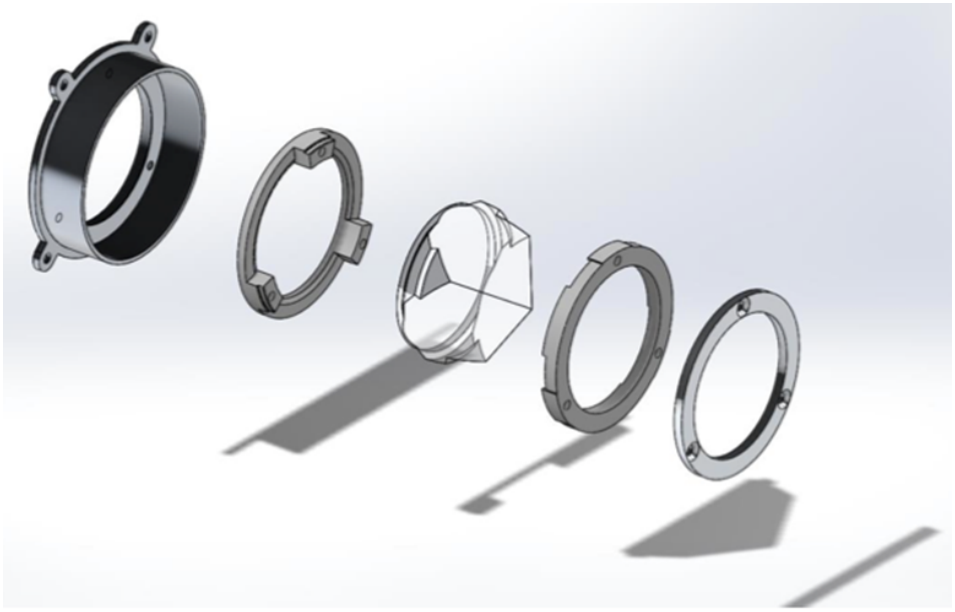

Figure 3.11: Housing, exploded view with, starting from the left: housing, upper KEL-F ring, CCR, lower KEL-F ring and Aluminum ring.

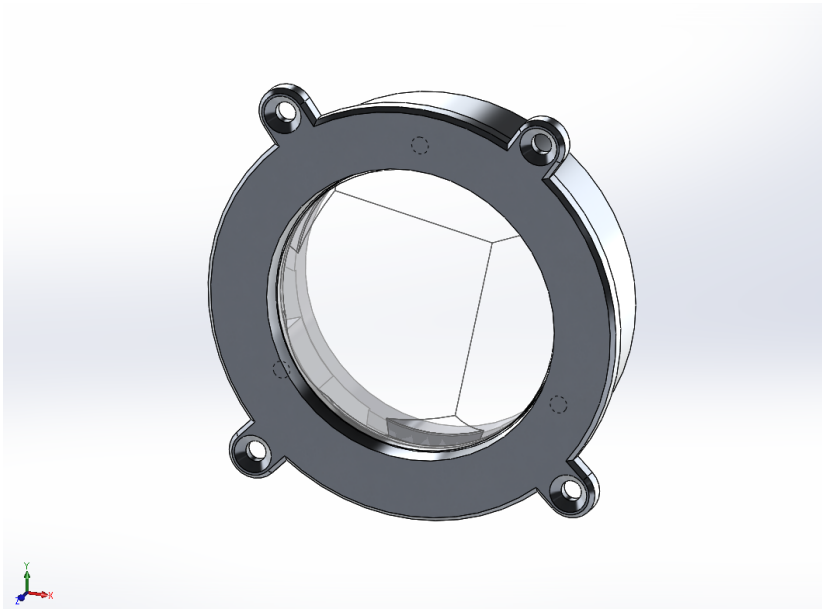

Figure 3.12: CCR housing assembly

Material	Al 6000
Weight	$\sim 200g$
Pyramid base side	115 mm
Pyramid height	50 mm
Pyramid edge angle	45°
CCR holes diameter	44.5 mm
CCR holding screws	3XM2
Housing holding screws	4XM2
Frame holding screws	4XM5

Table 3.2: CORA frame structure characteristics

KEL-F is a plastic material with low thermal conductivity and low hygroscopic potential used to reduce internal temperature gradients on CCR. These two rings are used to place CCR inside its cylindrical housing while an Aluminum ring on the rear of lower KEL-F ring, tightens the whole mounting system with three screws. The total structure with also CCRs installed is shown in the Fig.3.13 and it weights about 450 g. If we also consider the back closing plate the weight reaches about 500 g.

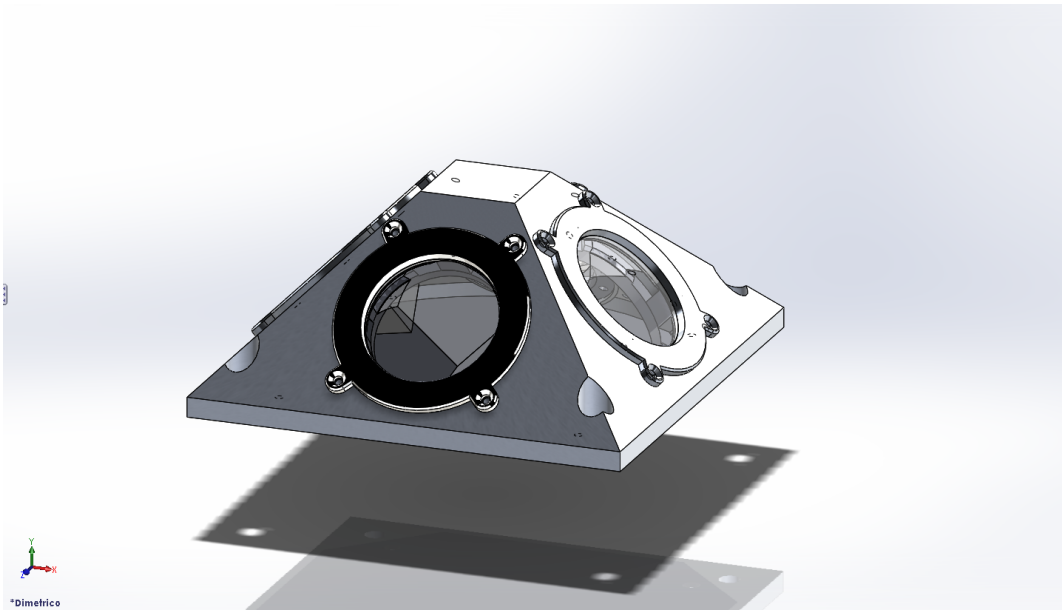

Figure 3.13: Cora assembly

3.2 INCA design

INCA consists of a trihedral radar reflector co-located with an optical CCR and equipped with a GPS/Galileo receiver. This new instrument inherits the main geometry from common popular reflectors but it has some innovations that make it unique and adaptable. Radar reflector concept is the same of laser CCR already described: this particular geometry retro reflects a microwave beam coming from an EO satellite and the reflector appears as a bright cross in the SAR image (the diffraction spectrum). For this reason radar reflector are used for geometrical calibration of SAR images.

The first step that led us to this choice for INCA design was a feasibility study, to determine the technically and economically more convenient configuration, operationally more simple, reliable and resistant. We started from the idea to build a CCR radar and optical at the same time. This concept was quickly left due to conflicting requirements on size and geometric accuracy imposed by SAR and SLR. The size required for the radar in fact is significantly greater than that required and implemented for the laser; moreover the geometric accuracy required for the radar CCR is much less than that required for the laser tracking. The accuracies required for optical CCR are: a flatness of retro-reflecting faces equal to $\lambda/10$ or better (typically λ is 532 nm or 633 nm), accuracy of the DAO respect to 90° equal to 0.5 $arcsec$ and accuracy of laser wavefront reflected $\lambda/4$ or better. On the other way, accuracies required for Radar CCR are proportional to the different λ of radar beam, which is much greater than optical beam (typically $\lambda = 2.5 - 3.7cm$ for X Band and $\lambda = 3.7 - 7.5cm$ for C Band).
An other possibility we thought was to build an hybrid hollow CCR with:

- an inner part of the cube corner, small about few centimeters, with optical quality

- the remainder part of the cube corner, order of the meter, with quality suitable to SAR.

This last option would create at least two negative technical issues:

- the outer part with radar quality, for its large size would cause mechanical (pressure and torsion) and thermal (temperature gradients) stress on the inside, changing optical functionality. This consideration is based on proven experience of optical FFDP measurements, made over 10 years at the SCF_Lab: the optical components are typically mounted with very mild constraints and it is known how the slightest pressure on the edge of the mirror causes a significant performance degradation of optical laser components

- continuous monitoring of cleanliness from atmospheric agents on the unified hybrid device could be too heavy and inconvenient: the accumulation of moisture and dust, which does not prevent the measure SAR, prevents or degrades decisively that laser. Therefore the prevention of rain accumulation on the optical inner part and the introduction of appropriate openings makes it necessary on that part. Practicing such openings makes the realization of the entire device technically complicated and expensive.

Therefore, after the assumptions from above we can state that the creation of a "unified INCA" (consisting of a retro-reflector radar and optical simultaneously) is not feasible, useful and convenient in the framework of G-CALIMES work program. For these reasons we decided to realize an optical CCR separated from radar CCR, to be able to easily remove and inspect it and upgrade in time desired and or if necessary. The final INCA configuration built consisted of two geometrically co-located CCRs:

- **Radar CCR**
  - Material: Aluminum Anticorodal (TA16 UNI 3571) externally painted with Elcovir 35, an electro-conductive black paint
  - Structure: 1 meter trihedral corner reflector
  - Dimensions: [420x1000x1000] mm
  - Design inheritance: permanent passive scatterers for SAR
- **Laser/optical CCR**
  - Material: fused silica, Suprasil 1
  - Structure: solid and uncoated CCR
  - Front face diameter: 64.4 mm
  - Length: 48.1 mm
  - DAO: $\pm 0.5mm$
  - Design inheritance: terrestrial (Leica/Nikon total station) and ILRS station survey/alignment metrology

The three faces of radar CCR are 90° each other and linked through three long and three short L–shaped section bars, along the adjacent edges. This structure is screwed at the "Bascula", a circular steel plate, as shown in the Figure 3.14. The whole structure is anchored to the ground with a three feet base with 3 through holes each. The optical CCR is a commercial one, not space qualified, and it is located on the support structure, with its tip co-located respect to radar reflector's tip and it is removable. The GPS/Galileo receiver is located along the same radar and optical CCR's vertical axis and it is screwed on a dedicated anchor bolt, as shown in the Figure 3.15. It is used to make geo-referencing measurement and calibration and

therefore it can be mounted and dismounted quickly and easily. The maximum dimensions of INCA are $[880x1420x1420]mm$ and the weight is less than 45 kg.

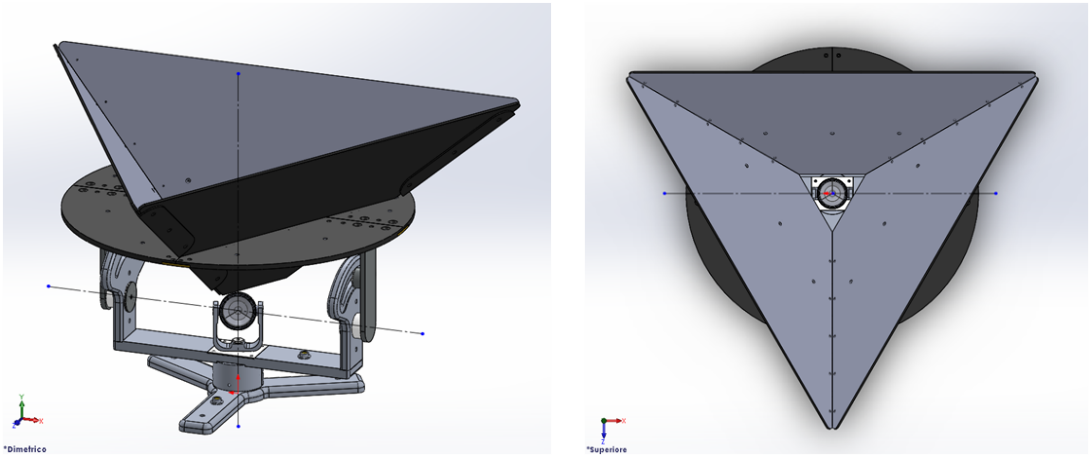

Figure 3.14: Left, INCA front view. Right, INCA top view, with vertical and horizontal rotation axes. *Property of INFN and Italian Ministry of Defense. Do not copy, reproduce, circulate without written authorization of INFN and Italian Ministry of Defense*

The entire device is designed to rotate 360° around the vertical axis using a Polytetrafluoroethylene (PTFE) bearing located at the bottom. In addition, the radar CCR can rotate around its horizontal axis by an eyelet which is fixed by a bolt, to easily point it to the satellite. Optical CCR can rotate around both its vertical and horizontal axes. Elcovir 35, used for painting radar reflector's external faces and circular plate, is an electro-conductive black paint and antistatic metallic-based with dispersion of thermoplastic resins, which has the purpose of shielding GPS receiver from electromagnetic waves and thereby avoid the phenomenon of multipath [6] (the propagation phenomenon that effects radio signals reaching the receiving antenna by two or more paths, causing interference and shifting phase). This is an additional measure, because the receiver is already multipath free. It is an advanced GNSS receiver (Topcon GR-5) and it is controlled by a field controller

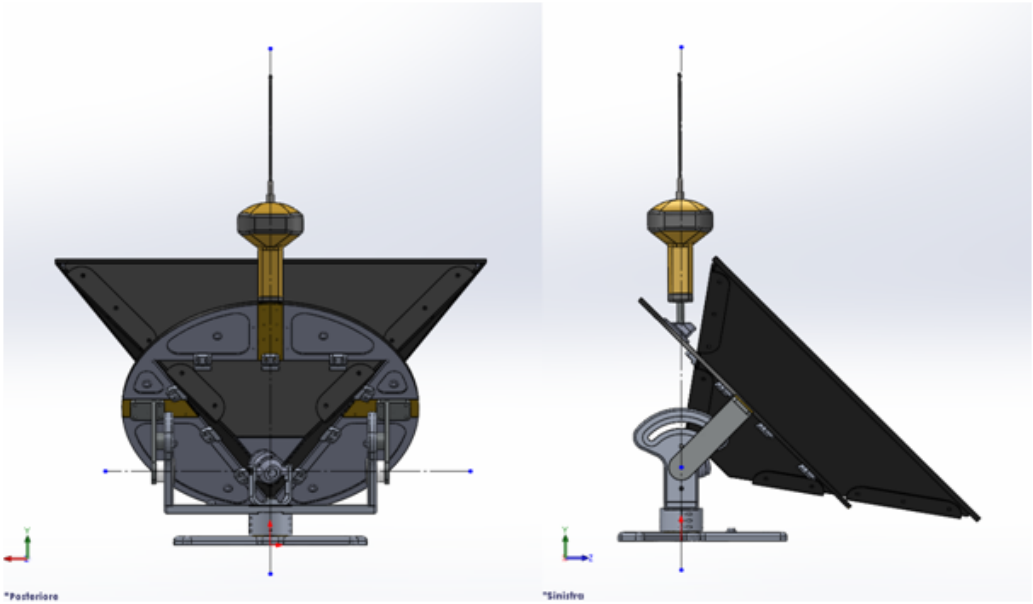

Figure 3.15: Left, INCA back view. Right,INCA lateral view, with GPS receiver. *Property of INFN and Italian Ministry of Defense. Do not copy, reproduce, circulate without written authorization of INFN and Italian Ministry of Defense*

(FC-250). GR-5 features a patented technology with flexible and dynamic tracking methods to automatically select and track any available satellite signal, enabling users to receive the maximum number of signals and measurements at any given time. GR-5 is not only capable of receiving signals from the fully operational GPS and GLONASS constellations, but also has the ability to support all planned signals from developing systems such as Galileo, COMPASS/Beidou and QZSS.

In the list below main INCA features are summarized:

Figure 3.16: Left, GR-5 receiver. Right, FC-250 controller

- Pointing system: manually operated
- System can rotate around its vertical axis, performing a 360° arch, and around its horizontal axis, by 180°
- Graduated eye-readable azimuth and elevation angular scales
- Tips (corners) of radar and laser CCRs are coincident (co-located)
- Co-located tips of radar and laser CCRs stay fixed in local three-dimensional space during azimuth-elevation pointing

- Total weight $< 45kg$

3.2.1 Radar Cross Section simulations

The intensity of INCA returning signal is proportional to the Radar Cross Section (RCS) [20], that is a function on the effective CCR equivalent area A_e (the active reflective surface shown in the Fig.3.17) as described by the equation:

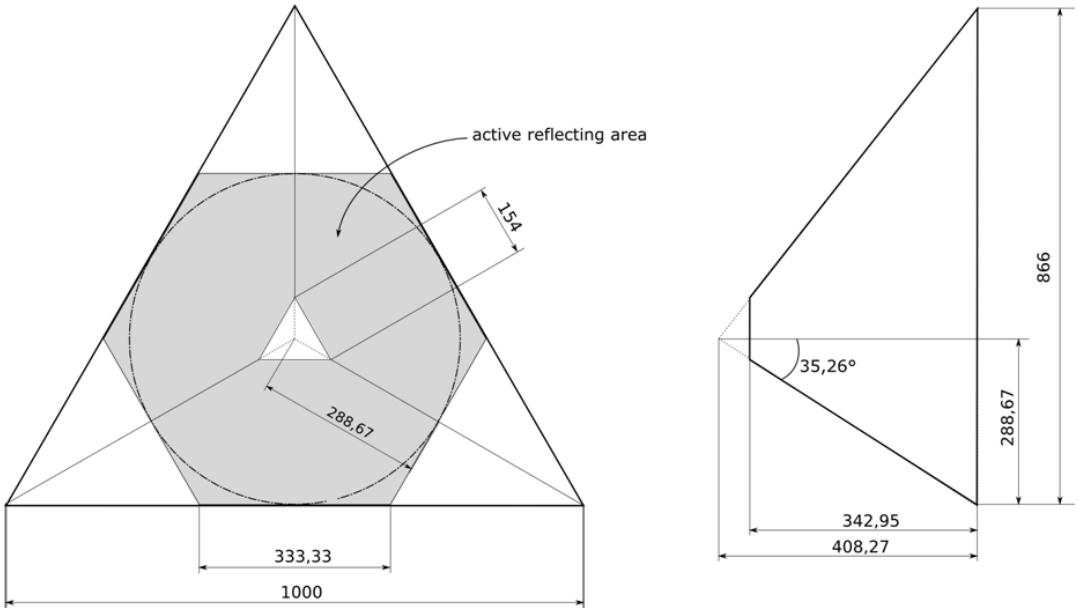

Figure 3.17: INCA active reflecting area

$$RCS = \frac{4\pi {A_e}^2}{\lambda^2} \tag{3.1}$$

where λ is the satellite wavelength. A_e depends on retroreflector geometrical dimensions by the law:

$$A_e = \frac{2}{3}A = \frac{2}{3}(\frac{\sqrt{3}}{4}l^2) \tag{3.2}$$

where A is the retroreflector geometrical area and l is the length of radar reflector edge of radar. If there is a perfect alignment between retroreflector and satellite, that means an accurate INCA pointing towards satellite in elevation and azimuth, A_e will be the maximum available ("normal" condition); but if there is a misalignment the reflective surface will decrease ("tilted" condition). Looking at Fig.3.18 and assuming a θ misalignment, on the satellite frame of reference the retroreflector edge l decreases with the law:

$$l' = l \times cos(\theta) \tag{3.3}$$

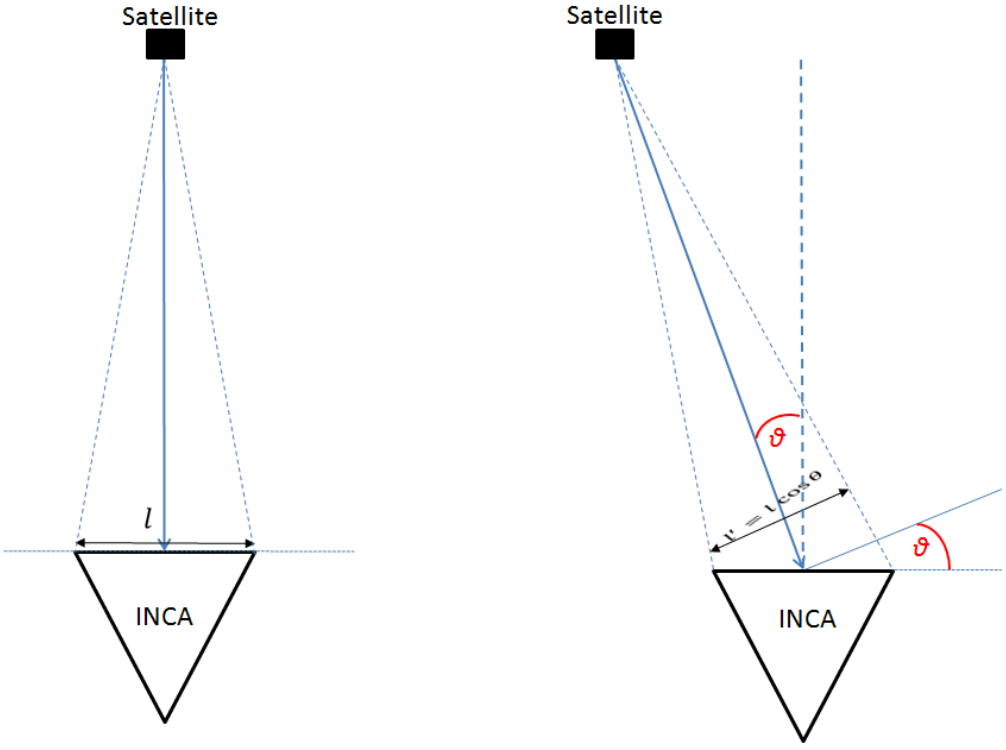

Figure 3.18: Schematic drawing of INCA alignment with satellite. On the left "normal" condition with INCA and satellite perfectly aligned, on the right "tilted condition" with INCA tilted by a θ angle respect to the "normal" condition.

Therefore a misalignment between INCA and satellite decreases the returning signal and hence reflector visibility in SAR images. The accuracy in this alignment depends on the instruments used to deploy and align INCA (compass and clinometer). For these reasons I conduct a simulation in order to study how the returning signal changes from the "normal" condition due to a misalignment. In this way I put some constraints on the minimum accuracy needed to point the reflector.
Firstly I define two functions $UNIT$ and $GAUSSIAN$, shown in the Fig.3.19: The spatial response $I(\theta, l)$ is defined as convolution product between $UNIT$ and

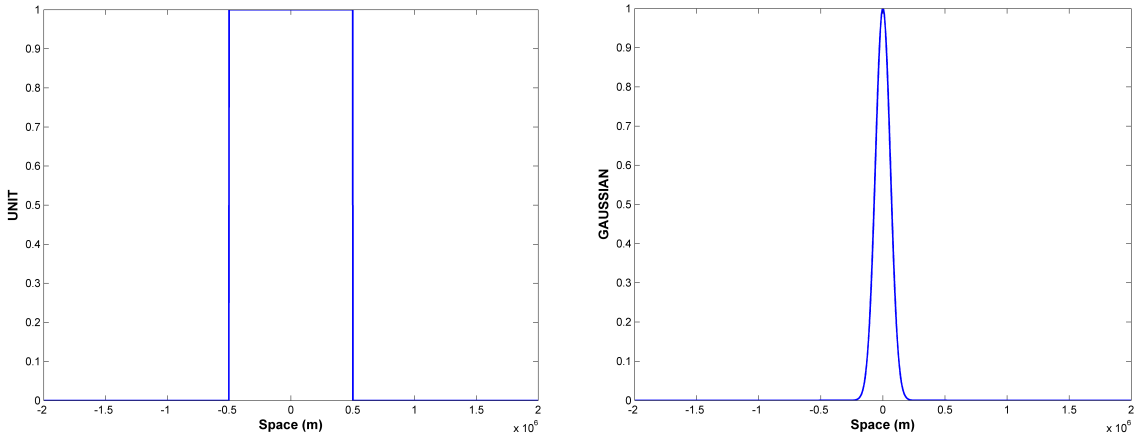

Figure 3.19: Left, $UNIT$: is equal to 1 in the range $[-l'/2; l'/2]$ and describes A_e depending on θ angle. Right, $GAUSSIAN$: has $\sigma = \lambda$ and depends on θ angle.

$GAUSSIAN$. Therefore the variation of returning signal R w.r.t. θ is:

$$R = \frac{\int I(\theta, l)dl}{\int I(\theta = 0, l)dl} p(\theta) \tag{3.4}$$

where $p(\theta)$ is a weight function defined as $(\frac{l'(\theta)}{l})^2$. Using: $l = 1m$ and $\lambda = 60mm$ (Sentinel wavelength) and computing with Matlab the equation 3.4 I obtained the response shown in Fig.3.20. The study proves that any significative decrease in

the INCA response is not expected within at least 10° from "normal" condition, or otherwise instrumentation used for INCA pointing must have an accuracy better than 10° (refer to section 6.2 for details about INCA deployment).

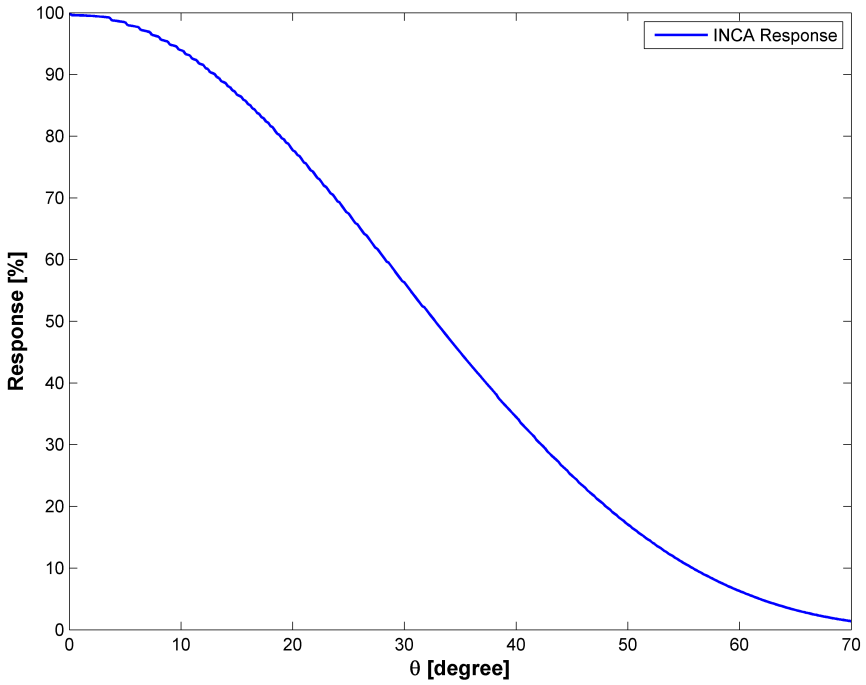

Figure 3.20: INCA response from "normal" condition as function of θ.

3.3 CORA and INCA design conclusions

In this section I summarize the main characteristics of CORA and INCA instrumentation. CORA payload was designed to be mounted on COSMO-SkyMed Second Generation satellites, with the aim of improving satellite tracking. We carried out some optical and mechanical simulations in order to define the best design for this payload. Final configuration consists of 4 silver coated CCRs made of Suprasil 1

with 33 mm of diameter. DAO is 1.8 $arcsec$ on all of the three retroreflector edges, with a tolerance of ± 0.5 $arcsec$. These values were chosen to not reduce too much the intensity of laser return at COSMO-SkyMed VA. The array structure has an Aluminum pyramidal shape, closed to the back, with one CCR assembled on each side, at 45° inclination relative to the base. The base square is [115 x 115] mm sized, the truncated pyramid height is 50 mm and total weight is about $500g$. This configuration allows to maximize CORA visibility from Laser Ranging stations. CCR's mounting system is inherited from LAGEOS.

Concerning INCA, we carried out a feasibility study to determine the technically and economically more convenient configuration, operationally more simple, reliable and resistant. The aim of this device is the intercalibration of three different positioning techniques: SLR, GNSS and SAR. The final design consists of a $1m$ trihedral radar reflector, made of Aluminum, co-located with an optical CCR of fused silica with $64.4mm$ of diameter and equipped with a GPS/Galileo receiver. The latter is located along the same radar and optical CCR's vertical axis, to guarantee an invariant point, that allows a common systematic error in the intercalibration measurement. The entire device is designed to rotate 360° around the vertical axis and in addition, the radar CCR can rotate around its horizontal axis, to easily point the satellite in azimuth and elevation. A detailed study proves that any instrumentation used for INCA pointing must have an accuracy better than 10°. The total weight is less than $45kg$ and the structure is disassembled and portable.

Chapter 4

SCF-Lab and Testing

The SCF_Lab is an infrastructure built by INFN-LNF in 2011 specifically for the Extra Terrestrial Ranging to Unified Satellite COnstellations (ETRUSCO)-2 ASI-INFN project to enhance testing capabilities of the old facility [21]. The laboratory is located inside a 85 m^2 class 10,000 Clean Room (ISO 7) and it is operational with two facilities: the Satellite/lunar/GNSS laser ranging/altimetry and Cube/microsat Characterization Facility (SCF) and the SCF-G, a facility optimized for GNSS. Each facility consists of:

- Cryostat
- Solar Simulator
- Optical bench
- Vacuum pump system
- Rack mounted control electronics

All of the subsystems for each facility are remotely controlled by two PCs positioned on a control desk. During my activity I used both of them, but CORA payload has been tested inside the SCF. Therefore in the subsection 4.1 I describe in detail the SCF and all of its subsystems.

4.1 SCF_Lab facility and subsystems

The SCF is a unique and unprecedented test facilities built in 2006 at INFN-LNF [18]. The initial goal of the SCF was to perform a complete characterization, in a realistic space environment, of an engineering model of LAGEOS satellite and to perform studies of Fundamental Physics. During the years, its modular and evolutionary design resulted suitable to characterize thermal and laser performances of retroreflectors used on GNSS and EO constellations. The SCF is a cylindrical

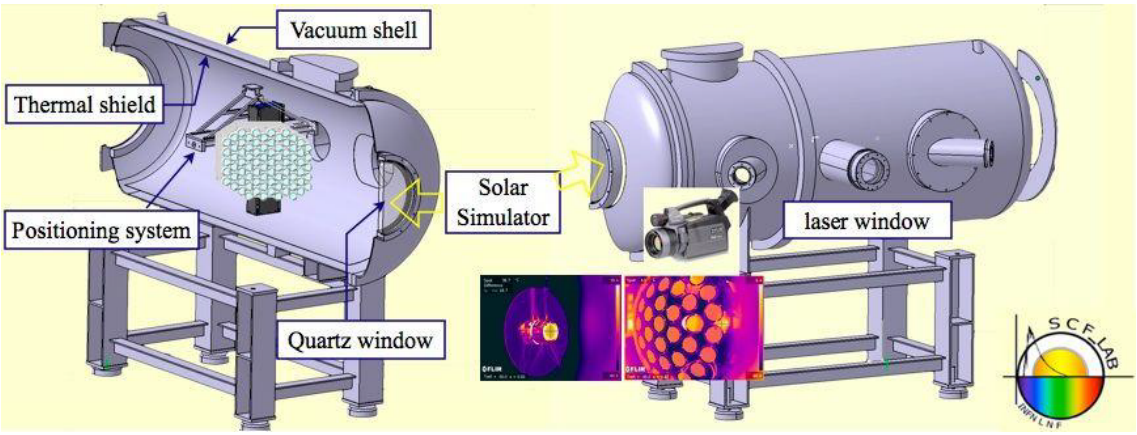

Figure 4.1: Schematic view of the SCF

steel cryostat that has a length of about 2 m and a diameter of about 0.9 m, inside which the space environment is reproduced in terms of pressure and temperature. On the right side of the cryostat there are three circular ports at 45°, 90°, 135° to

its longitudinal axis, respectively available for non-invasive thermal measurements, optical measurements and optional use (see Fig.4.2). The 45° port is equipped with a Germanium (Ge) window, it is used for InfraRed (IR) measurements of the CCRs front face temperature and other parts of the payload. The 90° port is instead equipped with an optical fused-silica window (38 mm thick and optical aperture of 120 mm) with low surface roughness, good optical quality and anti reflective coatings on both sides. It is used for laser interrogation and optical measurements. Through the front quartz window (37 cm clear diameter, 40 mm thickness) a beam created with the Solar Simulator (SS) enters inside the cryostat, heating the payload inside and it is used to study CCR characteristics as explained in section 4.2.

Figure 4.2: SCF facility in the Clean Room with the optical bench

Data acquisition and control System

Data acquisition and control system for the SCF is managed by the system design software LabVIEW by National Instrument. The user interface is simple and at the SCF_Lab we have developed a front panels for each facility's subsystem, dedicated

to data acquisition and instrument control by the user. A compact FielPoint 2220 controller runs LabVIEW Real-Time for data logging, analysis, and process control.

Vacuum/cryogenic System

In order to reproduce the space vacuum inside the chamber we used a two stage pumps system composed by a scroll pump for low vacuum and a cryopump for high vacuum. Scroll pump is used also to make vacuum inside cryopump which needs to reach $5x10^{-2}mbar$ prior to turning it on. When the vacuum inside SCF reaches $5x10^{-4}mbar$, the system is ready for cooling. Cryogenic temperature is reached using a Liquid Nitrogen (LN2) flux. In operative conditions temperature is about 90 K and pressure is about 10^{-6} mbar or better. The cryostat is equipped with an inner cylindrical copper shroud, painted black with Aeroglaze Z306 (0.9 emissivity and low-out gassing) and coated with Multi-Layer Insulation (MLI) sheets to enhance thermal insulation and reduce LN2 consumption.

Temperature Data acquisition System

The temperature data acquisition system consists of two approaches:

- Direct contact temperature monitoring with platinum sensing resistors (PT100)
- Non-invasive temperature measurement via IR camera

At the SCF_Lab we used PT 100 probes for monitoring the temperature of shroud and payload except CCRs, in order to not perturb their optical response. We use two types of PT100: *wirewound* and *flat film*, both four-wire probes that measure the variation of the temperature recording a voltage value at their ends, see Fig.4.3. Wirewound model consists of a pure platinum wire wound up and located within

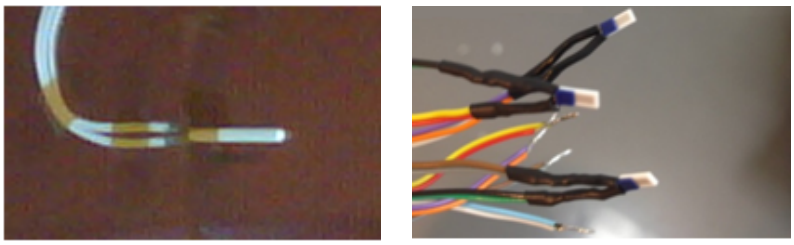

Figure 4.3: Left, wirewound PT100 probe. Right, flat film PT100 probes

axial holes in a high purity alumina rod. It has a good long term stability and a wide operative temperature range, from $-200°$ C to $800°$ C. These probes can work at cryogenic temperatures (below $-50°$ C) with good tolerance. 8 wirewound probes are used to monitor the shroud temperature.
Flat film model is produced by a deposition of a platinum film onto a ceramic substrate (platinum is sealed to ensure protection). These probes have small size with fast response to temperature changes and they are very useful for surface measurement with great resistance to vibrations and shocks. Flat film probes are used to monitor payloads temperature. The temperature of all probes is acquired and displayed on the SCF PC, using data acquisition and control system described above. We work with PT100 probes class A, with a tolerance of $\pm 0.15°$ at test temperature.

Non invasive thermometry is realized by means an IR camera, measuring the infrared radiation coming from the payload inside chamber, that is function of object superficial temperature. The detector measures IR radiation in the range of 7.5 μm and 13 μm and detects temperatures between $-50°C$ and $300°C$. In Fig.4.5 the main features of the IR camera used at the SCF_Lab are summarized. During testing activity the IR camera is positioned on a tripod in front of the SCF Ge window, watching payload inside the chamber. We mainly use this method for the acquisition

Figure 4.4: IR camera SC-640 by FLIR

Imaging performance	Accuracy	± 2.0°C (± 3.6°F) or ± 2% of reading
	Thermal sensitivity	< 0.06°C (< 0.11°F) @ +30°C (+86°F)
	Spatial resolution	▪ 40 mm lens: 0.66 mrad ▪ 19 mm: 1.3 mrad ▪ 76 mm: 0.33 mrad ▪ Close-up lens (P/N: 1196683): 50 µm
	Electronic zoom	Continuous interpolating zooming on images
	Panning	Panning over zoomed-in images
	Digital image enhancement	Adaptive digital noise reduction
Detector	Detector type	Focal Plane Array (FPA), uncooled microbolometer 640 × 480 pixels
	Spectral range	7.5–13 µm
Image presentation	Display	5.6 in., 1000 × 600 pixels
	Viewfinder	800 × 600 pixels
	Frame rate	30/25 Hz (PAL/NTSC)

Figure 4.5: IR camera characteristics

of CCR's temperature, because a temperature probe directly in contact with the reflector would degrade its optical performances. The radiation W_{tot} detected by camera consists of the properly emitted by the object and that deriving from the surrounding environment that the object reflects, as defined in the following formula:

$$W_{tot} = W_{obj} + W_{ref} \tag{4.1}$$

In order to measure accurately the temperature of the object, it is therefore necessary to compensate the effect due to these different radiation sources. Considering radiative thermal exchange possible the only possible in vacuum, we can express the equation 4.1 with:

$$W_{tot} = A_{obj} \cdot \sigma \cdot \epsilon_{obj} \cdot (T_{obj}^4 - T_{env}^4) + A_{obj} \cdot \sigma \cdot (1 - \epsilon_{obj}) \cdot (T_{ref}^4 - T_{env}^4) \tag{4.2}$$

where:

- W_{obj} is the total IR radiation emitted by the object at temperature T_{obj} with emissivity ϵ_{obj}
- W_{ref} is IR radiation emitted by the environment and reflected by the object to the camera. In order to simplify the problem the environment radiation is approximated as a black body radiation with temperature T_{env}
- σ is the Stefan-Boltzmann constant; $\sigma = 5.67 \cdot 10^{-8}$ W/m^2 K^4
- A_{obj} is the object surface, in the approximation that (for the IR camera point of view) the object emissive area is equal to the reflective area.
- T_{env} is the environment (shroud) temperature, 80 K average for the SCF.

From the equation 4.2 the temperature of the object is:

$$T_{obj} = \sqrt[4]{\frac{1}{\epsilon_{obj}} \cdot \left[\frac{W_{tot}}{A_{obj} \cdot \sigma} - (1 - \epsilon_{obj}) \cdot (T_{ref}^4 - T_{env}^4) \right] + T_{env}^4} \tag{4.3}$$

The operation described is done directly by the camera, after setting some object and environment parameters by the user:

- Object Emissivity: thermal radiation emitted from the object with respect to that emitted by a blackbody at the same temperature (0.82 for CCR)

- Reflected Temperature: is defined as the apparent temperature of the objects in the environment, that are reflected by the object under investigation (to be determined)

- Distance: it is used to balance the absorption of the radiation due to the transmittance of the medium between the source and the detector (1 m)

- Relative Humidity: it is set because the transmittance depends also by this parameter (0% being vacuum iside SCF)

- Atmospheric Temperature: atmospheric temperature between the camera and the object (the clean room temperature of 20°)

- External Optics Temperature: temperature of external lens or window (20°)

- External Optics Transmittance: transmittance of external lens or window (0.97 for the Ge window)

All of these parameters are known, except the Reflected Temperature, that is determined following the calibration procedure. This procedure consists of using a PT

100 probe to acquire the temperature of a part of the array at emissivity known. The temperature of this part is evaluated also by the IR camera, changing the reflected temperature among set parameters, to reach the same temperature recorded by the probe.

Solar Simulator

The SS, produced by TS-Space Systems[1], provides a spectrum in the range $(400 - 3000)nm$ and a beam compatible with the solar standard Air Mass 0 (AM0), i.e. outside the atmosphere (solar constant $1367W/m^2$) in terms of intensity, spectrum and uniformity. The solar beam at 35 centimeters diameter surface has a uniformity of $\pm 5\%$. The Fig.4.6 represents in grey the black body spectrum at 5777 K ($area = 1367W/m^2$) and in yellow the extra-terrestrial solar spectral irradiance ($area = 1367W/m^2$). The SS reproduces the yellow trend. The spectrum is built thanks to two lamps inside two parabolic reflectors: a Hydrargyrum Medium-arc Iodide lamp for the UV/VIS and a tungsten incandescent filament lamp (red-IR). The light coming from the two lamps is filtered before being combined by a beam combiner. The intensity of the absolute scale of the SS is established using a thermopile. The thermopile is a black body stable over periods of 5 years, with an accuracy within 5% and it is used in order to correct the power of the SS lamps to compensate aging. The Figure 4.7 shows a lamp, inside SS.

Positioning System

During measurements, payload is alternatively rotated in front of the quartz window (during heating with SS) or the optical window (for the optical measurements) and

[1]http://www.ts-space.co.uk/

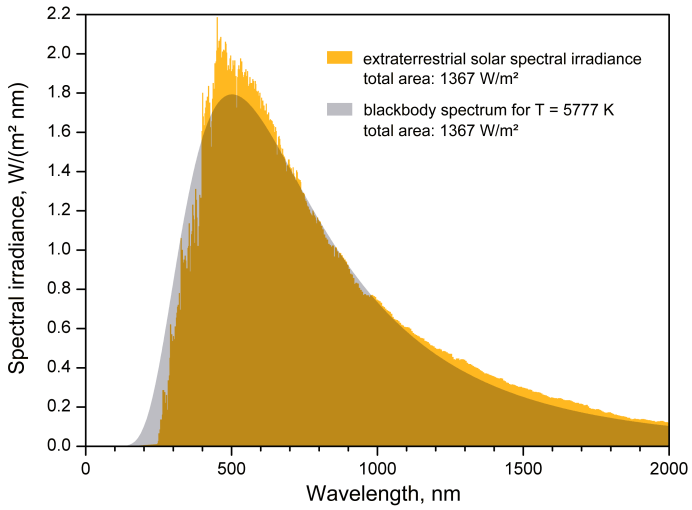

Figure 4.6: Grey: black body spectrum at 5777 K, yellow: extra-terrestrial solar spectral irradiance

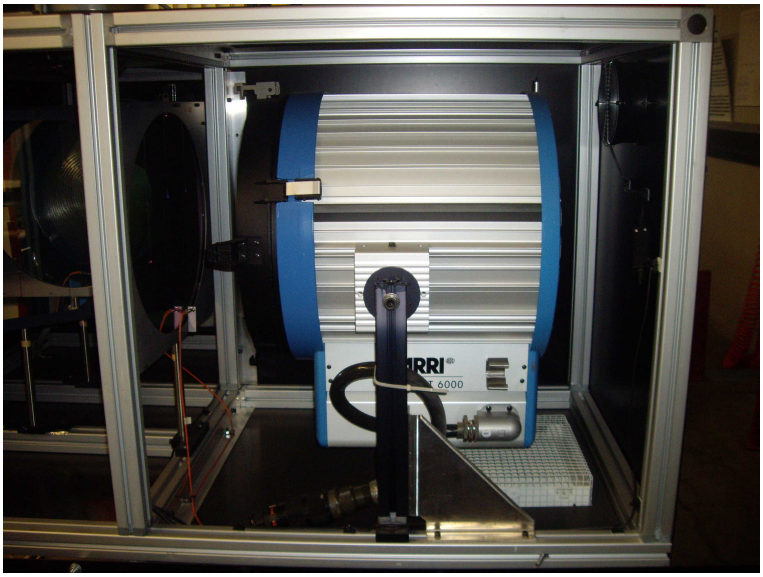

Figure 4.7: Lamp inside SS

it is moved horizontally or vertically, allowing laser beam hitting each CCRs of the array. This is possible thanks to a moving system consists of step by step motors. The payload translation along vertical and horizontal axis (horizontal axis is the cryostat longitudinal axis belonging to the horizontal median plane, while vertical axis is the normal axis to that plane) is made possible by two cryogenic motors, with slide placed inside cryostat. The payload rotation around its vertical axis is instead released by a motor located outside the cryostat. In addition a rotational potentiometer is installed on the external rotation axis, reading the absolute position of vertical axis and therefore of payload inside chamber. All controllers are equipped with limit switches and machine zero for the safe operation of the payload handling within the cryostat. They are controlled using an interface developed in LabVIEW.

Optical Bench

The SCF_Lab optical bench reproduces the laser beam path hitting CCR in orbit and analyzes the beam returning to ILRS ground station, the FFDP [18]. A scheme of the optical table used inside the laboratory for testing activity is shown in Fig.4.8. It consists of the following main components:

- 1 Laser: with a maximum power of 90 mW at the laser wavelength of 532 nm. Laser beam trend during the test is controlled by a power meter.

- 2 Beam Polarizers: one is used to isolate the horizontal component of beam outgoing from laser toward ccr; the other one is used in the laser returning from CCR, to split it into its two components again, since CCR changes the polarization of the beam coming in.

- 1 Beam Splitter: used to bend laser bean towards Charged Coupled Device (CCD)

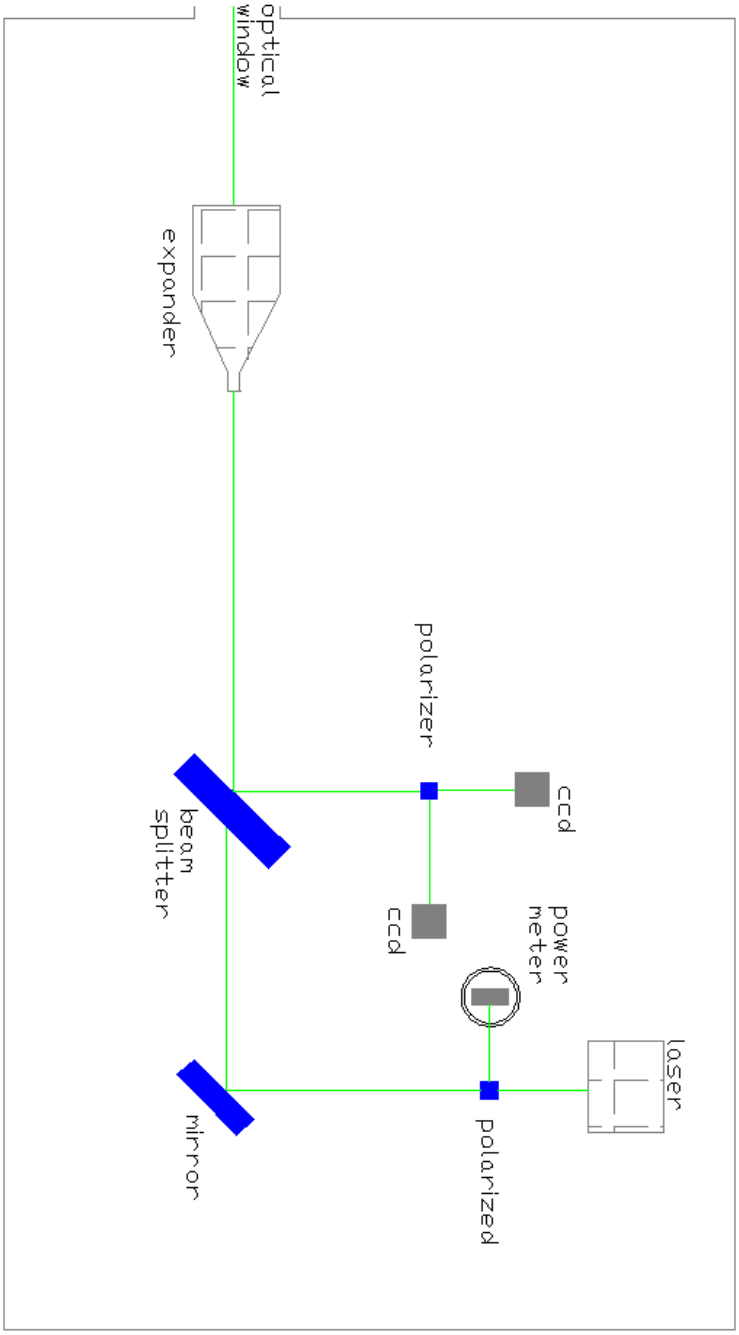

Figure 4.8: SCF FFDP optical circuit

- 1 Beam Expander/Reducer: used to reproduce the round trip of the laser beam from the Earth to the satellite/Moon and back; it expands 20 times the beam (20X).
- CCR/Flat mirror
- 2 CCD + filters: used for the acquisition of two FFDP components separately
- Double slits: used for CCD angular calibration (removable)

4.2 SCF-Test

The SCF-Test consists of a series of concurrent and integrated thermal and optical measurements performed on CCR/LRA breadboards, prototypes or flight payloads. It is an industry-standard procedure developed by INFN to qualify the performance of laser retroreflectors for SLR in accurately laboratory-simulated space conditions (pressure about 10^{-6} mbar, temperature about 90 K, radiation with AM0 spectrum). This test was defined in order to determine those that were identified as Key Performance Indicator (KPI) of retroreflectors: characteristic heating/cooling time of CCR, τ_{ccr}, and FFDP [18].

τ_{ccr} represents the time spent by reflector to reach 2/3 of its plateau temperature, that means the thermal equilibrium with the environment. It is a function of temperature and other environmental conditions experienced by LRA on the spacecraft. The first step to evaluate this parameter is the acquisition of CCR front face average temperature during test by IR picture and camera dedicated software. These raw data are processed by the use of a Matlab code I wrote during my activity, to compute the best fit parameters searching the minimum of χ^2 function on degrees of freedom, where:

- the experimental data are the observed values
- the pure exponential function described in equation 4.4 is the expected function

$$T(t) = T_0 \pm \Delta T(1 - e^{\frac{-t}{\tau_{ccr}}}) \tag{4.4}$$

  - T(t) is the temperature at time t
  - T_0 is the initial temperature
  - ΔT = is the difference between the final temperature and T_0
  - τ_{ccr} is the CCR thermal constant

- χ^2 function is defined with three degrees of freedom: T_0, ΔT and τ_{ccr}.

Matlab code searches τ_{ccr} for minimizing χ^2 function, setting the experimental value as initial value for T_0 and ΔT. The code repeats the computation 250 times with a bootstrap cycle [22] and [23] evaluates the average τ_{ccr} with its standard deviation.

FFDP is the spatial intensity distribution of the laser return at ground from a CCR interrogated by a beam of laser pulses. A distinctive intensity distribution used for CCRs FFDPs characterizing, is the Airy pattern, that is the diffraction pattern resulting from a uniformly illuminated circular aperture made of a flat mirror. It consists of a bright region in the center, called the Airy disc, and a series of concentric rings around it (see Fig.4.9). In Fig.4.10 the experimental Airy pattern, obtained on the SCF_Lab optical bench using a mask with a circular aperture of 38 mm positioned over the flat mirror, is shown: FFDPs are expressed using the OCS [19], that is an intrinsic characteristic of CCRs or LRAs and it is widely used by the SLR community as a measure of the absolute intensity of such payloads. It has the dimensions of an area, expressed in m^2, and can be thought as the size of a

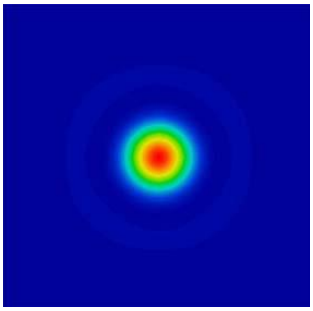

Figure 4.9: Theorical flat mirror FFDP

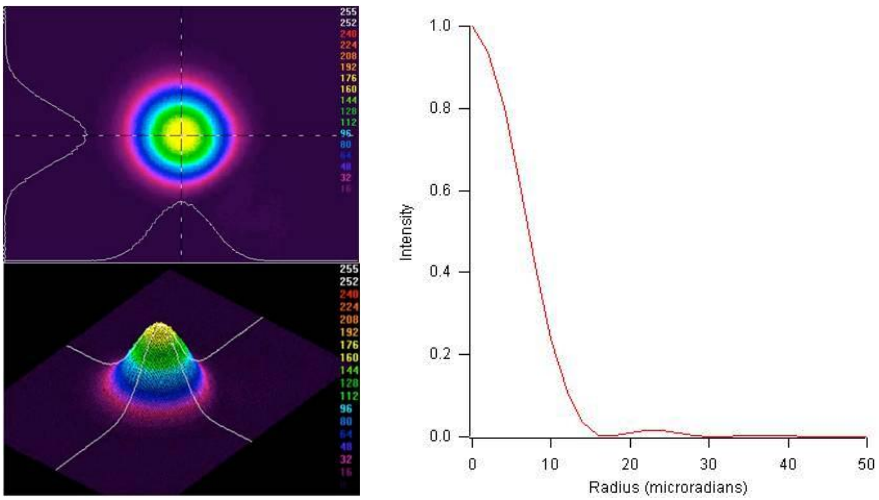

Figure 4.10: (Left) Experimental FFDP of a flat mirror; (Right) Airy pattern trends of the intensity vs radius

diffusely reflecting board in space, that gives the same reflected signal strength as the retroreflector array. Its value at each point of the FFDP is expressed as:

$$\sigma_{ccr} = I_{ccr/mir}(\theta_x, \theta_y) 4\pi (\frac{A_{ccr}}{\lambda})^2 \tag{4.5}$$

where $I_{ccr/mir}$ is the intensity of the FFDP of CCR, at a certain point of the FFDP plane, referred to the intensity of a perfect mirror of the same aperture, at the center; λ is the laser wavelength and A_{ccr} is the area of the CCR.

The SCF-Test consists of two main phases:

- *SUN ON*

- *SUN OFF*

Firstly the payload is mounted inside facility where space simulated conditions are reached, anchored to a support and control plate kept at a fixed temperature T_M ± 0.5. In Earth orbits the default LRA temperature is $T_M = 300\,K$, to guarantee normal operation of equipment. Therefore this is the standard measurement we used for testing. Before starting test is necessary for the CCR to reach thermal equilibrium respect to the environment. After this transition, *SUN ON* phase can start: the LRA under test is illuminated by SS with the beam at 0° respect to the normal to the CCR face. IR pictures of CCRs are recorded, along with the temperature of various components of the LRA. During the following *SUN OFF* phase, SS is turned off and FFDPs with IR pictures and LRA temperature are acquired. The aim is to evaluate the FFDP variation before and after Sun illumination, to quantify how Solar radiation degrades optical performances. During *SUN ON* phase FFDPs are not acquired in order to not perturb the heating phase rotating payload in front of the optical window.
Outputs of those final tests are:

1. CCR FFDPs variation before and after SS illumination (*SUN ON* phase)

2. Average intensity variation of the FFDP at the satellite velocity aberration for each SUN ON-SUN OFF cycle

3. CCR surface temperature and τ_{CCR} in heating and cooling phases

4. Temperature of components of the LRA other than CCRs.

The space environment simulated around CCR and LRA induces thermal gradients inside single CCRs which can cause a variation in the index of refraction and therefore optical performance degradation. Adding to τ_{CCR} the Matlab code extracts from IR picture the maximum temperature gradient on CCR front face. This is the concept of the default SCF-Test that allows us to investigate CCR characteristics. Some customized tests, procedures and experimental setups, not included in the default, have been implemented for a deeper understanding of LRAs performance, such as changing T_M value to evaluate changes in thermal and optical performances and varying SS inclination respect to the CCR front face. In section 5.1.1 I report all SCF-Tests carried out on CORA payload.

4.3 Orbit-Test

With the measurement of a Galileo-IOV array in 2010 at the SCF_Lab, it has been introduced a revision on the standard SCF-Test: the test of thermal and optical conditions experienced by reflectors during a simulated orbit of the satellite, called Orbit-Test. For Galileo satellite INFN developed the Galileo Critical Orbit (GCO). The GCO is the orbit whose angular momentum is orthogonal to Sun-Earth direction. For this particular orbit the inclination vector of Sun rays lays on a plane, and the orientation with respect to the CCR front face changes from $-90°$ to $+90°$. These conditions are reproduced in laboratory by rotating the LRA inside the cryostat, in quasi-real time, for the proper GCO period: ~ 7 hrs for Galileo half orbit, ~ 6 hrs for GPS. A conceptual drawing of this orbit is shown in Fig. 4.11. The first part, *sunrise*, starts from the condition of solar beams parallel to the front face of the CCR and lasts 3 hrs; after this first illuminated part of the orbit, the CCR enters the Earth shadow, modeled for simplicity as a cylinder, which lasts 1 hr;

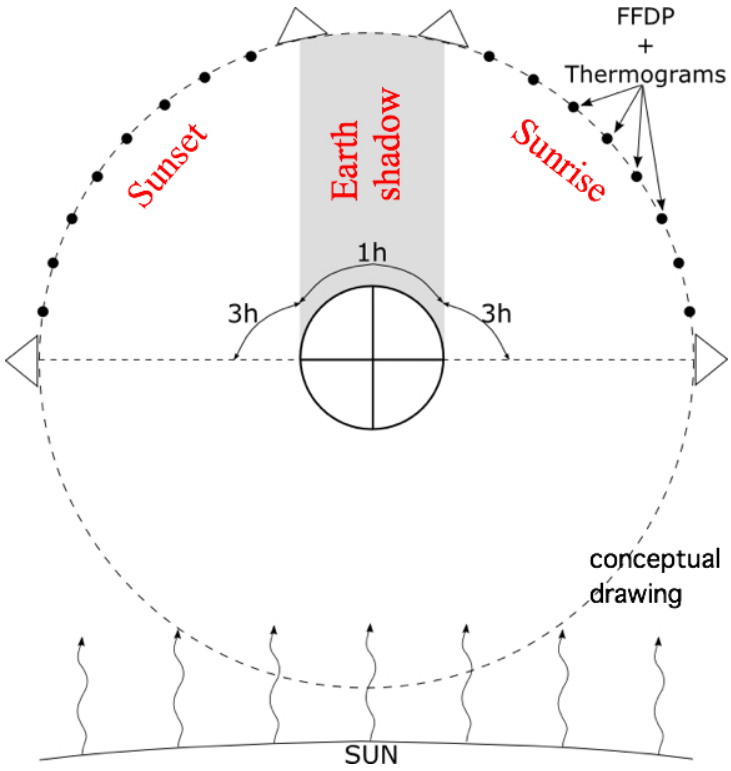

Figure 4.11: Galileo GCO conceptual drawing

the subsequent phase, *sunset*, is specular to sunrise phase, i.e. 3 hrs illumination with the CCR rotating until its front face becomes parallel to solar beams . This test-revision, though adopted specifically for Galileo LRA, is easily extendable to other satellites, even not GNSS. In order to perform a complete characterization of CORA I decided to carry out an Orbit-Test simulating an EO orbit.

4.3.1 EO Orbit simulations

Concerning the Orbit-Test of EO LRA, I simulated a COSMO-SkyMed orbit to know Sun rays inclination on CORA CCR front face during operational life. I developed a Matlab code that integrates the orbit of a COSMO-SkyMed satellite and returns in

output the vector of Sun rays inclination on CCR front face, for any day of the year. The first input given to the program is the choice of the day for orbit integration. This allows to determine the orientation of the satellite orbital plane respect to the Sun. Therefore the anomaly of the Earth, ν_T, in the Heliocentric System[2] is calculated. Afterwards the program integrates the equation of relative motion of satellite around the Earth in the two-bodies problem (equation 4.6), returning in output satellite positions and velocities in the Equatorial Reference Frame[3].

$$\ddot{\mathbf{r}} = -\frac{\mu}{r^2}\hat{\mathbf{r}} \tag{4.6}$$

$\mu = 398600.4405 \pm 0.001 Km^3 s^{-2}$ *Gravitational coefficient.*

Introducing the angles Ω_T (vernal equinox orientation in the Heliocentric System) and α (inclination of the equatorial plane), the change between Equatorial System to Heliocentric System is given by the following rotation matrix [24]:

$$R_{T-Sun} = R_{\Omega_T} R_\alpha \tag{4.7}$$

with

$$R_{\Omega_T} = \begin{bmatrix} cos\Omega_T & sin\Omega_T & 0 \\ -sin\Omega_T & cos\Omega_T & 0 \\ 0 & 0 & 1 \end{bmatrix}; R_\alpha = \begin{bmatrix} 1 & 0 & 0 \\ 0 & cos\alpha & sin\alpha \\ 0 & -sin\alpha & cos\alpha \end{bmatrix}$$

where $\alpha = 23.17°$ and $\Omega_(T) = 102.94°$. In this Heliocentric System, the Sun rays

[2]Xs axis points toward the Earth Perihelium, Zs axis is orthogonal to the Ecliptic and Ys completes the frame

[3]X axis points toward the Vernal Equinox, Z axis points towards the terrestrial north pole and Y completes the frame. This geocentric frame is fixed respect to the fixed stars

direction is given by:

$$s = \begin{bmatrix} cos\nu T \\ sin\nu T \\ 0 \end{bmatrix}$$

Through a transformation of coordinates system, it is possible to describe Sun rays direction in the Equatorial Reference Frame.

$$s_1 = \begin{bmatrix} 1 & 0 & 0 \\ 0 & cos\alpha & -sin\alpha \\ 0 & sin\alpha & cos\alpha \end{bmatrix} \begin{bmatrix} cos\Omega_T & -sin\Omega_T & 0 \\ sin\Omega_T & cos\Omega_T & 0 \\ 0 & 0 & 1 \end{bmatrix} s$$

Next coordinate change leads to the Orbital Satellite System[4], with three successive rotation of the angle that define the orbital plane.

$$s_2 = \begin{bmatrix} cos\omega_s & -sin\omega_s & 0 \\ sin\omega_s & cos\omega_s & 0 \\ 0 & 0 & 1 \end{bmatrix} \begin{bmatrix} cos\Omega_s & -sin\Omega_s & 0 \\ sin\Omega_s & cos\Omega_s & 0 \\ 0 & 0 & 1 \end{bmatrix} \begin{bmatrix} 1 & 0 & 0 \\ 0 & cosi_s & -sini_s \\ 0 & sini_s & cosi_s \end{bmatrix} s_1$$

being ω_s, Ω_s and i_s the orbital parameters *argument of perigee*, *ascension of the ascending node*, *inclination* respectively. Two other rotation matrices are necessary to refer Sun rays to CCR reference system, with z axis nadir pointing and y axis in direction of the orbit angular momentum, as shown in the Fig.4.12. This is the final information used to reproduce Sun radiation on CCR front face during the

[4]x axis points towards periapsis, y is rotated 90° in the direction of orbital motion and lies in the orbital plane, z completes the frame

Orbit-Test.

$$s_3 = \begin{bmatrix} cos(\frac{\pi}{2} - \nu_s) & 0 & sin(\frac{\pi}{2} - \nu_s) \\ 0 & 1 & 0 \\ sin(\frac{\pi}{2} - \nu_s) & 0 & cos(\frac{\pi}{2} - \nu_s) \end{bmatrix} \begin{bmatrix} 1 & 0 & 0 \\ 0 & cos\frac{\pi}{2} & sin\frac{\pi}{2} \\ 0 & -sin\frac{\pi}{2} & cos\frac{\pi}{2} \end{bmatrix} s_2$$

In order to evaluate the satellite visibility from a Laser Ranging Station, I introduced

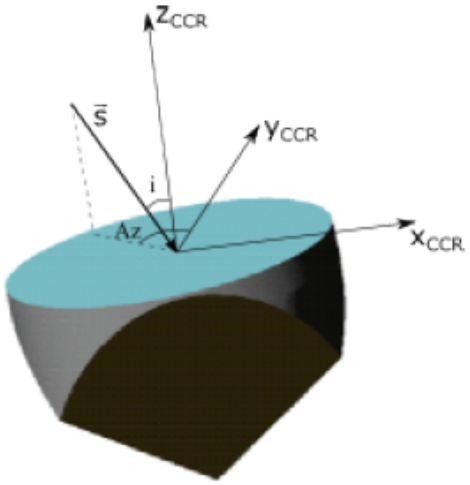

Figure 4.12: CCR coordinate system

a Topocentric Reference System with X axis points south, Y axis points east and Z axis points up normally from the CCR front face [24]. The program asks to the user latitude and longitude of the station and computes the satellite coordinates in this Topocentric System r_{s_t}, using the transformation matrix R_{T-t} from Geocentric-Equatorial System to this Topocentric System:

$$R_{T-t} = \begin{bmatrix} cos\alpha_l sin\delta_l & sin\alpha_l sin\delta_l & -cos\delta_l \\ -sin\alpha_l & cos\alpha_l & 0 \\ cos\alpha_l cos\delta_l & sin\alpha_l cos\delta_l & sin\delta_l \end{bmatrix}$$

$\delta_l = declination$ and $\alpha_l = rightascension$ of the station.

Orbital simulation results are reported in this section and this trend has been reproduced inside chamber using SS and facility's movement system. As explained in Chapter 2 COSMO-SkyMed orbit is a dawn-dusk sun-synchronous orbit, with a period of $\sim$ 1.6 hours, inclination of 97.86° and altitude of $\sim$ 619 km. In this type of orbit, the satellite orbital plane remains approximately fixed with respect to the Sun and therefore satellite passes over a chosen area, in this case the Italian Laser Ranging Station (ASI-Centro di Geodesia Spaziale "G. Colombo" in Matera at the same time for all orbits of any day and in particular at about 6 am (with maximum elevation) and 6 pm (with minimum elevation) local time, as shown in the Fig.4.13. Fig.4.14 shows Sun rays inclination on CORA tested CCR during orbits at 26/03/15.

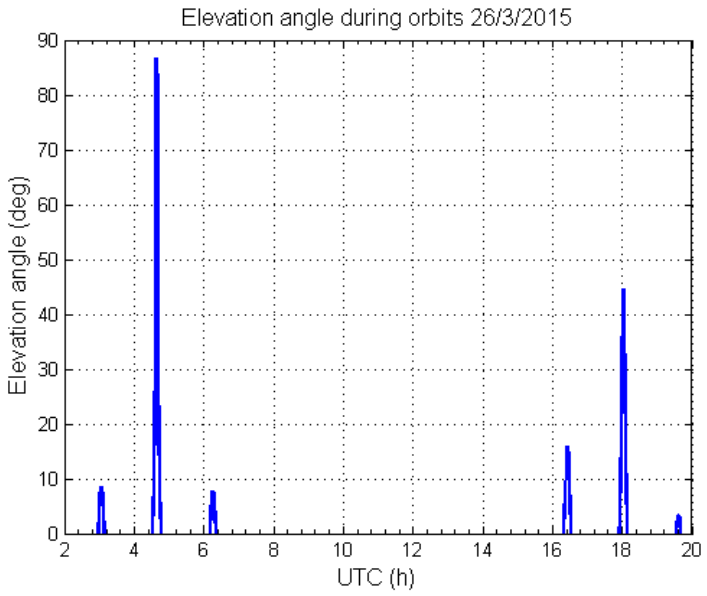

Figure 4.13: Cosmo-SkyMed visibility from Matera Laser Ranging Station at 26/03/15

In section 5.2 I describe in detail CORA Orbit-Test performed in order to inves-

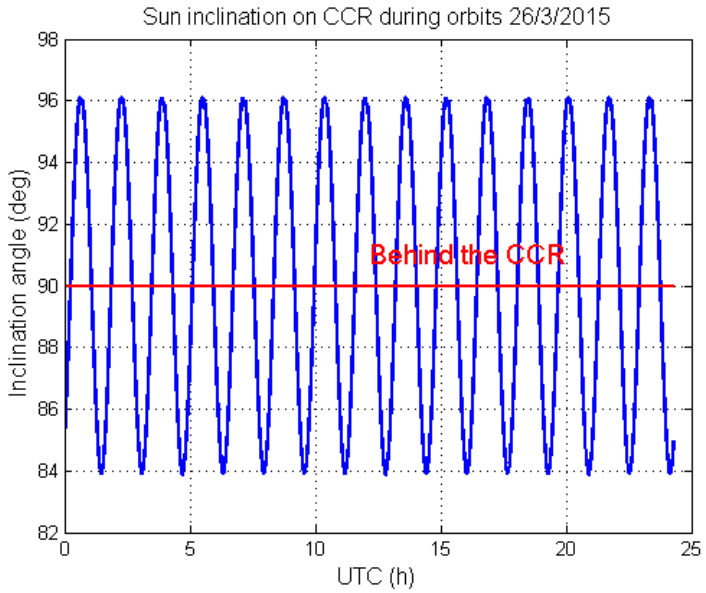

Figure 4.14: Sun rays inclination on CCR front face during orbits at 26/03/15

tigate its realistic behavior during operational live, reproducing conditions shown in this simulation.

Chapter 5

CORA Characterization and Results

In this Chapter I describe experimental tests performed to characterize CORA payload, composed by the standard SCF-Test and the Orbit-Test. In section 5.1 I provide a description of SCF-Test setup, while thermal and optical results are reported in section 5.1.1. Section 5.2 regards the Orbit-test setup and section 5.2.1 concerns on its relative results. Finally in section 5.3 I report the main testing results concerning to other GNSS LRA (that I analyzed during my PhD activity), in order to provide a useful comparison for well understanding CORA performances.

5.1 CORA SCF-Test characterization

In this section I present tests carried out to investigate CORA engineering properties in a space simulated environment. We performed three SCF-Tests, at different temperatures of the support and thermal control plate: 280 K, 300 K, 320 K. As

mentioned before, we need a support plate to anchor payload to the movement system inside the facility and also to control its structure at a fixed temperature. In this way we can study the only thermal/optical CCR behavior, avoiding any influences from the housing, due to its temperature variation during testing. We consider the SCF-Test at 300 K as our reference, since satellite structure temperature is controlled at about 300 K, to guarantee normal operation of equipment. For this reason we decided to test CORA first with the plate fixed at 300 K; after that, we wanted to investigate its behavior changing the reference temperature of ± 20 K, to evaluate potential variation of CCRs thermal relaxation time. In fact from the theory [28], an increase in the housing temperature must decrease the time constant, and any divergences from this law could suggest a non optimal thermal isolation between CCR and its structure.
In order to control the structure at the chosen temperature, we used three circuits of 4-wires resistive tape heaters installed on the support and control plate and some PT 100 probes for thermal monitoring during testing. Fig.5.1 shows CORA plate with heaters installed, while PT 100 probe [1] locations are shown in the Fig.5.2. Table 5.1 summarizes probes name and position. In order to ease the identification of CORA CCRs for test, those were tagged in the Fig.5.3 with their serial number. We optically tested CCR number 13. IR Calibration probe was used to remove the background noise from thermal measurement at the beginning of the analysis, as described in section 4.1 and Plate back probe was used for heaters control and for temperature monitoring of the structure during testing.

Following the procedure described in section 4.2, inside the facility vacuum was pulled down to $10^{-6} mbar$ and shields were cooled at the average temperature of

[1] for reference about the PT100 standard calibration curve see:
http://http://gilsoneng.com/reference/rtdinfo.pdf

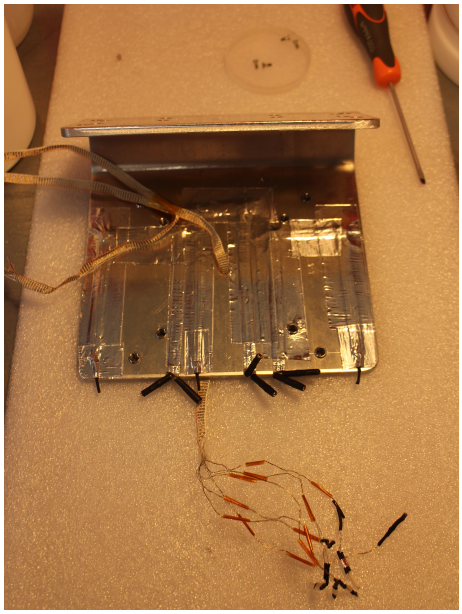

Figure 5.1: CORA support and control Aluminum plate with heaters installed

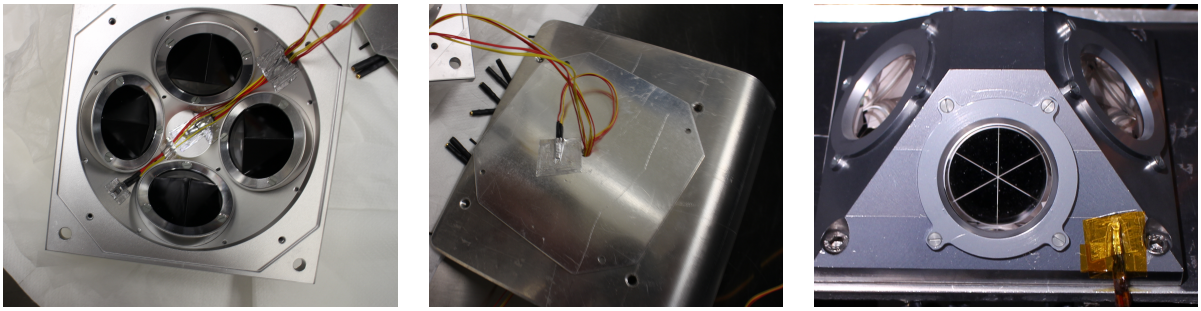

Figure 5.2: Different views of CORA with probes. From left: probes inside the frame structure, probe on cover back plate and probe for infrared calibration.

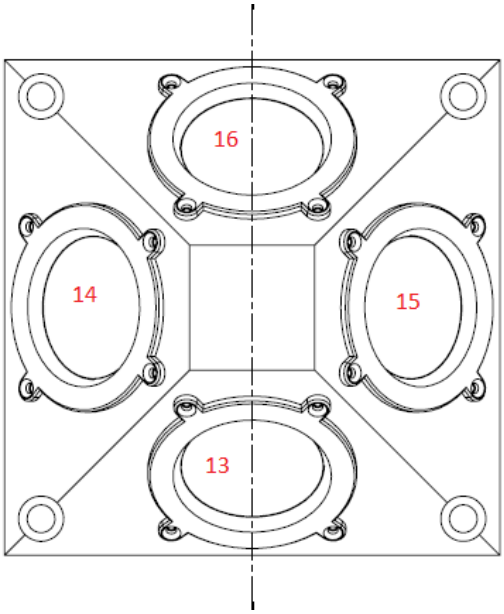

Figure 5.3: CORA drawing with CCRs serial numbers

Probes name	Probes position
Frame top	Inside, on the top part of the truncated pyramid
Frame bottom	Inside, on the frame between the CCR number 13 and 14
IR calibration	On the front side of the array, on the right of CCR number 13
Plate back	Inside, on the back plate of the array

Table 5.1: CORA probes name and position

about 90 K. After an initial conditioning phase, in which CCRs were facing to the optical window to reach thermal equilibrium, the SCF-Test started. Test phases and operations performed can be summarized in a *SUN ON* heating phase (3hrs long, with the only acquisition ofIR pictures) and a *SUN OFF* cooling phase (3hrs long , with acquisition of both FFDPs and IR pictures). FFDPs were acquired only during *SUN OFF* in order to not perturb the thermal heating on the assembly. In fact in order to acquire FFDP the entire structure must be rotated in front of the optical window, closing the SS shutter. This procedure would affect SUN ON

heating phase creating a non-homogeneous conditions, canceling the reliability of test. The acquisition of FFDPs during the *SUN OFF* is:

- every minute for 20 minutes
- every 2 minutes for 40 minutes
- every 4 minutes for 60 minutes
- every 10 minutes until the end of the test.

It is important to underline that one FFDP is acquired in undisturbed conditions before starting of *SUN ON* phase and it is used as reference to evaluate potential variations occurred after heating. IR images were acquired every minute for the entire test.

5.1.1 CORA SCF-Test Results

As mentioned before, we carried out three SCF-Tests at different temperatures of CORA housing (280K, 300K, 320K) and in this subsection I report thermal and optical results for all of them.

Thermal Results

The IR analysis is achieved with FLIR Thermacam Researcher software and a specific Matlab code, as described in section 4.1. In Fig.5.4 one CORA IR picture is shown, acquired during the test. In the following part I report the main plots with τ_{ccr}, χ^2_{FIT} and ΔT analysis.

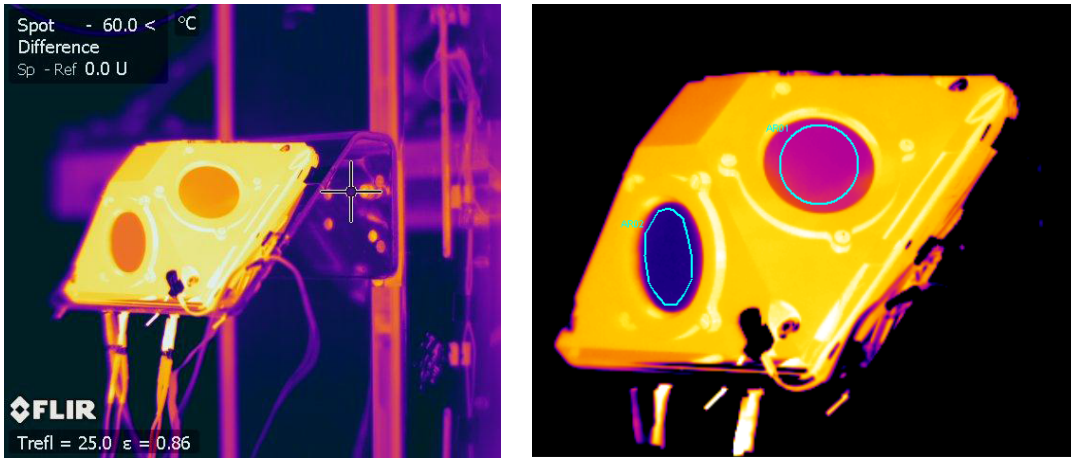

Figure 5.4: Left, IR CORA image. Right, example of CORA IR image with areas selected for thermal analysis

CORA SCF-TEST 280K: Thermal results

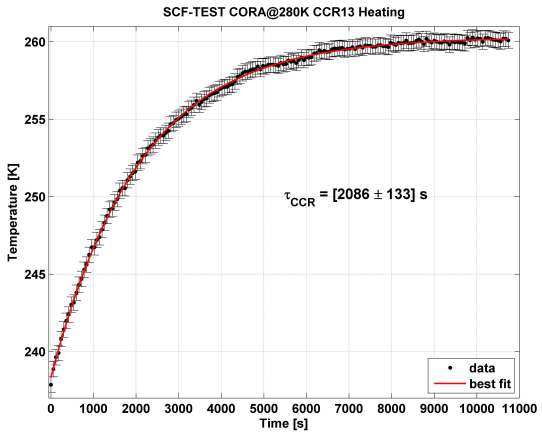

(a) τ_{ccr} *heating phase,* $\chi^2_{FIT} = 0.06$.

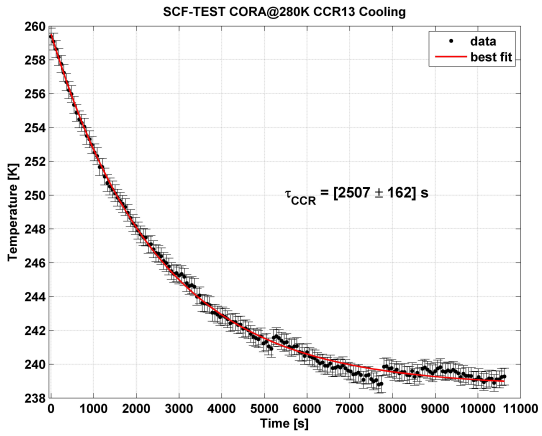

(b) τ_{ccr} *cooling phase,* $\chi^2_{FIT} = 0.29$.

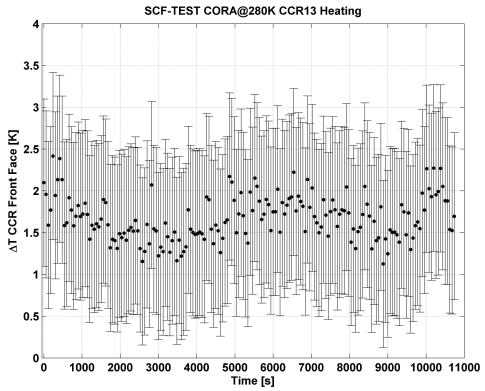

(c) *Front face gradient heating phase.*

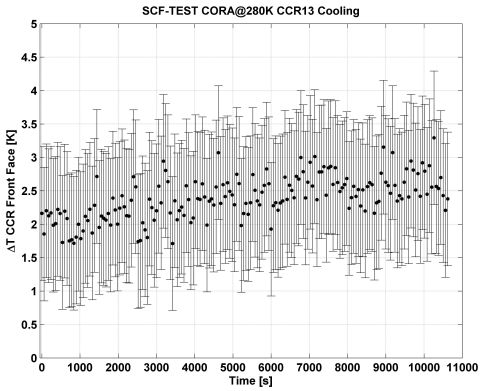

(d) *Front face gradient cooling phase.*

Figure 5.5: CORA-2 SCF-Test at 280K, IR analysis result.

CORA SCF-TEST 300K: Thermal results

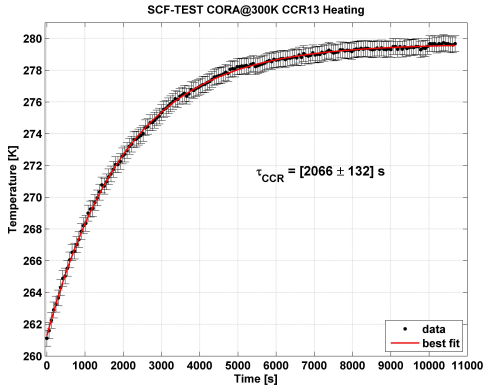

(a) *τ_{ccr} heating phase,* $\chi^2_{FIT} = 0.06$.

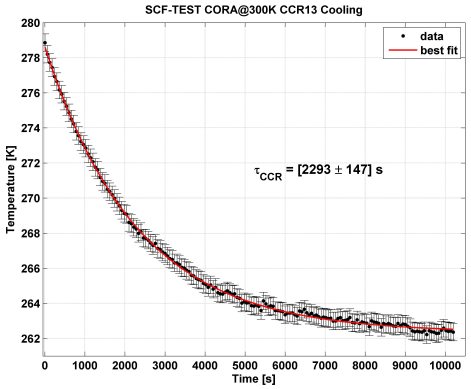

(b) *τ_{ccr} cooling phase,* $\chi^2_{FIT} = 0.29$.

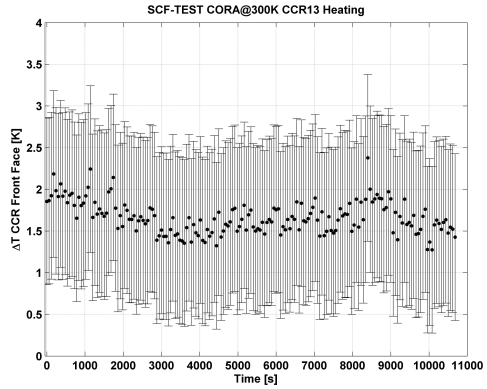

(c) *Front face gradient heating phase.*

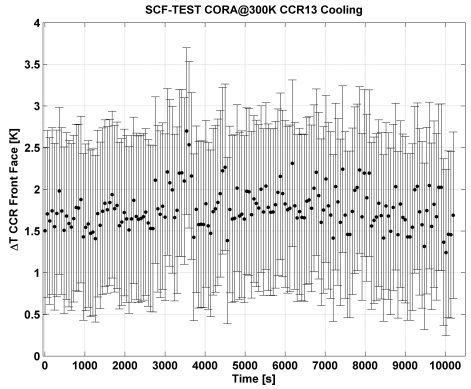

(d) *Front face gradient cooling phase.*

Figure 5.6: CORA-2 SCF-Test at 300K, IR analysis result.

CORA SCF-TEST 320K: Thermal results

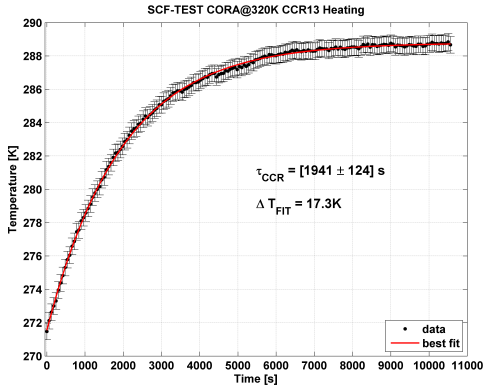

(a) τ_{ccr} *heating phase,* $\chi^2_{FIT} = 0.04$.

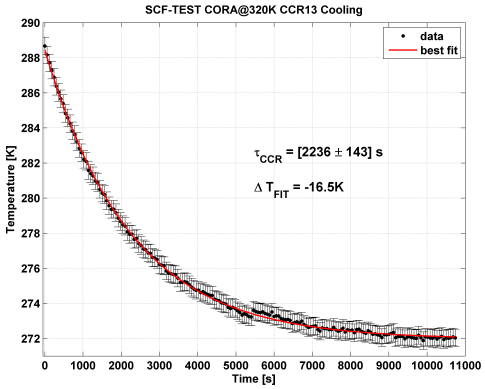

(b) τ_{ccr} *cooling phase,* $\chi^2_{FIT} = 0.06$.

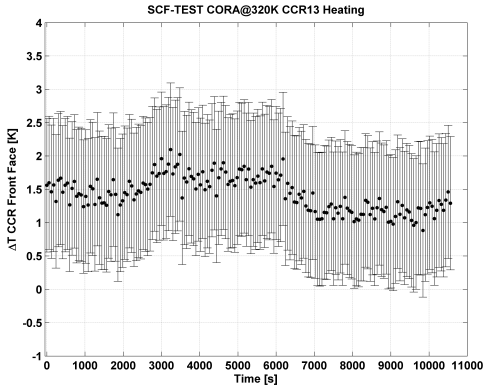

(c) *Front face gradient heating phase.*

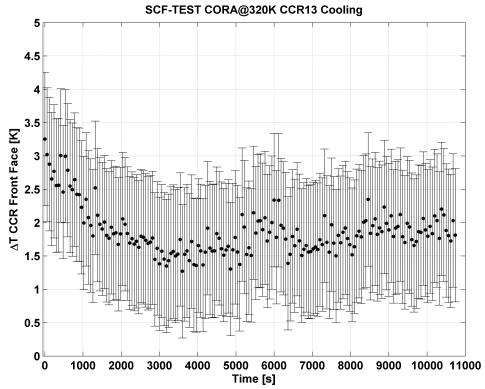

(d) *Front face gradient cooling phase.*

Figure 5.7: CORA-2 SCF-Test at 320K, IR analysis result.

Following tables summarize results of all three SCF-Tests.

Test	$\tau_{ccr} heating$ **(s)**	$\tau_{ccr} cooling$ **(s)**	$\tau_{ccr} average$ **(s)**
SCF-Test 280 K	2086±133	2507±162	2317±298
SCF-Test 300 K	2066±132	2293±147	2185±161
SCF-Test 320 K	1941±124	2236±143	2099±189

Table 5.2: Summary of SCF_Test thermal results: τ_{ccr} during heating phase, τ_{ccr} during cooling phase and τ_{ccr} average

Test	**Temperature average gradient (K)**
SCF-Test 280 K	2.0±0.5
SCF-Test 300 K	1.7±0.2
SCF-Test 320 K	1.6±0.5

Table 5.3: Summary of SCF_Test thermal results: Temperature average gradient on CCR front face

Test	**ΔT heating (K)**	**ΔT cooling (K)**
SCF-Test 280 K	22.0±1.0	-20.8±1.0
SCF-Test 300 K	18.4±1.0	-19.3±1.0
SCF-Test 320 K	17.3±1.0	-16.5±1.0

Table 5.4: Summary of SCF_Test thermal results: Maximum ΔT during heating and cooling phase

Temperature data in these plots have a statistic error of ±0.5 K, introduced by the IR camera. CORA thermal analysis shows the average τ_{ccr} is about 2000 seconds for all tests. This behavior is in accordance with other reflectors of the same volume tested at the SCF_Lab and indicates a good thermal insulation between CCR and its housing and an optimized mounting system. Generally during heating phase, thermal charging is faster than thermal discharging (cooling phase), therefore

heating τ_{ccr} is lower than cooling τ_{ccr}. Average τ_{ccr} decreases slightly with the increase of Aluminum plate temperature, as shown in the Table 5.4, following the expression $\tau_1/\tau_2 \propto T_2/T_1$. This is in accordance with CCRs of LAGEOS satellite, previous tested at the SCF_Lab, as reported on ILRS web site[2]. These good results are confirmed also by low temperature gradient on CCR front face, that is stable and about 2 K or less for all tests. There are not hot spots visible near screws in the IR images. This reduced heat exchange between reflector and its housing leads to good optical performances, as shown in the next subsection.

[2]https://ilrs.cddis.eosdis.nasa.gov/technology/spaceSegment/

Optical results

Concerning the optical data, as mentioned in section 4.2, we measure simulated laser return intensity distribution on the ground, for CCR under testing; then through the optical analysis and a Matlab code developed at the SCF_Lab, we compute the following deliverables:

- FFDP in OCS unit
- OCS intensity distribution versus velocity aberration
- OCS intensity distribution in annulus at operational VA.
- Average OCS intensity at VA of FFDPs for entire test.

As explained before, this array was designed for LEO satellites and then VA is over the range 25-50 μrad. Therefore we computed the average OCS intensity, taking into account all values inside an annulus at this specific VA range. The azimuth angle equal to zero is on a horizontal line of FFDPs, on the right, and counted positive counterclockwise. The maximum error for all OCSs presented in this document is 15% and it is a measure of the systematic error introduced by all optical components used during test. In Figures 5.8, 5.9 and 5.10 the results of optical analyses are reported, as comparison with thermal results, for a deeper understanding of CORA thermal properties.

SCF-TEST 280K

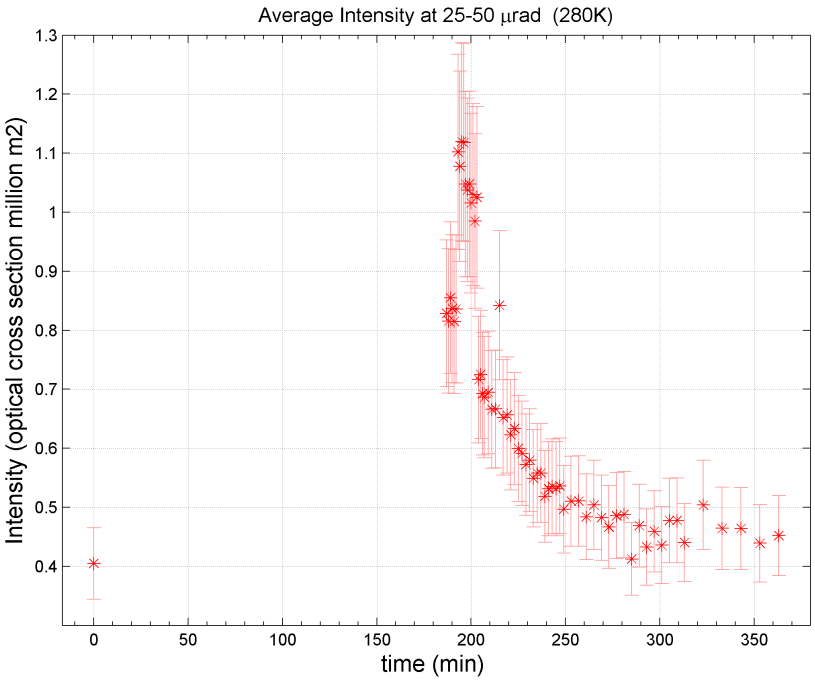

(a) Average intensity vs time at range 25-50 μrad during the SCF-Test.

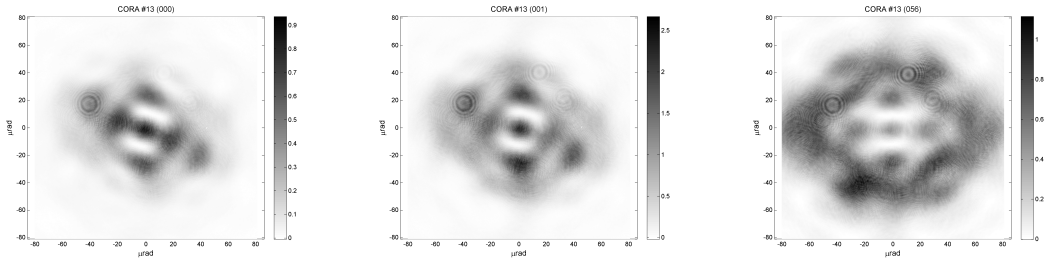

(b) *First FFDP, beginning of test.* **(c)** *Second FFDP, beginning of SUN OFF.* **(d)** *Last FFDP, end of test.*

Figure 5.8: CORA SCF-Test at 280K.

SCF-TEST 300K

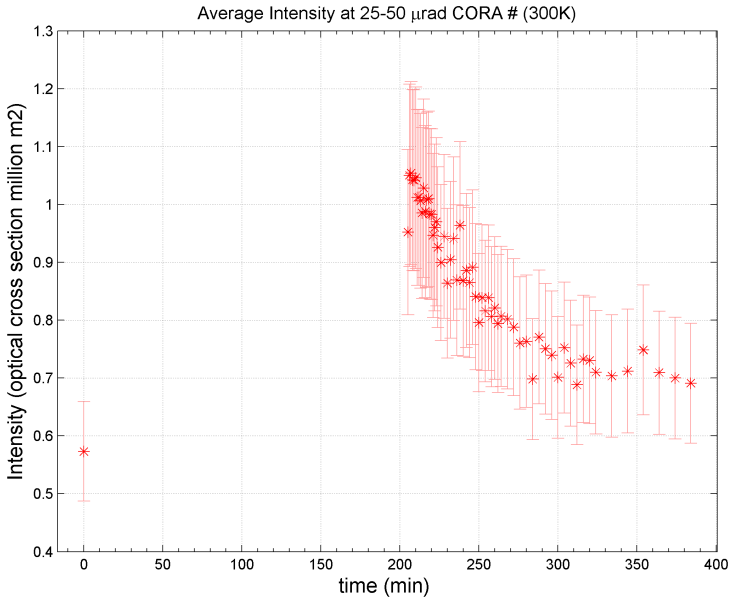

(a) Average intensity vs time at range 25-50 μrad during the SCF-Test.

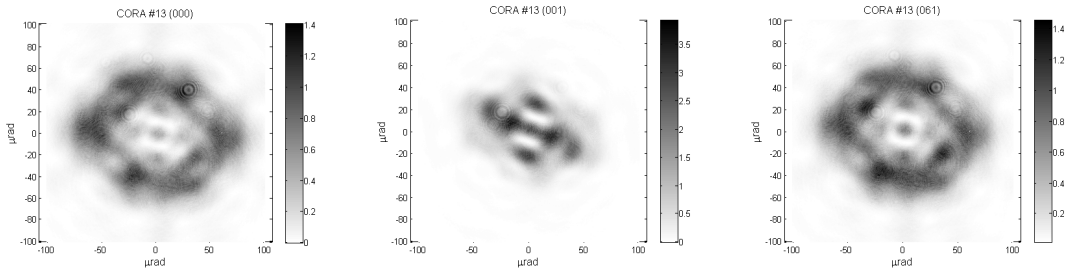

(b) *First FFDP, beginning of test.* **(c)** *Second FFDP, beginning of SUN OFF.* **(d)** *Last FFDP, end of test.*

Figure 5.9: CORA SCF-Test at 300K.

SCF-TEST 320K

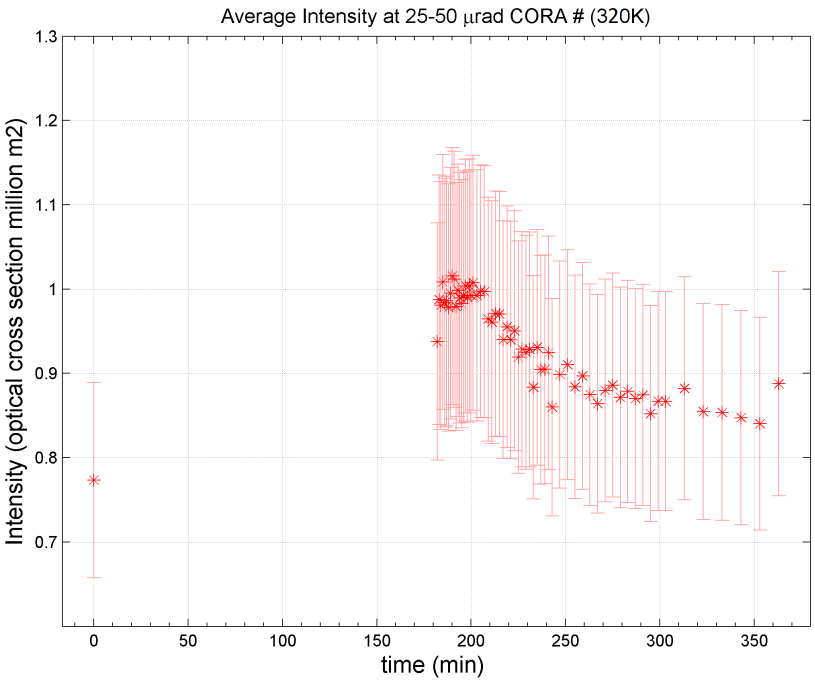

(a) Average intensity vs time at range 25-50 μrad during the SCF-Test.

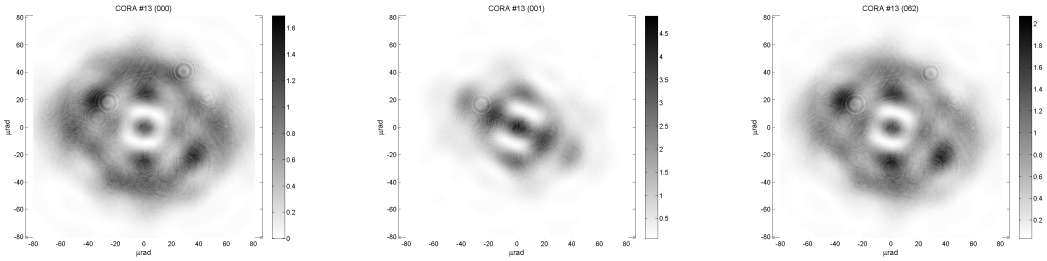

(b) *First FFDP, beginning of test.* **(c)** *Second FFDP, beginning of SUN OFF.* **(d)** *Last FFDP, end of test.*

Figure 5.10: CORA SCF-Test at 320K.

CORA optical analysis shows how pattern's shape and intensity at the end of all tests, come back to the conditions before starting test. It means the variation due to Sun heating, disappears during cooling phase and CCR comes back to work as in

undisturbed conditions. This behaviour is also clear in particular in Fig.5.10a where the average intensity variation in the range of VA, during the SCF-Test at 300 K is plotted. This intensity starts from about 0.6 million m^2 in undisturbed conditions and after a transient phase at the beginning of *SUN OFF*, it comes back to 0.6 million m^2 at the end of test. Good thermal results and low temperature gradients on CCR front face are demonstrated also by these optical results and indicate an optimized design.

5.2 CORA Orbit-Test Characterization

Concerning the Orbit-Test, I needed to simulate Cosmo Sky-Med orbit to know Sun rays inclination on CORA CCR front face during operational life and reproduce this profile inside the chamber, using facility's movement system. This orbital simulation has been describe in detail in section 4.3.1.

In order to reproduce in laboratory this behavior, I divided the orbit in two parts of 50 minutes each one. The first phase (illumination) starts with SS turned on and CORA in front of the laser window, therefore Sun rays are parallel to CCR number 13 front face. During this phase I rotated CORA of 1.2° every 5 minutes, increasing Sun rays inclination on CCR front face up to +6° and turning back to the parallel condition. During the second phase (shadow) I turned off SS to reproduce the shadow, that means Sun rays to the rear of CCR.

We performed three consecutive orbits. I report results of the only third orbit that is the most realistic, representing CORA behavior free of transients. In fact, even if payload is controlled at around 300 K during preparation phases, when the test starts it is left thermally floated; therefore when the third orbit begins, after about 12000 seconds, considering CORA τ_{ccr}, we can conclude that payload reached its

realistic thermal conditions.

During this test we acquired:

- one IR and one FFDP every rotation (5 minutes) for the whole Sun illumination phase

- one IR every one minute and one FFDP every one minute for first 10 minutes, one FFDP every 2 minutes for other 10 minutes and one FFDP every 10 minutes up to the end of test, during shadow phase.

However CORA is intended to be installed on LEO satellites and for this reason it will be affected by the IR radiation, coming from the Earth albedo. For a Cosmo-SkyMed satellite orbit, the typical albedo is of 0.2, [25], so CORA during its orbit experiences a total radiation 1.2 times the solar constant. In order to reproduce the albedo thermal effect and obtain a radiation with an intensity of $1.6kW/m^2$, I modify the focus of SS, increasing the intensity at the beam center. Before changing focus, I measured with a pyranometer an intensity of $1.35kW/m^2$, and after modification I measured $1.60kW/m^2$, with a beam uniformity inside CORA dimensions of $\sim 3\%$.

Fig.5.11 shows CORA inside the SCF, during Orbit-Test. We used 10 layer Mylar sheets to isolate CORA from its support plate, therefore the payload is floating and its temperature is not fixed like during SCF-Test, to study its real thermal behavior during operational life, as explained before. For temperature monitoring we used the same probes described for the SCF-Test in 5.1 and as already mentioned space simulated conditions inside SCF are: pressure about $10^{-6}mbar$ and shields at about 90 K.

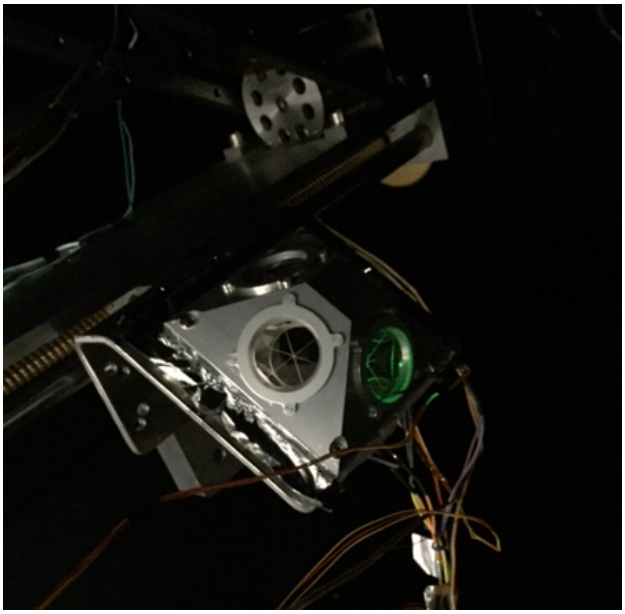

Figure 5.11: CORA inside SCF ready for Orbit-Test

5.2.1 CORA Orbit-Test Results

In this section I report the main thermal and optical results of the third orbit performed.

Thermal Results

Fig.5.12 shows temperature trend of PT 100 probes installed on CORA and on its mounting plate. The temperature of all probes increase during illumination phase and decrease quickly during shadow. All probes become to decrease about some minutes before starting shadow phase, due to Sun rays inclination on payload. I did not acquire any IR picture because during this test the payload (CCRs and chassis) reached temperatures below IR camera limit of acquisition (223.15 K). Looking at the results a large increase in the temperature is show for the green probe, located

inside CORA back plate. For the other probes, this increase in reduced and the thermal behaviour (in terms of absolute temperature and trend) is quite similar.

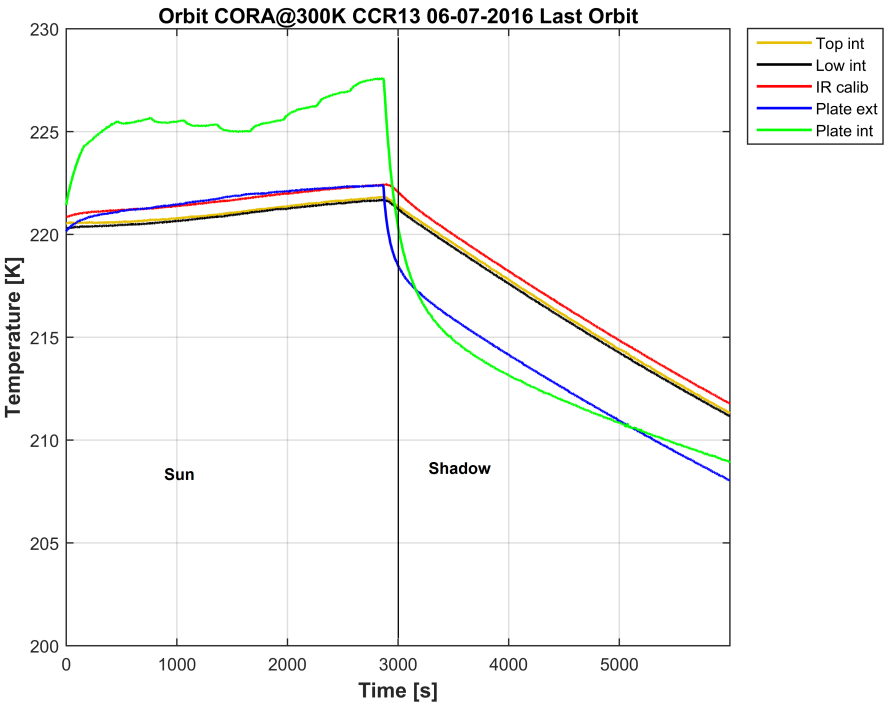

Figure 5.12: CORA probes

Optical Results

The most important result for CORA Orbit-Test is the optical behavior, that shows good performances along whole orbit. I report FFDPs, intensity versus velocity aberration and intensity versus azimuth angle in the range of 25-50 μrad VA, before Sun illumination phase, during the shadow phase and at the end of test. These results highlight small changes in FFDP shape and low decrease of intensity due to Sun heating. The average intensity at 25-50 μrad (Fig.5.19) starts from

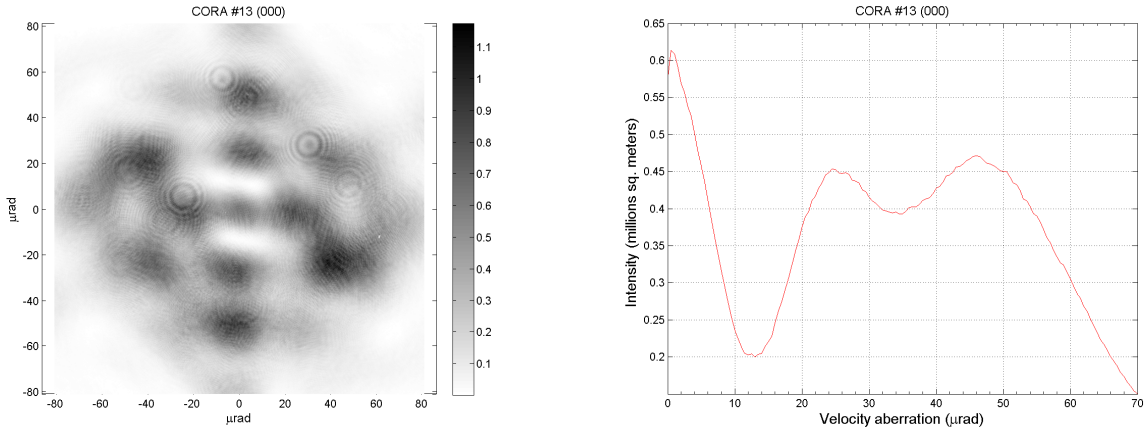

Figure 5.13: Left: FFDP; Right: average intensity versus velocity aberration of CCR num.13 before Sun illumination, during Orbit-Test

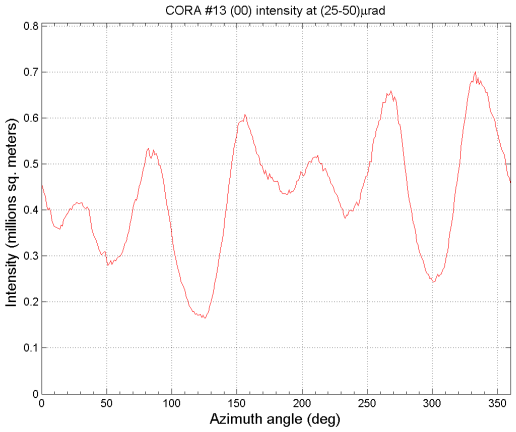

Figure 5.14: Intensity at the VA of operations (25-50 µrad) of CCR num.13 before Sun illumination, during Orbit-Test

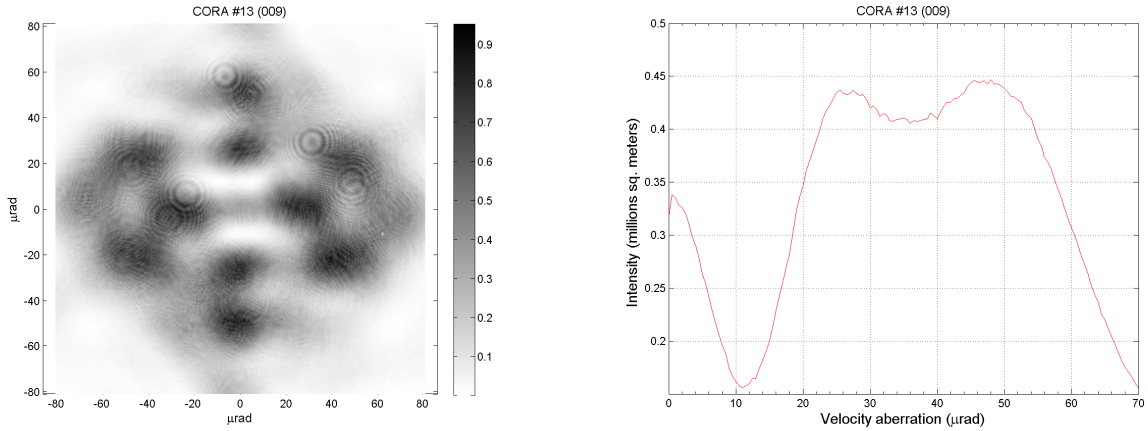

Figure 5.15: Left: FFDP; Right: average intensity versus velocity aberration of CCR num.13 after Sun illumination, during Orbit-Test

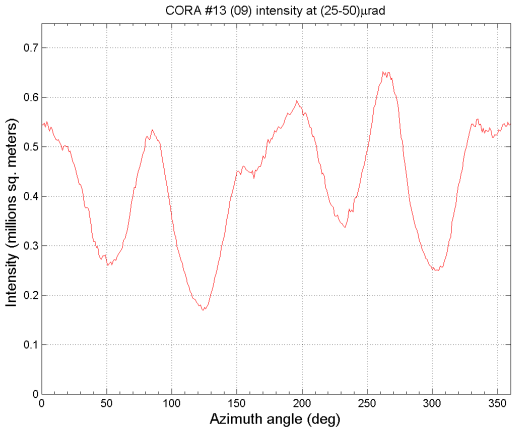

Figure 5.16: Intensity at the VA of operations (25-50 µrad) of CCR num.13 after Sun illumination, during Orbit-Test.

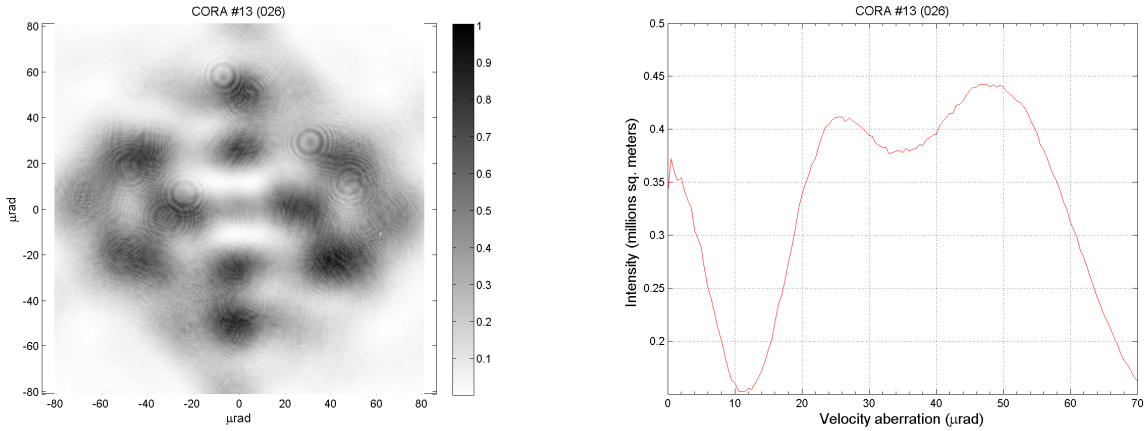

Figure 5.17: Left: FFDP; Right: average intensity versus velocity aberration of CCR num.13 at the end of test, during Orbit-Test

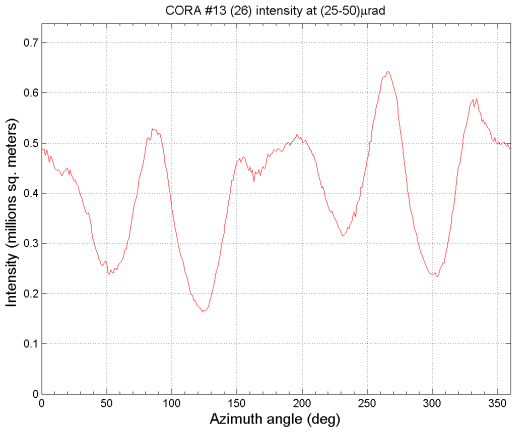

Figure 5.18: Intensity at the VA of operations (25-50 µrad) of CCR num.13 at the end of test, during Orbit-Test

0.45 million m^2 before Sun illumination and decreases during heating phase up to 0.28 million m^2; then it increases up to about 0.4 millions m^2 during shadow phase. These values are consistent with the same plot of CORA SCF-Test at 300 K and indicate a good optical behavior in realistic operative conditions, affected by a low degradation due to heating.

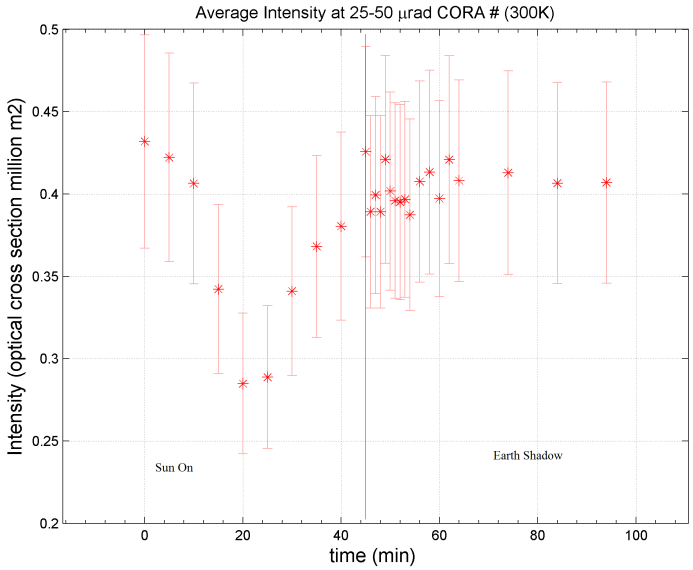

Figure 5.19: Average intensity variation in the VA range, during Orbit-Test

5.3 Correlation with Galileo and GNSS

In this section I report some characterization tests of LRAs for GNSS satellites I performed during my research activity, to investigate their thermal and optical performances and to deeply study the correlation between structural design and optical behavior. A well understood (that means a well characterized) performance of GNSS and of EO LRAs, is the basis to characterize the co-location of GNSS

positioning with SLR in the space segment. Moreover I can compare these results with CORA thermal and optical analysis to deeper understand its characterization. LRAs here reported are: an array deployed on European Galileo In Orbit Validation satellites (section 5.3.1), an array of the IndianIRNSS (section 5.3.2) and a GNSS Retroreflector Array (GRA), developed by INFN and ASI during the ETRUSCO-2 project ([21]) (section 5.3.3).

5.3.1 Results of SCF-Test of Galileo IOV

In this subsection are reported the main testing results carried out on the Engineering Model (EM) of Galileo-IOV, on behalf of ESA [26]. The array is shown in Fig. 5.20. It is composed by 7 solid coated 33 mm diameter CCRs, assembled on an Aluminum base plate in a hexagonal axial symmetric configuration. The base plate is provided with a Thermal Control System consisting of heaters, radiators and PT 100 probes, to allow its temperature control during tests.

EM LRA was installed inside SCF on the 3-axis movement system and Fig. 5.21 shows the payload inside facility, ready for testing. We carried out the standard SCF-Test at three different temperatures of the base plate (233 K, 273 K, 318 K) and a Galileo Orbit-Test to simulate a GCO, following the procedures described in section 4.2. For every SCF-Test Sun On and Sun Off phases were each 5 hours long and we acquired one IR every 30 seconds for both of them. The Table 5.5 summarizes the main thermal results of testing campaign.

These thermal relaxation times indicate a low insulation between metal housing and CCR and therefore a non optimized mounting system. During thermal analysis I also observed three hot spots on CCR front face, close to mounting screws, as shown in the IR picture in Fig. 5.22. Tables 5.6 and 5.7 reports temperature gradients on

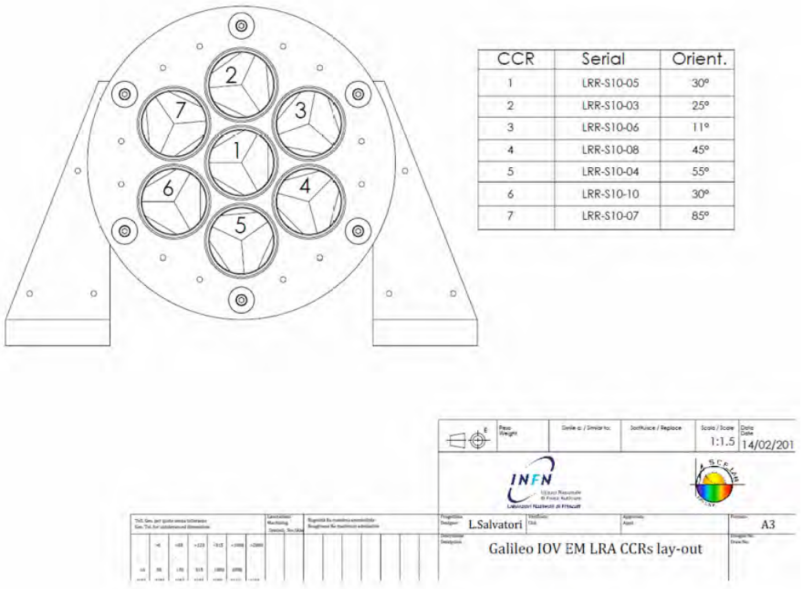

Figure 5.20: Drawing of Galileo-IOV Engineering Model with CCRs number and orientation

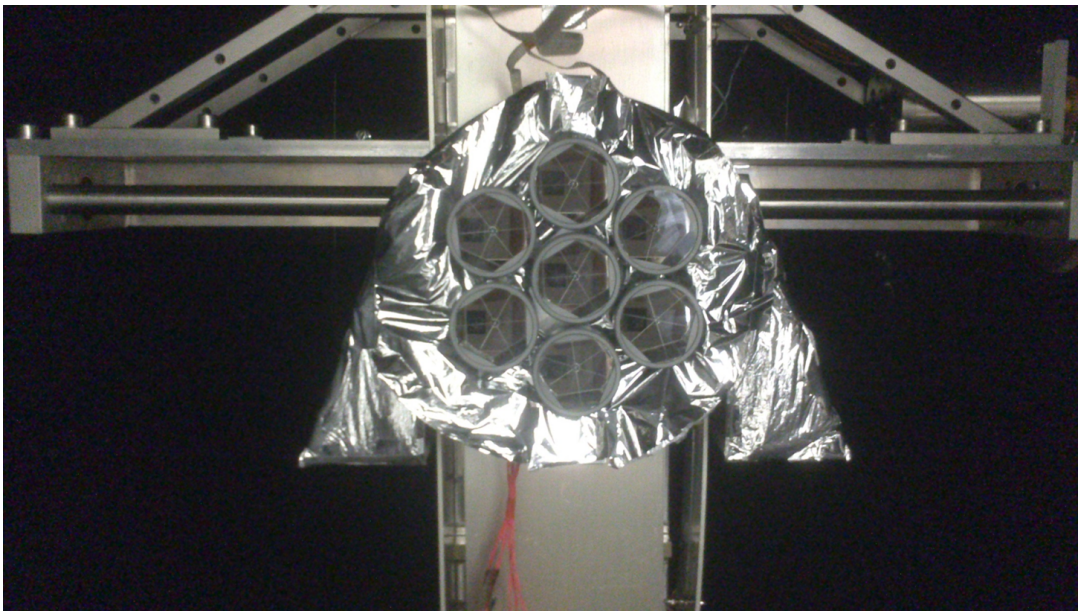

Figure 5.21: Galileo-IOV Engineering Model inside SCF ready for testing

Test	# CCR	$\tau_{ccr} heating$ (s)	$\tau_{ccr} cooling$ (s)	$\tau_{ccr} average$ (s)
SCF-Test 233 K	1	677	597	637±51
	7	644	664	654±34
SCF-Test 273 K	1	632	557	595±48
	7	559	565	562±28
SCF-Test 318 K	1	561	528	545±32
	7	520	682	601±86

Table 5.5: Summary of IOV SCF-Test thermal results: τ_{ccr} during heating phase, τ_{ccr} during cooling phase and τ_{ccr} average

CCR front face during SCF-Tests in heating phase and cooling phase respectively.

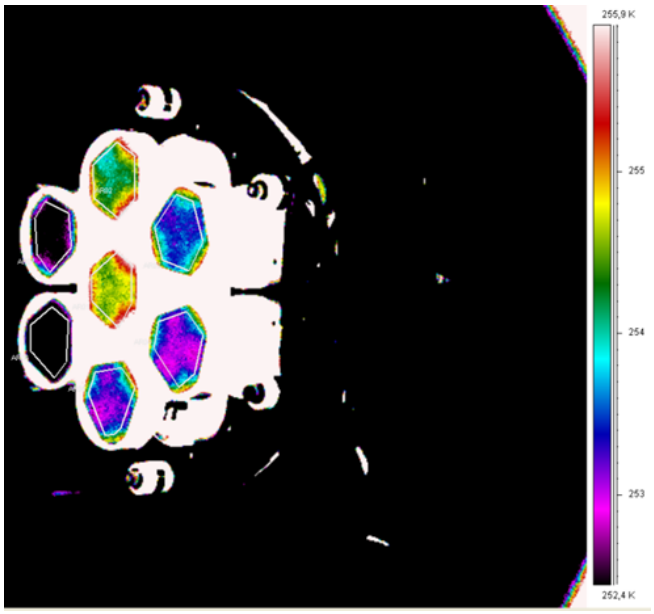

Figure 5.22: Galileo-IOV IR image during SCF-Test

Test	# CCR	Max ΔT (K)	Min ΔT (K)	Average ΔT (K)
SCF-Test 233 K	1	4.1	1.4	2.2±0.7
	7	4.2	1.4	2.3±0.8
SCF-Test 273 K	1	4.5	2.3	3.2±0.7
	7	4	1.7	2.6±0.6
SCF-Test 318 K	1	4.5	2.5	3.1±0.5
	7	5.3	3.2	3.8±0.6

Table 5.6: Summary of IOV SCF-Test temperature gradient on CCR front face during heating phase

Test	# CCR	Max ΔT (K)	Min ΔT (K)	Average ΔT (K)
SCF-Test 233 K	1	3	1.2	1.9±0.4
	7	3	1.3	2±0.4
SCF-Test 273 K	1	2.3	0.9	1.6±0.3
	7	3.1	2.5	2.8±0.1
SCF-Test 318 K	1	2.9	1.7	2.4±0.3
	7	3.5	1.7	2.8±0.5

Table 5.7: Summary of IOV SCF-Test temperature gradient on CCR front face during cooling phase

5.3.2 Selected results of IRNSS test

Concerning the IRNSS-LRA, shown in Fig. 5.23, it is a planar array equipped with 40 solid uncoated 40 mm diameter CCRs. We carried out some tests to investigate its performances during a simulated orbit in different configurations. In order to compare this behavior with other GNSS arrays I report only the most important and comparable results. We did not perform the standard SCF-Test, therefore it is not possible to extract a thermal relaxation time, but we concentrated our analysis on CCR front face temperature gradient.

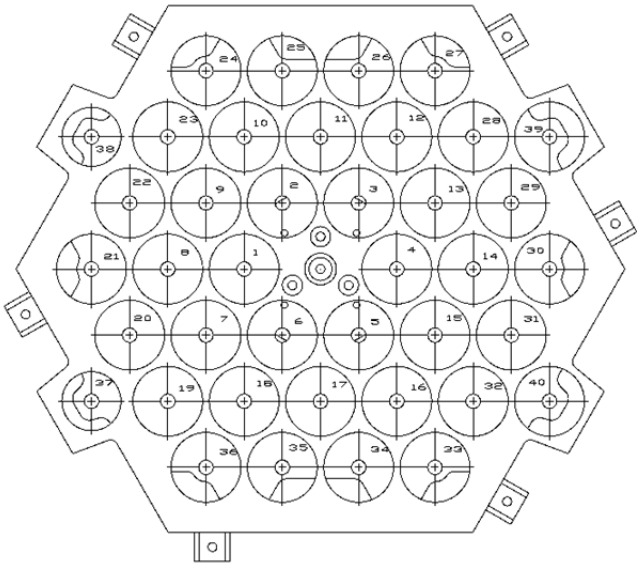

Figure 5.23: IRNSS retroreflector array tested at the SCF_Lab

We performed an Orbit-Test with SS illuminating the array at changing angles, with a rate of about 15°/hour. After reaching equilibrium conditions (cold/vacuum and LRA plate at T=293 K) we started the test, turning on SS with the payload facing it, for about 1 hour before beginning rotations. The test was 6 hours long, as requested by the Indian Space Agency and reproduce a quarter of IRNSS orbit. At

the end we acquired 5 measurements of FFDP and IR pictures for each measured CCR, with payload at 0°, 15°, 37.5°, 60°, 90° respect to Sun rays.

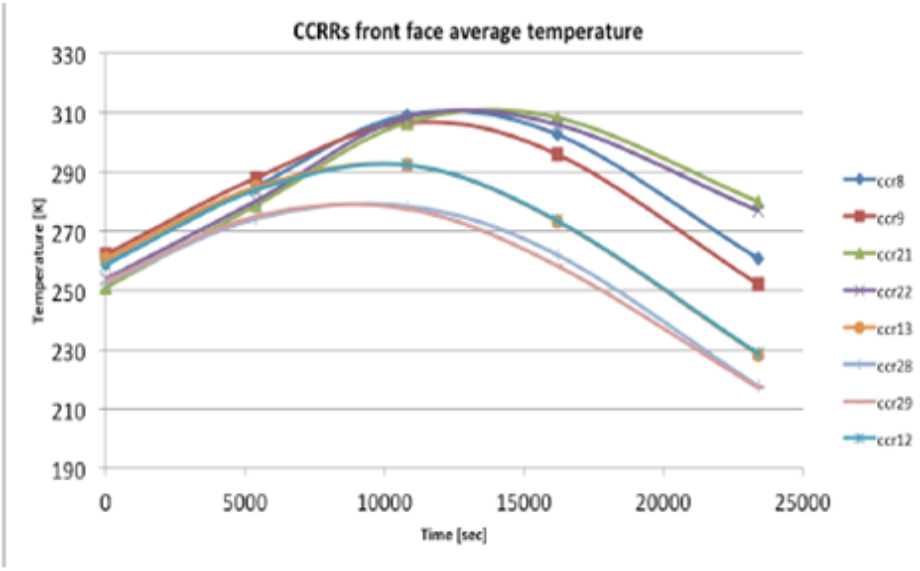

Figure 5.24: Temperature of IRNSS CCRss front face during Orbit-Test

As shown in Figures 5.24 and 5.25 the left side of the array is hotter than the right one because has a more direct Sun irradiation. Moreover external CCRs show a higher front face temperature difference than the others, due to more severe environment conditions. Most of them are affected by an increase of temperature gradient during first rotations, that means between 0° and 15°, then this difference decreases. This behavior could bring to a non-homogeneous reduction of performance throughout the orbit.

Optical analysis performed summing the intensity of all measured CCRs at 18 μrad (the VA of IRNSS satellites), shows that overall trend is a reduction of intensity during first rotations, when the temperature of CCR and gradient on front face are higher, see Fig.5.26.

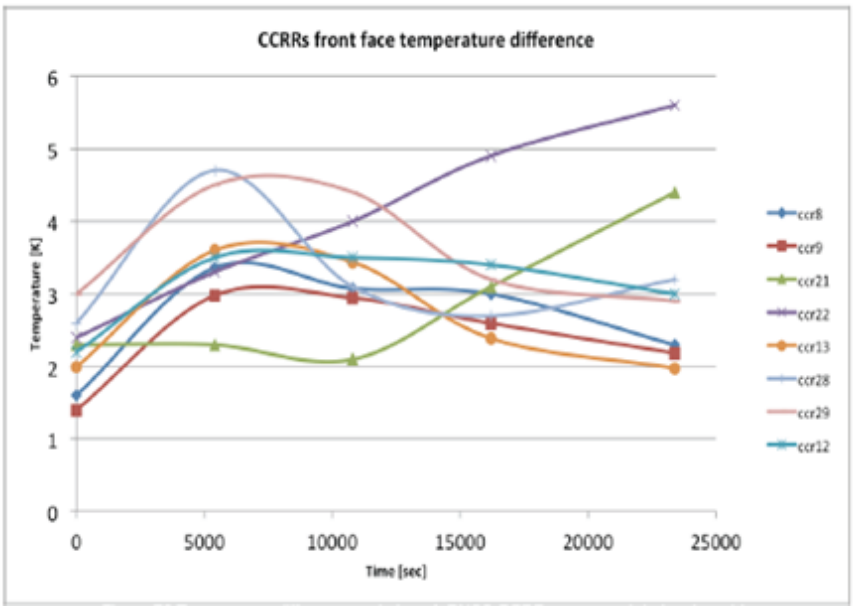

Figure 5.25: Temperature gradient on IRNSS CCRs front face during Orbit-Test

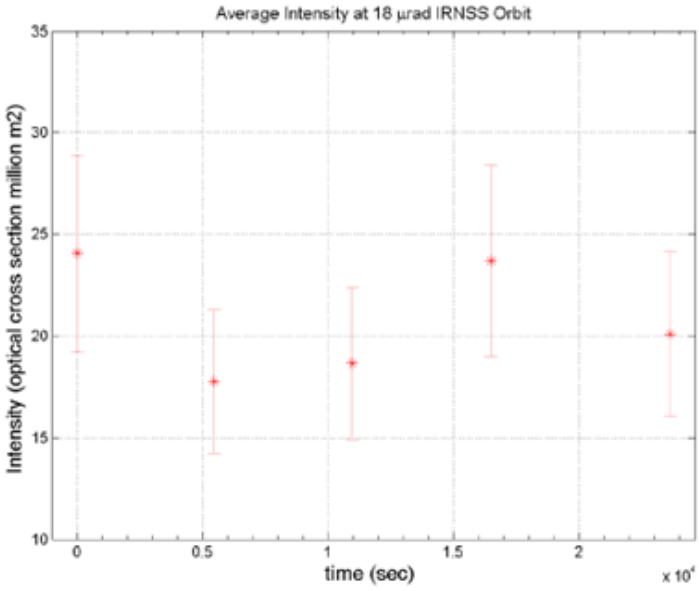

Figure 5.26: Average intensity variation of summed tested CCRs at 18 μrad during Orbit-Test. Error on the intensity is 20% of the relative intensity

5.3.3 Comparison with testing results of INFN-ASI LRA

In this subsection I report some results of testing on GRA. The array is shown in Fig. 5.27 and we carried out both the standard SCF-Test and the Orbit-Test, simulating GCO, described in section 4.3. CCRs optically tested are number 1 and 7, shown in Fig. 5.28.

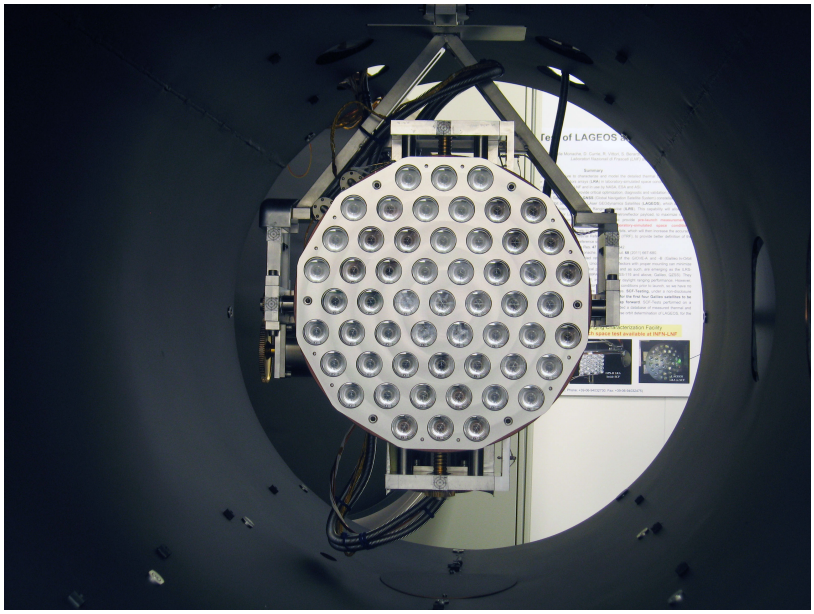

Figure 5.27: GNSS Retroreflector Array inside SCF ready for testing

GRA consists of a near-circular planar array, equipped with 55 solid uncoated 33 mm diameter CCRs. Its design is intended to increase LRAs performance in orbit trying to reduce as much as possible thermal gradients inside CCR and keeping the optical return at the VA of Galileo (24 μrad) as constant as possible. To obtain this, we mounted CCRs on the array with four different orientations around their symmetry axis. CCR mounting system is inherited from LAGEOS satellite.

In Table 5.8 I report τ_{ccr} of the 7 CCRs in the center of the array, for the three

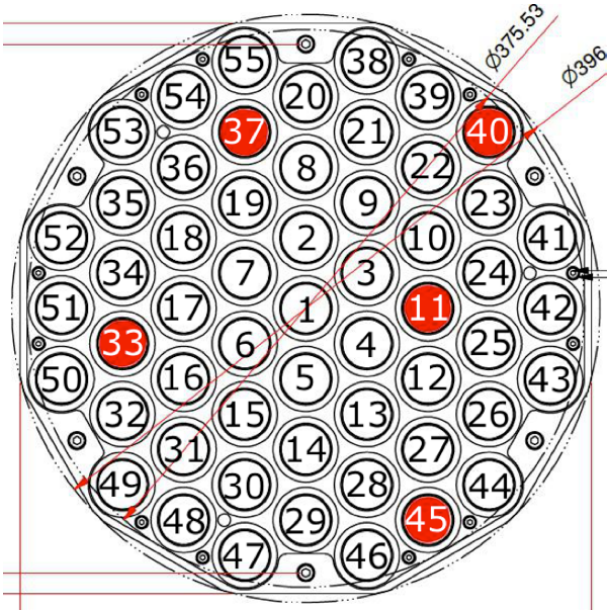

Figure 5.28: GRA CCRs labels. In red the Suprasil 311 CCR, in white the Suprasil 1

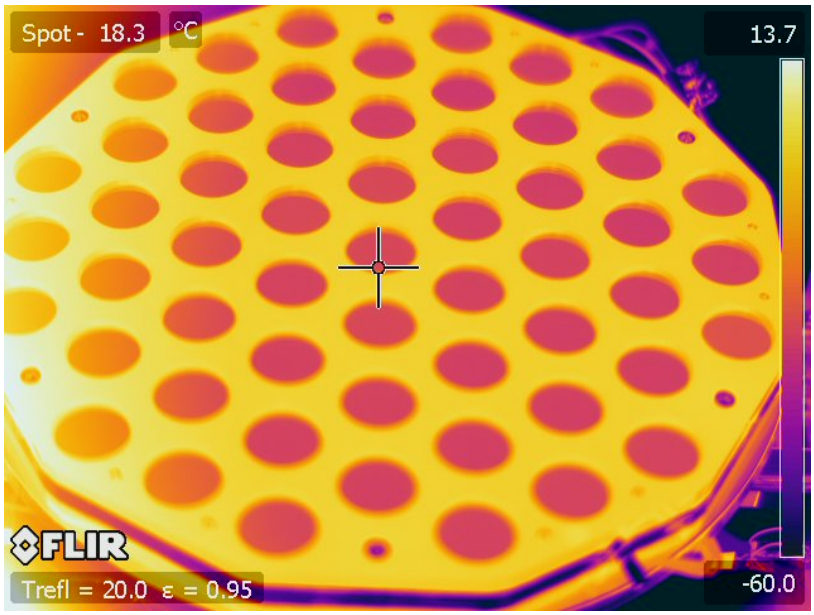

Figure 5.29: IR picture of GRA during SCF-Test

SCF-Tests performed. These values are between 1500 and 2000 seconds, in agreement with the thermal/optical simulation [27]. This proves that τ_{ccr} is independent from the structure and hence there is a good thermal insulation between CCR and metal housing. Moreover from IR pictures (Fig.5.29) it is not possible to find visible hot spots on CCR front face near the mounting screws.

	SCF-Test@280K	**SCF-Test@300K**	**SCF-Test@310K**
CCR1	1579±168	1973±134	1534±156
CCR2	1685±192	1324±89	1746±183
CCR3	1386±161	1359±91	1999±194
CCR4	1603±227	1535±102	2566±354
CCR5	1550±168	1514±100	2513±243
CCR6	1507±164	1417±95	1644±171
CCR7	1744±204	1387±93	2077±211

Table 5.8: Summary τ_{ccr} of 7 central GRA CCRs, during three SCF-Tests

An interesting result is the average intensity at 24 μrad during Orbit-Test, shown in Fig. 5.30. The intensity along half simulated GCO is approximately constant around 2.25 million m^2 and there is not a performance degradation caused by Sun irradiation. If we compare Galileo-IOV and GRA during the same GCO we can observe a significantly different behavior: IOV array at has an average intensity at 24 μrad lower than GRA of about one order of magnitude and it and shows a consistent decrease of intensity after Sunrise phase, while GRA intensity is about stable during all orbit. This important result is shown in Fig. 5.31, where CCRs number 1 and 7 of IOV array are plotted.

From this analysis we can observe a connection between CCR thermal and optical performances. In particular we can conclude that a good thermal behavior, that means high τ_{ccr} and low CCR front face temperature gradient, leads to good optical performances. This study on different GNSS retroreflector arrays helped us

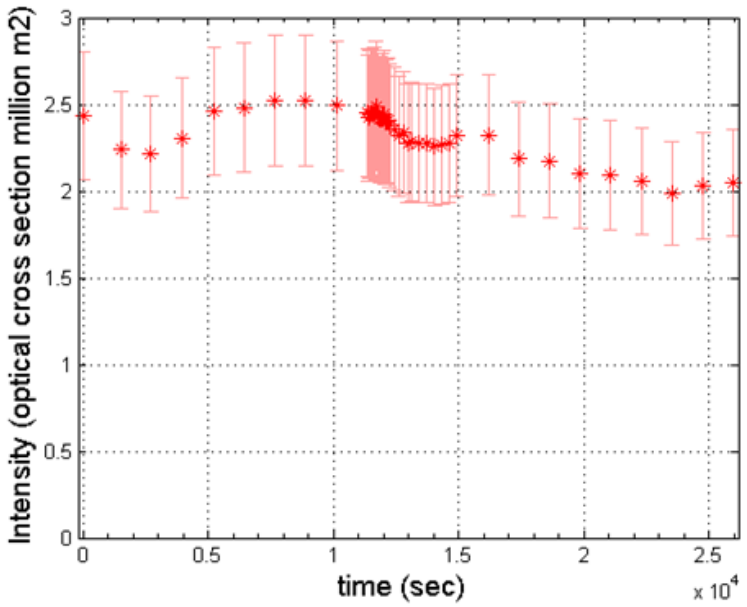

Figure 5.30: GRA CCR1 average intensity at 24 μrad during GCO.

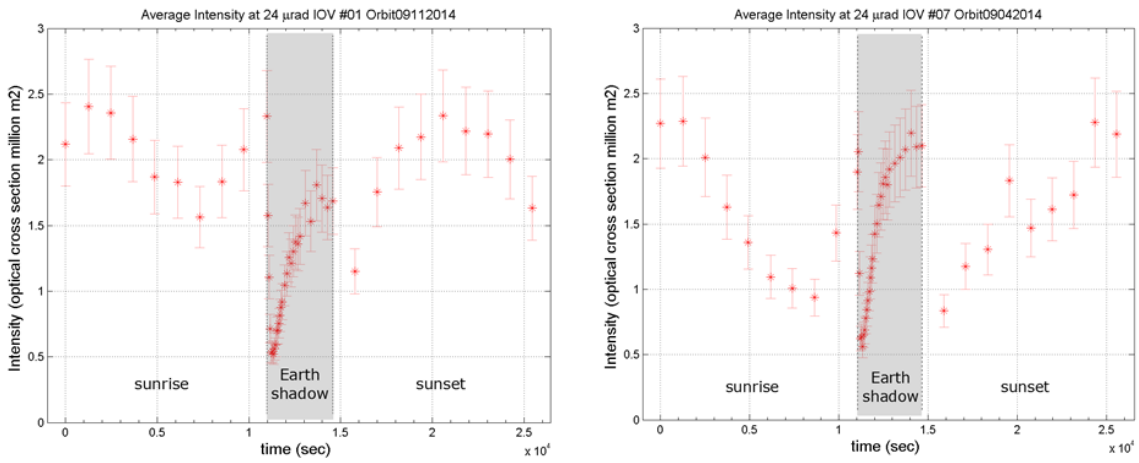

Figure 5.31: Left, IOV CCR1 average intensity at 24 μrad during GCO. Right, IOV CCR7 average intensity, at 24 μrad during GCO

to better understand the behavior of CCR under different heat loads and also to define optimized arrays for GNSS and EO satellites, GRA and CORA respectively.

5.4 Conclusions about CORA test results

We carried out three SCF-Test at different temperature of CORA housing (280 K, 300 K, 320 K). Thermal results show the average τ_{ccr} is about 2000 seconds for all tests. This behaviour indicates a good thermal insulation between CCR and its housing and an optimized mounting system. This is also confirmed by low thermal gradient on CCR front face, that is stable around 2 K or less for all tests.
A reduced heat exchange leads to good optical performances. The average intensity of laser return at ground in the range $25 - 50\mu rad$ for all three tests starts from about 0.6 million m^2 in undisturbed conditions and after a transient phase at the beginning of *SUN OFF*, it comes back to 0.6 million m^2 at the end of tests. Moreover the patterns's shape and intensity at the end of all tests mean the variation due to Sun heating disappears during cooling phase and CCR comes back to work as in undisturbed conditions.
CORA Orbit-Test results show good performances along all orbit. The laser average intensity at $25 - 50\mu rad$ starts from 0.45 million m^2 before Sun illumination and decreases during heating phase up to 0.28 million m^2; then it increases up to about 0.4 millions m^2 during shadow phase. These values are consistent with the same plot of CORA SCF-Test at 300 K and indicate a good optical behavior in realistic operative conditions, affected by a low degradation due to heating.

Chapter 6

INCA Characterization and Results

In this Chapter I report main steps conducted in order to investigate INCA performances. Its characterization consisted of two phases: the first was carried on at JPL and concerned the detection of scatterers in SAR images and their geo-location using GPS coordinates (it is reported in section 6.1); the second phase took place at LNF, regarding the identification of the best background for INCA deployment, to have the maximum return and making some preliminary positioning measurements. This second activity (reported in section 6.2), was not included in G-CALIMES contract Phase 1, in which my activity at LNF has developed, but it was a useful study to validate INCA design and to define the best conditions for future deployments and test campaign.

6.1 Radar Reflector Detection

The activity of my internship at JPL regarded SAR geometric calibration for Earth deformation studies. I used SAR imagery from the international constellation of satellites, including COSMO-SkyMed and Sentinel-1A (referred here to S-1A), to precisely determine the geometric accuracy of SAR images in space and time. I analyzed ground calibration points that are known to mm precision and are measured continuously over time, to characterize the geodetic quality of images and how it changes in time series interpretation.
The area of interest I studied was the south beach of Rosamond Dry Lake Bed, in California, a desert area where 32 trihedral Corner Reflectors (CRs) are installed. These reflectors have different dimensions (twenty-three are 2.4 m, five are 4.8 m and four are 0.7 m) and orientations: some look east and some look west with different azimuth angles and for this reason they can be used for calibration of different SAR images, both in ascending and descending configuration. In Fig. 6.1 one typical Rosamond CR is shown[1].

For my work I used the free software InSAR Scientific Computing Environment (ISCE) for SAR processing, developed by Caltech and Stanford Universities and distributed by the Western North America Interferometric Synthetic Aperture Radar Consortium (WinSAR)[2]. ISCE is a powerful tool for measuring Earth surface deformation due to diverse nature, like earthquakes, volcanic unrest, ground water migration and anthropogenic activity. I used it for running a Python code I developed, to get the power return from CRs in S-1A images. The code compares these radar positioning values (namely "measured") with CRs GPS coordinates (namely

[1] http://uavsar.jpl.nasa.gov/cgi-bin/calibration.pl
[2] https://winsar.unavco.org/

Figure 6.1: Typical Rosamond Corner Reflector[1]

"expected") in IGb08[3], shown in Figure 6.2, applying orbit correction. The orbit correction has been evaluated exploiting the Orbital State Vectors (OSVs)[4] *precise* and *restituted* [29]. I analyzed twelve identical SLC images, downloaded from ESA web site[5], acquired in the period between 07/01/2015 and 09/05/2016, in order to perform a statistic analysis. Table 6.1 summaries images processed. Figure 6.3 represents one of the twelve images from S1-A satellite analyzed. During processing I observed an offset in the CRs positioning expected and measured, in the two satellite view directions (azimuth and slant range). The error in azimuth depends on synchronization issues between atomic and terrestrial clocks and cannot be easily reduced. The error in slant range depends on atmospheric delay when radar beam penetrates ionosphere and troposphere and it can be reduced [8]. The dom-

[3]http://acc.igs.org/igs-frames.html
[4]http://www.unavco.org/data/imaging/sar/lts1/winsar/s1qc/
[5]https://scihub.copernicus.eu/dhus/

Corner reflector number	Geodetic latitude	Longitude	Elevation (m)	Orientation (deg)	Elevation angle (deg)	Side length (m)
0	34.796968	-118.0965259	660.9047	171.83	11.43	2.4384
1	34.79976241	-118.0870473	661.0851	170.67	11.68	2.4384
2	34.80523651	-118.0874563	660.8863	170.67	12.34	2.4384
3	34.80534159	-118.0819065	661.0639	175.33	11.89	2.4384
4	34.80541462	-118.0763749	661.143	175	12.38	2.4384
5	34.80549289	-118.0708001	661.2326	171.33	10.1	2.4384
6	34.80558395	-118.0652228	661.2451	172	10.76	2.4384
7	34.80566908	-118.0596638	661.3144	173	11.59	2.4384
8	34.80575124	-118.0540701	661.4592	171.66	10.21	2.4384
9	34.80581331	-118.0489123	661.4532	174.67	8.45	2.4384
10	34.80592464	-118.043364	661.522	173.33	7.96	2.4384
11	34.80602337	-118.0376901	661.6029	170	8.19	2.4384
12	34.80604616	-118.0322784	661.9067	173.33	11.84	2.4384
13	34.80519087	-118.0844157	660.8183	349	13.86814	2.4384
14	34.80543974	-118.0789121	660.9549	350	9.047237	2.4384
15	34.80551809	-118.0733394	661.2359	350.75	7.35	2.4384
16	34.80554783	-118.0678661	661.2917	350.83	6.9	2.4384
17	34.80550096	-118.0624549	661.3198	351.67	11	2.4384
18	34.80568571	-118.0563896	661.3912	351.67	11.23	2.4384
19	34.80572179	-118.0518132	661.4171	351	11.56	2.4384
20	34.80583723	-118.0463549	661.4538	350	10.61	2.4384
21	34.8059005	-118.040331	661.4691	355	9.95	2.4384
22	34.80603087	-118.0350619	661.7198	354	10.59	2.4384
23	34.80250391	-118.0858021	661.2242	350.93	21.75	4.8
24	34.80290863	-118.0766439	661.4462	350.77	22.15	4.8
25	34.80315584	-118.0687772	661.5239	349.38	21.23	4.8
26	34.80322777	-118.06058	661.6443	350.7	22	4.8
27	34.80351914	-118.0522778	661.6858	350.22	22	4.8
28 (Key)	34.79894033	-118.0948046	661.5012	353.5	12.3	0.7
31 (Hello Kitty)	34.80122243	-118.0790931	661.8806	351	16.9	0.7
34 (Kite)	34.80349533	-118.0633906	661.9856	354	22.4	0.7
37 (Kangaroo)	34.80577869	-118.0476721	662.1196	350	28.4	0.7

Figure 6.2: Rosamond CCRs coordinates expressed as WGS-84 geodetic latitude and height above the reference ellipsoid with a = 6378137 m and f = 1/298.257222, from[1]

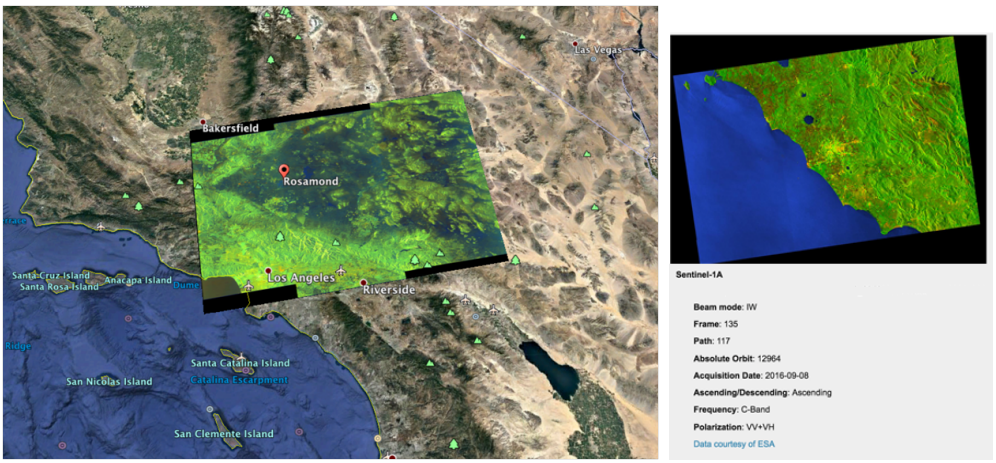

Figure 6.3: Left, SAR image superimposed on Google Earth image of Rosamond area. Right, Details of S1-A SLC image of Rosamond area

S-1A images	Number in the plot
S1A IW SLC 1SDV 20160905	1
S1A IW SLC 1SDV 20160719	2
S1A IWSLC 1SDV 20160321	3
S1A IW SLC 1SDV 20160309	4
S1A IW SLC 1SDV 20151216	5
S1A IW SLC 1SDV 20151122	6
S1A IW SLC 1SDV 20151029	7
S1A IW SLC 1SSV 20151017	8
S1A IW SLC 1SDV 20150911	9
S1A IW SLC 1SSV 20150806	10
S1A IW SLC 1SDV 20150725	11
S1A IW SLC 1SDV 20150701	12

Table 6.1: S-1A images processed, all are in ascending configuration

inant component of this error is due to the troposphere and this delay depends on atmospheric parameters and on the zenith angle of satellite. I reduced it evaluating the vertical delay estimated from European Centre for Medium-Range Weather Forecasts (ECMWF) and processing it using a python module (PyAPS package[6]) developed by Caltech University. This module estimates differential phase delay maps due to the stratified atmosphere, taking into account pressure, vapor water and temperature parameters [30].

First result of my analysis is presented in Figure 6.4: it represents the power return from burst number 2 of S1-A image of 16/12/2015, expressed in dBW and twelve CRs (red dot in the blue circles) are visible. This is clearer in Figure 6.5: on the left there is a zoom in a box of 16x16 pixels around each expected position; on the right there is the same zoom after an oversampling process and the expected diffraction pattern from a reflector is clearly visible (power is expressed here in W).

[6]http://earthdef.caltech.edu/projects/pyaps/wiki/Main

The black cross represents CRs expected position.

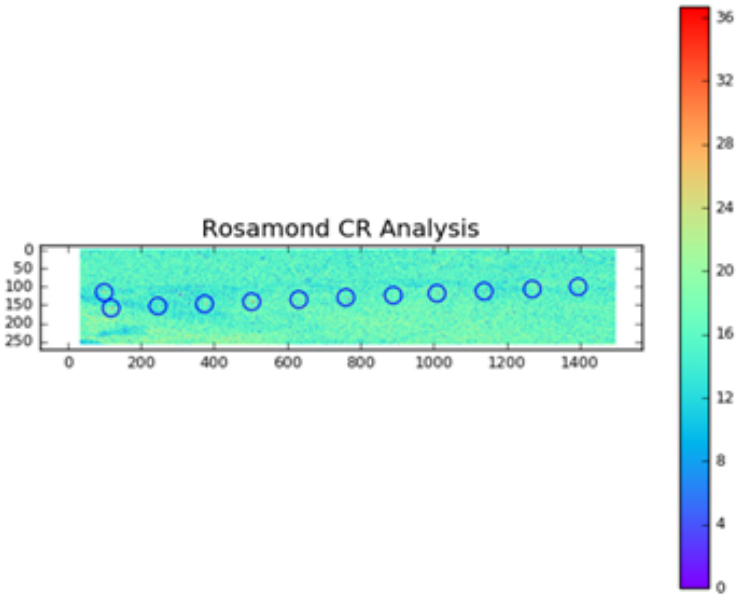

Figure 6.4: Rosamond S-1A SLC images processed with CCRs visible.

This analysis highlights a difference between expected and measured positions. Figure 6.6 shows the error in azimuth direction for all twelve images. Its mean value is $[-0.68 \pm 2.00]$ m. Figure 6.7 represents the error in slat-range direction before correction and its mean value is $[2.77 \pm 0.10]$ m. After troposphere correction it is reduced to $[0.41 \pm 0.16]$ m, as shown in Figure 6.8. These results are consistent with previous analysis conducted on S-1A Stripmap images by ESA and University of Zurich [29].

During this period at JPL I learnt radar image processing and CCR detection and I used these skills to perform the first measurement with INCA in Italy, presented in the next section.

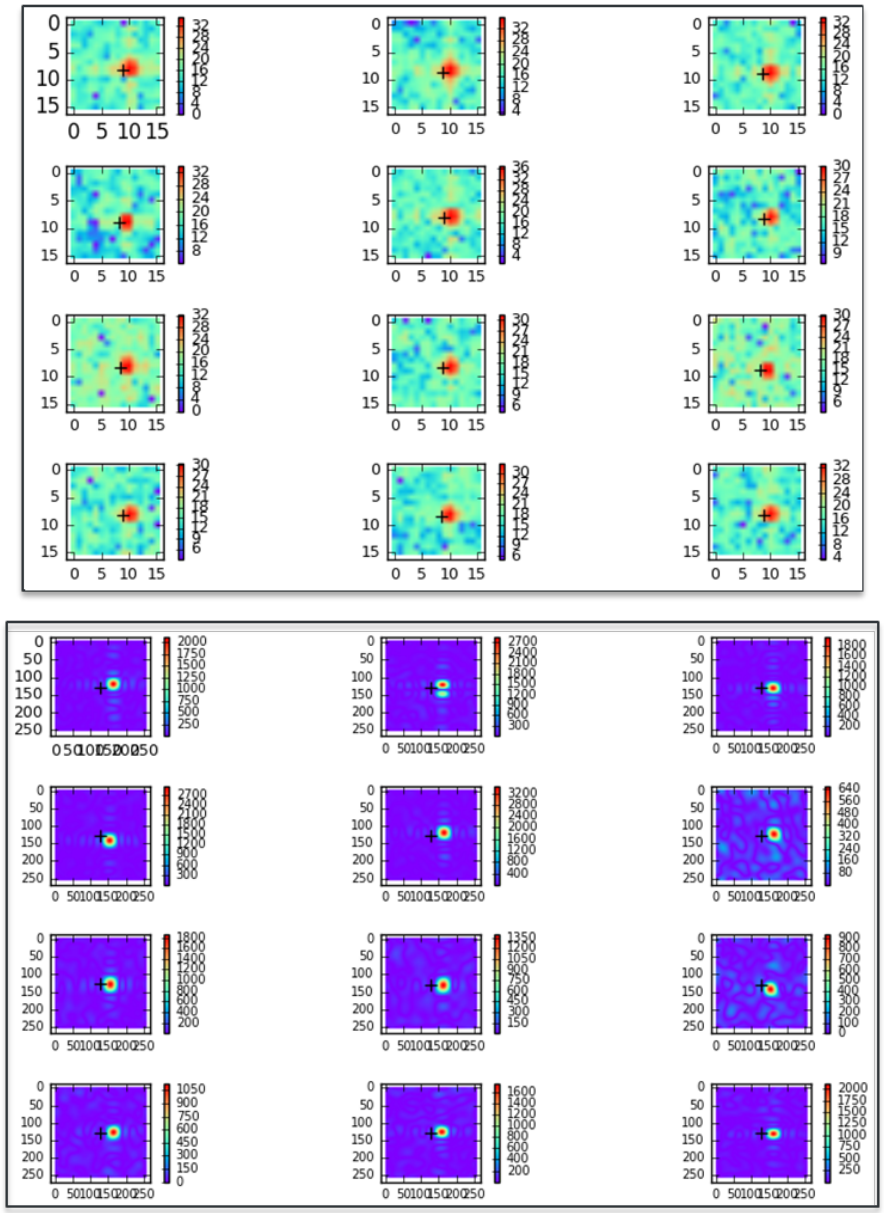

Figure 6.5: Left, SAR image zoom around each visible CR. Right, image after oversampling process

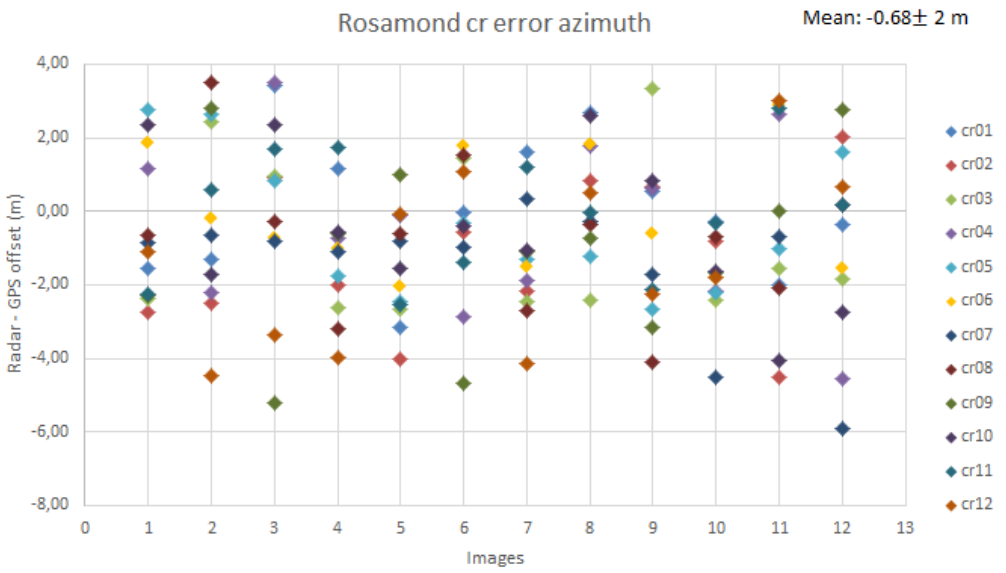

Figure 6.6: Error between CRs radar measured and expected position in azimuth direction from 12 S1-A images

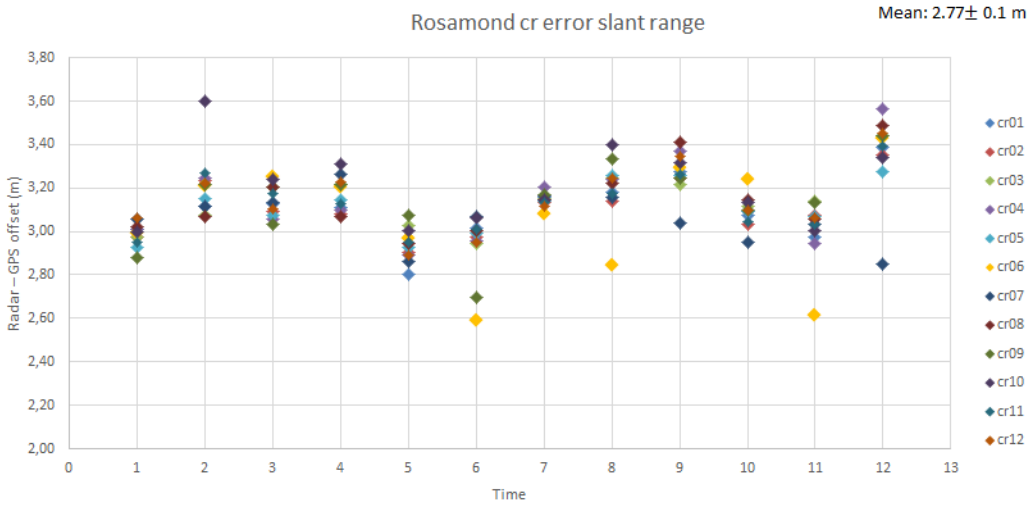

Figure 6.7: Error between CRs radar measured and expected position in slant range direction from 12 S1-A images

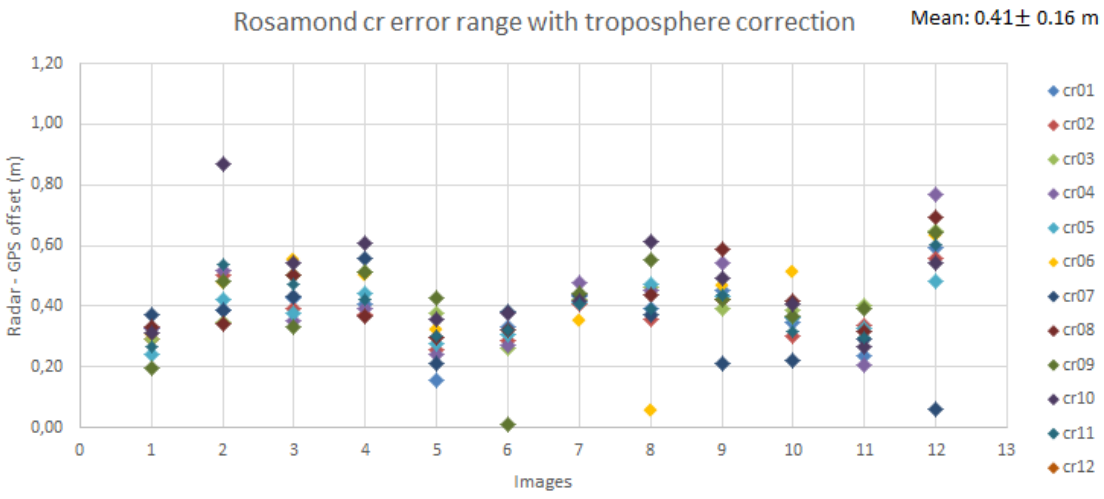

Figure 6.8: Error between CRs radar measured and expected position in slant range direction after troposphere correction

6.2 INCA deployment and first measurement

As mentioned before the second part of INCA characterization has taken place at LNF. The aim of this activity was the identification of the best background for deployment and the demonstration of device visibility. I choose two different sites for placing INCA: a lawn inside LNF in Frascati (site 1) and a paved road in Grottaferrata (site 2), see Table 6.2 for details. Two pictures of INCA in field are shown in Figure 6.9. In order to perform the first detection I used S1-A images and I processed them using ISCE and the same Python code described in the previous section. In Fig. 6.10 there is the S1-A image related to site 1.

Site	**Acquisition Date**	**Coordinates**
Number 1 Frascati	06/04/216	lat=41.822372 N long=12.675277 E
Number 2 Grottaferrata	09/08/216	lat= 41.7890417 N long= 12.6645794 E

Table 6.2: Sites for INCA deployment

Before deployment I calculated the incidence angle between satellite and site coordinates in ECEF (Earth-Centered Earth-Fixed) System. Then I aligned INCA in azimuth and elevation in order to pointing the satellite. I used for this activity a commercial compass and a clinometer, both with an accuracy of $\pm 2°$. However looking at the simulation described in section 3.2.1, I can assert that such accuracy is more than enough, because INCA angular response does not show significative decrease at that accuracy.

Fig. 6.11 left represents S-1A image with INCA located on site 1. Blue circle is the expected position but it is clear that inside it, the device is not visible. This is due to an excessive background noise produced by buildings and human structures

Figure 6.9: Left, site 1: INCA on a lawn in Frascati. Right, site 2: INCA on a paved road in Grottaferrata

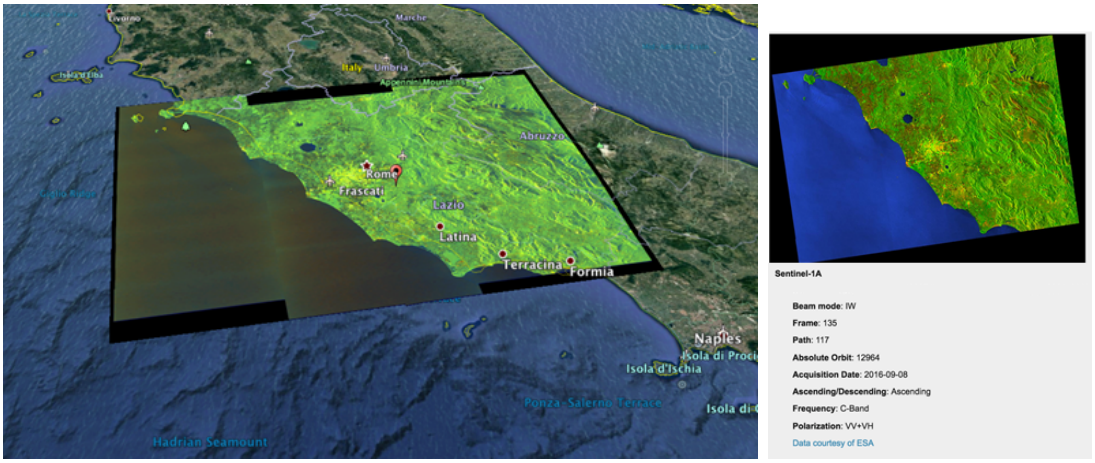

Figure 6.10: Left, SAR image superimposed on Google Earth image of Frascati area. Right, Details of S1-A SLC image of Frascati area

presented on this urban area and also by the grass under the device. The blades of grass dimension is of the same order of magnitude of beam's wavelength which invests the device and thus causes interference and overlap in the power returns, that prevent the correct identification of the reflector. Even after a zoom we cannot identify the device.

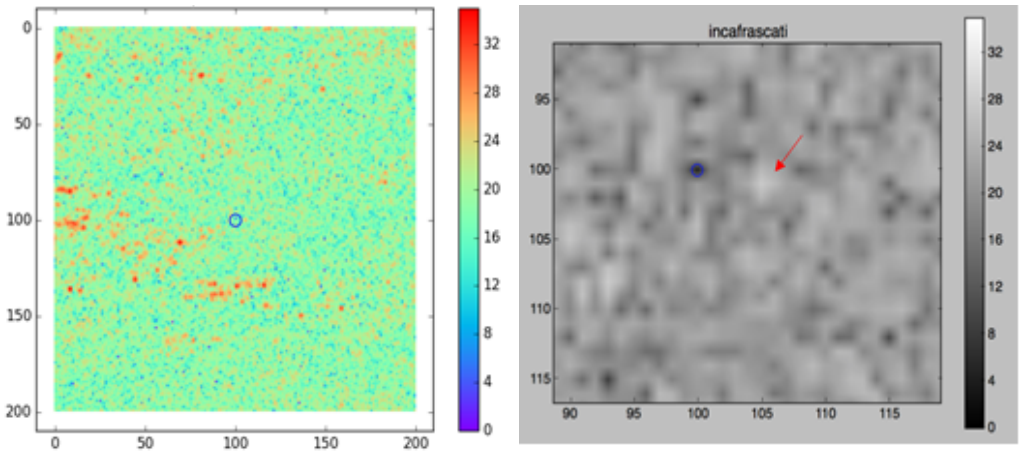

Figure 6.11: Left, S1-A processed image of site 1 at 06/04/2016. Right, zoom around CR expected position

Fig. 6.12 represents S-1A image with INCA placed on site 2. Here the detection is easier, even if CR diffraction patter is not as expected. The error between measured and expected position, estimated after oversampling process, is 1.06 m in azimuth direction and 0.6 m in slant range. I analyzed just one image for each site and I did not apply any atmospheric correction. We can conclude that the paved road is a better background respect to lawn, but the desert is the best on which to place CR for image calibration [31].

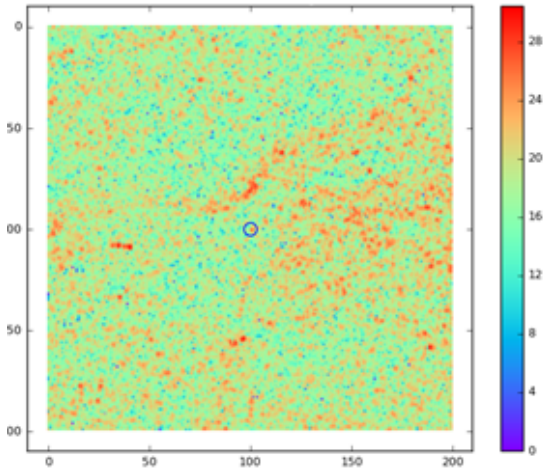

Figure 6.12: S1-A processed image of site 2 at 09/08/2016

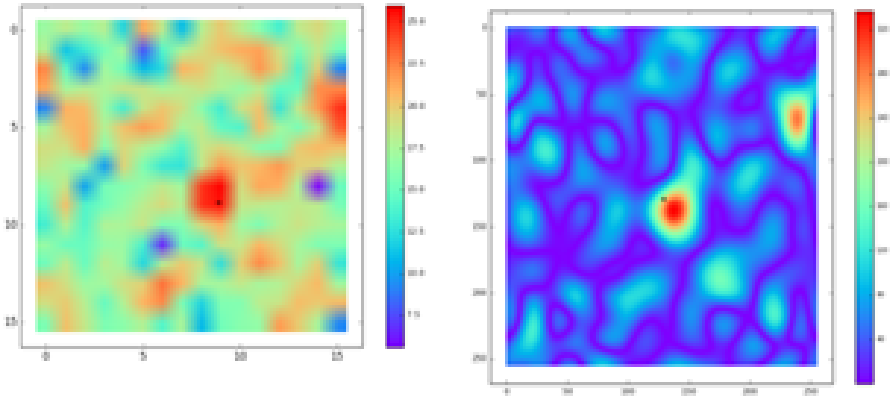

Figure 6.13: Left, SAR image zoom around CR on site 2. Right, image after oversampling process

6.3 Conclusions and future activity for INCA entire characterization

As explained in this chapter, INCA characterization consisted in two phases: the first at JPL concerned the detection of radar reflectors in SAR images and their geolocation using GPS coordinates; the second phase at LNF regarded the identification of the best background for INCA deployment, to have the maximum return and making some preliminary positioning measurements. The main result showed that the desert is the best background for this kind of measurements, a paved road is acceptable while a lawn is the worst background, preventing the device's detection. In order to complete the entire characterization of INCA, G-CALIMES phase 2 is starting. This activity involves INCA deployment at ASI-Centro di Geodesia Spaziale in Matera, where we perform the inter-calibration of three different positioning techniques, SAR, SLR and GNSS, exploiting radar reflector, optical CCR and GPS/Galileo receiver of INCA device. In particular we process images of the area from COSMO-SkyMed constellation for INCA detection in field, applying also orbit and atmospheric corrections; we measure INCA position with the receiver and with the CCR exploiting the local network for laser measurements in the station; finally we combine these results to quantify the improvement that the device produces to the positioning of terrestrial maps.

Conclusions and Future work

This thesis work is in the framework of G-CALIMES, a INFN-Italian Ministry of Defense technological research project. Its goal is the absolute inter-calibration of SLR, GNSS and SAR, in order to mainly increase the accuracy of GNSS and EO satellite constellations and hence improve positioning measurements.

My activity concerned on development and performance testing of space and terrestrial instrumentation based on retroreflectors. I carried out my research at the SCF_Lab of LNF, with the collaborations of NASA-JPL.
My work can be summarized in three main parts:

- Characterization of LRA for GNSS satellites to investigate thermal and optical performances and to deeply study the correlation between structural design and optical behaviour
- Design and characterization of a LRA for EO satellites, named CORA
- Feasibility study, design and first deployment of a ground-based radar device, named INCA

CORA is a retroreflectors payload intended to be mounted on COSMO Second Generation satellites, with the aim of guaranteeing an accurate ranging measurement from every Laser Ranging station on Earth, in a compact and lightweight assembly.

It consists of 4 coated laser CCR with an active area of 33 mm, made of fused silica installed on a pyramidal Aluminum chassis. CORA best design was chosen thanks to optical and orbital simulations, in order to minimize the weight and maximize performances.
Its characterization consisted of two tests: the standard SCF-Test and the Orbit-Test, both carried out in order to evaluate device's thermal and optical performances. Key parameters I evaluated are τ_{ccr}, FFDP and temperature gradients on CCR front face. With the SCF-Test I evaluated CCR engineering properties with a standard qualified test, in order to quantify thermal insulation between retroreflector and array structure; while with the Orbit Test I studied payload thermal and optical properties in realistic operative conditions. I developed a Matlab code to process thermal experimental data and to compute Sun rays inclination on payload in orbit, to be reproduced during test. CORA test results show a good insulation between CCR and its housing, that means an optimized mounting system and a good optical performances during operational life.

INCA device consists of a radar reflector equipped with a GPS/Galileo receiver and an optical CCR. It allows the inter-calibration of SLR with GNSS and SAR techniques. INCA key element is the invariant point along the vertical line joining the receiver with the tip of radar and optical reflectors, that allows a common systematic error in the intercalibration measurement.
INCA feasibility study performed during my thesis, regards the device response analysis for different satellites, sites and pointing and is divided in two parts: the first was carried out at JPL during my summer internship and the second was conducted at LNF. At JPL I performed geometric calibration of Sentinel-1A images of a desert area in California, using ISCE software. I developed a Python code to detect radar retroreflectors in the scene and compare these measurements with GPS

coordinates, performing orbital and atmospheric corrections. At LNF I processed Sentinel-1A images of Frascati (Rome) area to identify the best background for INCA deployment. Processed data indicate the best background is a desert area, even if it is possible to detect the object also in some urban areas with acceptable results. In addition, INCA response study demonstrates the device system pointing has an accuracy that allows an alignment respect to the satellite, without any loss in the returning signal. Therefore the two analyses show that the only possible detection issues for future device deployment come from the background.

Concluding, the result of my research activity has been a contribution to the improvement of EO satellites and their terrestrial maps position, as well as their integration with SLR and GNSS.

For future activities I will work on CORA structural validation tests, proposing payload for the integration on COSMO Second Generation satellites. Regarding INCA, with the beginning of G-CALIMES phase 2, I will proceed with an extensive experimental characterization (up to 2019) with SLR-SAR-GPS combined measurements at ASI-Centro di Geodesia Spaziale in Matera. In addition other deployment sites will be chosen in collaboration with the Italian Ministry of Defense, providing finally a complete analysis on INCA performances "in field".

Bibliography

[1] `http://itrf.ensg.ign.fr/`

[2] `http://ilrs.gsfc.nasa.gov/docs/slrover.pdf`

[3] *Probing Gravity with Next Generation Lunar Laser Ranging* Chapter in the book Gravity: Where Do We Stand, ISBN: 978-3-319-20224-2, 195-210 (2016)

[4] P.L. Bender *et al.*, *The Lunar Laser Ranging Experiment*, Science, Volume 182, Issue 4109, pp 229-238, 1973

[5] M. R. Pearlman, J. J. Degnan and J. M. Bosworth, *The International Laser Ranging Service*, Adv. in Space Research, Vol. 30, No. 2, pp. 135-143, July 2002, DOI:10.1016/S0273-1177(02)00277-6.

[6] Elliot D. Kaplan,Christopher J. Hegarty, *Understanding GPS. Principles and Applications*. Second edition.

[7] `http://infocom.uniroma1.it/~pier/didattica.html`, Prof. Pierfrancesco Lombardo, handouts of the course for *Radiolocalizzazione e Navigatione Satellitare*, University of Rome "La Sapienza"

[8] A. Bernardini, *Lezioni del corso di Sistemi di comunicazione satellitare*, Ingegneria 2000, second edition 2008

[9] C. Oliver, S. Quegan, *Understading Synthetic Aperture Radar Images*, Scitech Pub Inc, 2004

[10] Alessandro Ferretti, Andrea Monti-Guarnieri, Claudio Prati, Fabio Rocca, *InSAR Principles: Guidelines for SAR Interferometry Processing and Interpretation*, European Space Agency, Karen Fletcher, February 2007

[11] De Zan, F., Guarnieri, A. M. (2006), *TOPSAR: Terrain Observation by Progressive Scans. Geoscience and Remote Sensing*, IEEE Transactions on, 44(9), 2352–2360. doi:10.1109/TGRS.2006.873853

[12] `https://sentinel.esa.int/web/sentinel/user-guides/sentinel-1-sar/acquisition-modes/interferometric-wide-swath`

[13] `http://www.igs.org`

[14] C. Urschl, et al., *Validation of GNSS orbits using SLR observations*, Adv. in Space Research, Vol. 36, pp. 412-417, 2005, DOI:10.1016/j.asr.2005.03.021

[15] C. Urschl, et al., *Contribution of SLR tracking data to GNSS orbit determination*, Adv. in Space Research, Vol. 39, pp. 1515-1523, 2007, DOI:10.1016/j.asr.2007.01.038.

[16] P. Fridelance, E. Samain and C. Veillet, *A new optical time transfer generation*, Experimental Astronomy, 7, pp 191-207, 1997.

[15] ESA, Specificatin of Galileo and GIOVE space segment properties relevant for Satellite Laser Ranging, ESA Technical Note ESA-EUING-TN/10206, issue 3, 2008

[16] `http://www.esa.int/Our_Activities/Observing_the_Earth/Copernicus/Overview4`

[17] Plag,H.P., Pearlman , M.R., *The Global Geodetic Observing System*. Meeting "The Requiremnts of the Global of a Global Society on a Changing Planet in 2020", Springer Berlin Heildeberg, 2009.

[18] Dell'Agnello S. et al. *Creation of the new industry-standard space test of laser retroreflectors for the GNSS and LAGEOS* Adv. in Space Res. 47 (2011), 822-842.

[19] J. Degnan et al., *Millimeter Accuracy Satellite Laser Ranging: A Re- view Contribution of Space Geodesy to Geodynamics*, Technology Geodynamics Series, 25 (1993)

[20] Kamal Sarabandi, Tsen-Chieh Chiu, *Optimum Corner Reflectors for Calibration on Imaging Radars*, IEEE Transactions on Antennas and Propagation, Vol. 44. NO. 10, October 1996

[21] Dell'Agnello S., et al., *ETRUSCO-2 an ASI-INFN project of technological development and "SCF-Test" of GNSS Laser Retroreflecotr Arrays.*

[22] B. Efron, *The Jackknife, the Bootstrap, and Other Resampling Plans*, Society of Industrial and Applied Mathematics CBMS-NSF Monographs 38, 1982.

[23] R. W. Johnson, *An Introduction to the Bootstrap*, Teaching Statistics. Volume 23, Number 2, Summer 2001.

[24] 4. Roger R. Bate, Donald D. Muller, Jerry E. White, *Fundamentals of Astrodynamics*. New York: Dover Publications, Inc. 1971

[25] Anderson B.J., Justus C.G., Batts G.W., *Guidelines for the Selection of Near-Earth Thermal Environment Parameters for Spacecraft Design* Nasa Internal Report, NASA/TM-2001-211221 (October, 2001)

[26] Dell'Agnello S., et al., *SCF-Test of Galileo IOV retroreflectors*, presented at the International Technical Laser Workshop 2012 (ITLW-12), INFN-LNF, Frascati (Rome), Italy November 5-9, 2012

[27] A. Boni et al., Integrated Thermal-Optical simulations of a GNSS retroreflector array, Adv. Space Res., doi: 10.1016/j.asr.2015.03.035, 2015.

[28] John R. Howell, M. Pinar Menguc, Robert Siegel, *Thermal Radiation Heat Transfer*, 6th Edition, CRC Press

[29] A. Schubert, D. Small, N. Miranda, D. Geudtner, E. Meier, *Sentinel-1A Product Geolocation Accuracy: Commissioning Phase Results*, Remote Sensing 2015, 7, 9431-9449, doi:10.3390/rs70709431

[30] Jolivet, R., R. Grandin, C. Lasserre, M.-P. Doin and G. Peltzer, *Systematic InSAR tropospheric phase delay corrections from global meteorological reanalysis data*, Geophys. Res. Lett., 38, L17311, doi:10.1029/2011GL048757 (2011)

[31] Donald M. Ugsang, Kiyoshi Honda, Genya Saito, *Assessment of small passive corner reflectors for geometric correction of Radarsat fine mode SAR data*, Paper presented at the 22nd Asian Conference on Remote Sensing, 5-9-Nov 2001, Singapore

[32] James B. Abshire, Chester S. Gardner, *Atmospheric Refractivity Corrections in Satellite Laser Ranging*, IEEE Transactions on Geoscience and Remote Sensing, Vol. GE-23, N.4, July 1985